Alphas and Surface Backgrounds in Liquid Argon Dark Matter Detectors

Christopher J. Stanford

A Dissertation
Presented to the Faculty
of Princeton University
in Candidacy for the Degree
of Doctor of Philosophy

Recommended for Acceptance
by the Department of
Physics
Adviser: Peter D. Meyers

November 2017

Abstract

Current observations from astrophysics indicate the presence of dark matter, an invisible form of matter that makes up a large part of the mass of the universe. One of the leading theories for dark matter is that it is made up of Weakly Interacting Massive Particles (WIMPs). One of the ways we try to discover WIMPs is by directly detecting their interaction with regular matter. This can be done using a scintillator such as liquid argon, which gives off light when a particle interacts with it.

Liquid argon (LAr) is a favorable means of detecting WIMPs because it has an inherent property that enables a technique called pulse-shape discrimination (PSD). PSD can distinguish a WIMP signal from the constant background of electromagnetic signals from other sources, like gamma rays. However, there are other background signals that PSD is not as capable of rejecting, such as those caused by alpha decays on the interior surfaces of the detector.

Radioactive elements that undergo alpha decay are introduced to detector surfaces during construction by radon gas that is naturally present in the air, as well as other means. When these surface isotopes undergo alpha decay, they can produce WIMP-like signals in the detector.

We present here two LAr experiments. The first (RaDOSE) discovered a property of an organic compound that led to a technique for rejecting surface alpha decays in LAr detectors with high efficiency. The second (DarkSide-50) is a dark matter experiment operated at LNGS in Italy and is the work of an international collaboration. A detailed look is given into alpha decays and surface backgrounds present in the detector, and projections are made of alpha-related backgrounds for 500 live days of data. The technique developed with RaDOSE is applied to DarkSide-50 to determine its effectiveness in practice. It is projected to suppress the surface background in DarkSide-50 by more than a factor of 1000.

Acknowledgements

I would like to thank the Physics department for providing me with the opportunity to pursue a Ph.D. at Princeton University and for providing me with financial support through fellowships and teaching assistantships.

I would like to thank my advisor, Prof. Peter Meyers, for providing academic guidance and financial support, for allowing me the freedom to pursue what interested me, and for being an excellent role model of scientific rigor and objectivity. I would also like to thank him for his seemingly endless supply of entertaining stories, and for his approach toward academic advisement that I greatly appreciated. It was a pleasure and a privilege to be his student.

I would like to thank Prof. Frank Calaprice for his encouragement and guidance when it came to my work in the lab, and for aiding in the understanding and publication of my results. I would also like to thank him for letting me borrow some of his lab equipment for my research.

I would like to thank Prof. Cristiano Galbiati for calling me up when I was first admitted into Princeton and encouraging me to join the DarkSide Collaboration. I would like to thank him for his financial support to attend collaboration meetings and for providing me with many networking opportunities.

I owe a great deal of thanks to Helen Ju for her constant administrative support in arranging travel and reimbursement. I wish her a happy, well-deserved retirement.

I would like to thank Herman Verlinde for his academic guidance and for agreeing to be on my defense committee.

I would like to thank all the support staff at the university, especially those in the physics department who work each day to ensure that Jadwin Hall is an enjoyable place to do research.

I owe thanks to all those involved in the DarkSide-50 collaboration for coming together to build and study such an excellent experiment. I owe thanks to the NSF

and DOE that directly and indirectly supported my involvement with the project. I am also thankful for the NSERC support I received in my first year of studies.

I would like to thank all my past and present DarkSide-50 collaborators at Jadwin Hall: Jason Brodsky, Graham Giovanetti, Guangyong Koh, Xinran Li, Hao Qian, Masayuki Wada, Shawn Westerdale, Xin Xiang, Chengliang Zhu. Their knowledge was constantly drawn upon throughout my time at Princeton. A special thanks to Xin Xiang, my office mate who was pestered with more questions than most, and played an important role in understanding the low-gain digitizer data used throughout this thesis, and Masayuki Wada, a living encyclopedia of all things DarkSide-50, who seemed to have the answer to just about any question I asked.

I would like to thank collaborator Alissa Monte for her contributions to the DarkSide-50 alpha analysis and for her work in simulating TPB scintillation.

My research with the RaDOSE detector would not have been possible without the assistance of Jingke Xu and Shawn Westerdale. Their insight and manpower were vital to the success of the experiment and I owe them both a lot of gratitude.

I would like to thank all those whose support had an indirect impact on my thesis. My friendships formed through the Aquinas Institute, the Graduate Board Game Club, and elsewhere, provided much-needed opportunities to take my focus off research.

I would like to thank my family, especially my Mom and Dad, to whom this thesis is dedicated. Your constant love and support has made me into the man and scientist I am today. I am forever grateful.

Finally, I am very thankful for my wife Janine. Thankful for her continual love and support throughout my graduate studies; for all her hard work and dedication, especially during the last couple months as I was busy writing this thesis; and for being the mother of our son, Joseph, who I am very thankful to have in my life.

To my parents.

AMDG

Contents

List of Tables

List of Figures

Chapter 1

Outline

This thesis begins with several introductory chapters (2–6) to lay the groundwork necessary for the final chapters (7 & 8) which discuss the results of two different liquid argon experiments.

Chapter 2 gives an introduction to the dark matter problem, including a popular theory for dark matter and how experiments test the theory. The introduction is aimed at a layman who knows nothing of dark matter. A deeper review of various dark matter models is beyond the scope of this thesis and can be found elsewhere [1]. Instead the discussion is kept simple and streamlined to provide a basis for the following chapters on liquid argon detectors.

Chapter 3 gives an introduction to how liquid argon (LAr) works as a means to detect dark matter. The topic of pulse-shape discrimination is introduced as a tool that allows LAr detectors to heavily suppress signals that would interfere with a dark matter signal. Some of the challenges to using LAr are discussed in this chapter.

Chapter 4 gives an introduction to wavelength shifters, which are chemical compounds used on surfaces in LAr detectors and play a critical role in surface backgrounds.

Chapter 5 gives an introduction to alpha radioactivity.

Chapter 6 introduces alpha decays on detector surfaces. An overview is given of many different modes of surface background and how it can cause a signal that may be mistaken for dark matter.

Chapter 7 gives a detailed view of the RaDOSE detector and its results. A technique is outlined in this chapter that uses the wavelength shifter in liquid argon detectors to reject background signals from surface alpha decays.

Chapter 8 gives an overview of the DarkSide-50 experiment and a detailed view of alphas and surface backgrounds in the detector. The technique developed in Chapter 7 is applied to DarkSide-50 data and projections are given of the background for 500 days of exposure.

Appendix A is a translation of a paper by R. Voltz and G. Laustriat that provides an explanation for the scintillation processes in organic compounds and is helpful in understanding the results seen in Chapters 8 and 7.

Appendix B takes the technique developed for surface background rejection in liquid argon and applies it to liquid xenon experiments through the use of MgF_2.

Chapter 2

Dark Matter

Over the past century, a series of astrophysical observations have been made that are inconsistent with our understanding of how gravity works. The observations seem to indicate that there is a lot more matter out in the universe than just the stars, planets, and other "regular" matter that we can see.

The solution to this problem remains elusive. The most common theory involves a new form of matter that is invisible and does not interact with light, called "dark matter".

To date, no widely accepted detection of dark matter has been made, but the search remains a very active field of research.

In this introductory chapter we will highlight the major historical observations that built the case for dark matter. We will then summarize a proposed theory of what dark matter could be, along with a brief summary of how experiments are currently testing that theory.

2.1 Evidence

2.1.1 Galaxy Clusters

The first major development in the history of dark matter came in 1933 with Fritz Zwicky's observations of the Coma Cluster, which is cluster of over 1,000 galaxies. Zwicky made an estimate of the total mass of the cluster using two different methods. The first method, which we call the "virial" method, involved measuring the velocities of galaxies on the edge of the cluster. One can use these velocities to infer the mass that must be present, because there must be enough gravity to prevent these edge-galaxies from being flung out of the cluster. The second method, which we call the "luminosity" method, involved directly counting the mass in the cluster based on the matter that can be seen.

The surprising result was that the virial method showed there to be much more mass present in the cluster than the luminosity method. In other words, the galaxies in the Coma Cluster were travelling so fast that the cluster should be flung apart. To explain this discrepancy Zwicky proposed the existence of "dark matter", which is present in the cluster but cannot be seen, and so avoids being counted in the luminosity method. This dark matter would exert the necessary gravitational forces to hold the cluster together [2].

2.1.2 Rotation Curves

The next major piece of observational evidence came in the 1960s and 70s from the work of Vera Rubin and Kent Ford [3, 4]. By this time the technology had improved to the point where the rotation of an individual galaxy could be measured. Instead of applying the virial method to clusters of galaxies, it could be applied to the stars within a single spiral galaxy. Rubin and Ford measured a similar discrepancy as Zwicky between the virial method and the luminosity method: the stars in the

galaxy were moving too fast. Based on the visible matter in the galaxy, the stars on the outer edge should be flung off into the void. In order to hold the galaxy together, Rubin's calculations show that the galaxies must be made primarily of dark matter, with visible matter making up only a small fraction of the total mass.

2.1.3 Gravitational Lensing

The last piece of evidence for dark matter that will be given here is that of gravitational lensing. Gravitational lensing is notable because it provides a third method for determining the mass of an astronomical body, which we call the "lensing" method.

The lensing method is based on the principle that matter bends light. The amount of this bending is calculated by Einstein's general theory of relativity, and is dependent upon the mass of the object. An object with more mass has a greater ability to bend light. For objects such as the Earth or the Sun, the bending effect is still quite small, but when looking at larger bodies in the universe the effect becomes noticeable, clearly distorting the light from background objects in the same way the lens of a magnifying glass distorts the images behind it. An example of this phenomenon can be seen in Fig. 2.1.

Estimates of the mass of galaxies obtained with the lensing method match the value obtained by the virial method rather than the luminosity method [6]. There is simply not enough visible matter in these galaxies to cause the amount of light-bending that we see.

To summarize, multiple independent methods have been used to calculate masses of galaxies, and they agree not only on the existence of an unseen form of matter, but on the quantity of that matter that is required to explain the observations. This agreement formed the main thrust for the scientific community's interest in dark matter.

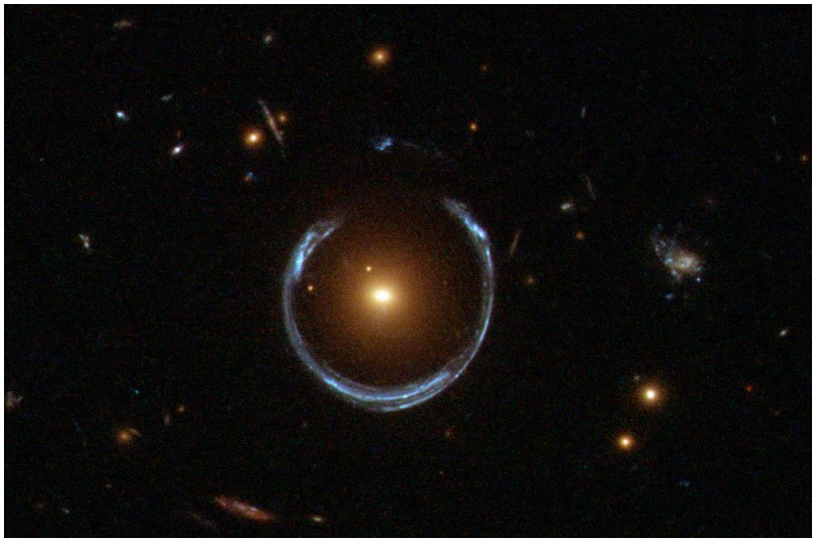

Figure 2.1: This image from the Hubble Space Telescope shows a large red galaxy with a blue galaxy far behind it. As the light from the background galaxy comes toward us, it is distorted by the gravity of the foreground galaxy, forming a ring shape [5].

2.1.4 Other Evidence

In the present day, many other measurements have been made that corroborate those listed above. The interested reader can find some of the most convincing pieces of evidence for dark matter within the topics of structure formation [7], and the Bullet Cluster [8]. A breakdown of the total matter content of the universe is provided by measurements of the cosmic microwave background [9], which tell us that dark matter makes up roughly 85% of the mass of the universe.

2.2 Theory and Experiment

The fact that the astronomical observations are inconsistent with the known laws of gravity is undisputed. However, no such consensus exists when it comes to a solution. While dark matter is the most common answer, theories abound as to what dark matter actually is. Still others disagree with the need for dark matter at all, suggesting instead that the laws of gravity need tweaking [10].

Giving a fair treatment to all current theories of dark matter is beyond the scope of this thesis. Instead, just one particular theory will be discussed – the one that liquid argon detectors hope to verify.

2.2.1 WIMPs

One theory of dark matter is that it is made up of Weakly Interacting Massive Particles, or WIMPs. WIMPs can be defined by their two primary characteristics. First, they are elementary particles that interact with regular matter only through gravity and the weak nuclear force. They do not interact through electromagnetism, which means they cannot not absorb, emit, or scatter photons and are thus invisible. Second, their mass is somewhere in the range of 1 to 10,000 times the mass of a proton. Theories that predict masses outside this range are more rare and are typically referred to as "light dark matter" [11] or "super heavy dark matter" [12].

The WIMP is currently the most popular dark matter candidate – certainly more money is being spent looking for WIMPs than in pursuing any alternative theory [13] – and it is the candidate being searched for by the majority of the dark matter community.

Its popularity stems from an apparent coincidence between the fields of cosmology and elementary particle physics. If WIMPs exist, then during the early stages of the universe they would have been continually produced and destroyed at a rate depending on a parameter called the self-annihilation cross-section. If this parameter is too large, then too much of the dark matter would have been annihilated in the early universe to explain the abundance we see today. Conversely, if this parameter is too small, it would have resulted in more dark matter surviving the early universe than what we now measure. As it turns out, the sweet spot for this parameter matches that of a massive particle that interacts through the weak nuclear force. This apparent coincidence is called the "WIMP miracle."

As with any scientific theory, the key to verifying the existence of WIMPs is to make a prediction and confirm that prediction with an experiment. Being able to predict the motion of stars and galaxies does not count, as these are the observations that WIMPs were cooked up to explain. Instead, experiments are attempting to prove the existence of these particles through some method other than gravity.

Some experiments, such as those at particle accelerators, look for WIMPs by smashing particles together in the hopes of producing their own dark matter. This method is sometimes called "production" (Fig. 2.2a). Other experiments use telescopes to look out into the galaxy, hoping to detect gamma rays from two dark matter particles colliding with each other and annihilating. This method is called "indirect detection" (Fig. 2.2b). The third method for detecting WIMPs, which we will focus on, is called "direct detection"(Fig. 2.2c). Direct detection experiments hope to see a WIMP collide directly with the detector itself. Liquid argon experiments fall under the category of direct detection.

2.2.2 Direct Detection

A WIMP can be detected directly in a number of ways. A common method is through the use of a scintillator. A scintillator gives off light when a particle interacts with it. In this way an invisible particle (the WIMP) can produce a visible signal (the light). Common scintillators include sodium iodide crystals and noble liquids such as argon or xenon. In addition to the light, heat and free electric charge can be produced during a WIMP's collision with an atom, and some experiments are designed to pick up these signals in addition to or instead of the light.

Direct detection experiments are attempting to measure both the mass of the WIMP and its cross-section. Its cross-section can be thought of as its likelihood to collide with regular matter; the larger the cross-section the more frequent the collisions.

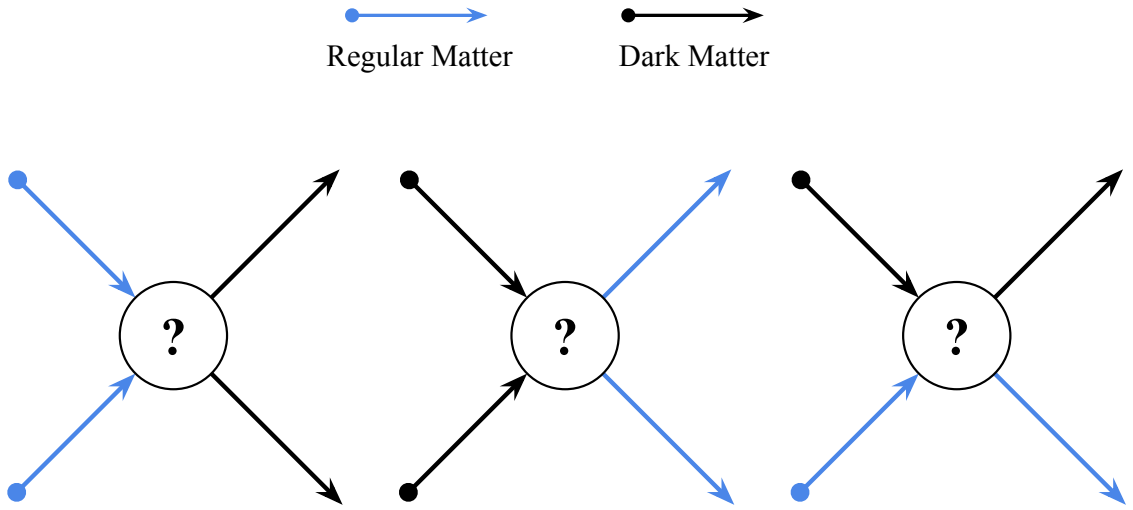

(a) Production. An accelerator smashes two regular particles together to see if dark matter particles come out. The dark matter particles would escape detection, but the experiment can infer their presence using the laws of conservation of energy and momentum.

(b) Indirect Detection. If a dark matter particle by chance collides with another dark matter particle, they could mutually annihilate to produce regular particles (such as photons) that can be seen.

(c) Direct detection. If a dark matter particle directly collides with a regular matter particle, it will cause the regular particle to recoil. Certain types of regular matter, such as an argon atom, will give off light when it recoils. A direct detection experiments aims to detect this light.

Figure 2.2: Production, indirect detection, and direct detection. The question mark at the the center of each diagram refers to our uncertainty of how exactly the particles would interact.

Since neither the mass nor the cross-section is known, there is room for many complimentary direct detection experiments to exist. For example, the DarkSide-50 experiment is designed to look for WIMPs with a mass between 10 and 10,000 GeV, while the SuperCDMS experiment is designed to be more sensitive to a low mass WIMP with a mass below 10 GeV (for reference, a proton is about 1 GeV). As for the cross-section, experiments are designed to be as sensitive as they can be, because by looking for WIMPs with very small cross-sections they simultaneously look for WIMPs with larger cross-sections (this becomes clear when cross-section is thought of as the collision probability). To increase in cross-section sensitivity an experiment either needs to either reduce the "noise" from collisions caused by background sources or increase the number of collisions caused by WIMPs by building a bigger detector.

A plot of WIMP cross-section vs. mass is called the "parameter space". It represents the vast number of possible values that the cross-section and mass could take. Experiments are trying to pinpoint where in this space the WIMP lives.

Current Status

Over time many experiments have published negative results, ruling out the part of the parameter space that they were searching. These results can be seen in Fig. 2.3, which shows the (somewhat outdated) status of the direct detection search as of Nov. 2015. Each result is presented with a solid line, showing that the experiment has excluded all of the parameter space above that line. The dotted lines are the projected exclusion curves of future experiments if they see no evidence of dark matter. The yellow region at the bottom of the plot is called the "neutrino floor". Once an experiment is built that reaches the sensitivity of the neutrino floor, it will be sensitive enough to detect a high rate of recoils induced by neutrinos, making dark matter detection much more difficult.

The shaded ovals and circles in the figure represent a selection of theoretical models that predict a certain WIMP mass and cross-section. Much of this space is going to be probed with the next generation of detectors.

The enclosed regions in the figure – "DAMA", "CRESST", "CDMS Si" – indicate experiments that measured a statistically significant dark-matter signal. The exclusion of these regions by a multitude of more sensitive experiments has cast doubt on those signals.

In summary, it is an exciting time for the direct detection of WIMPs, with experiments probing more of the parameter space every year, and many theoretical WIMP models still to be tested.

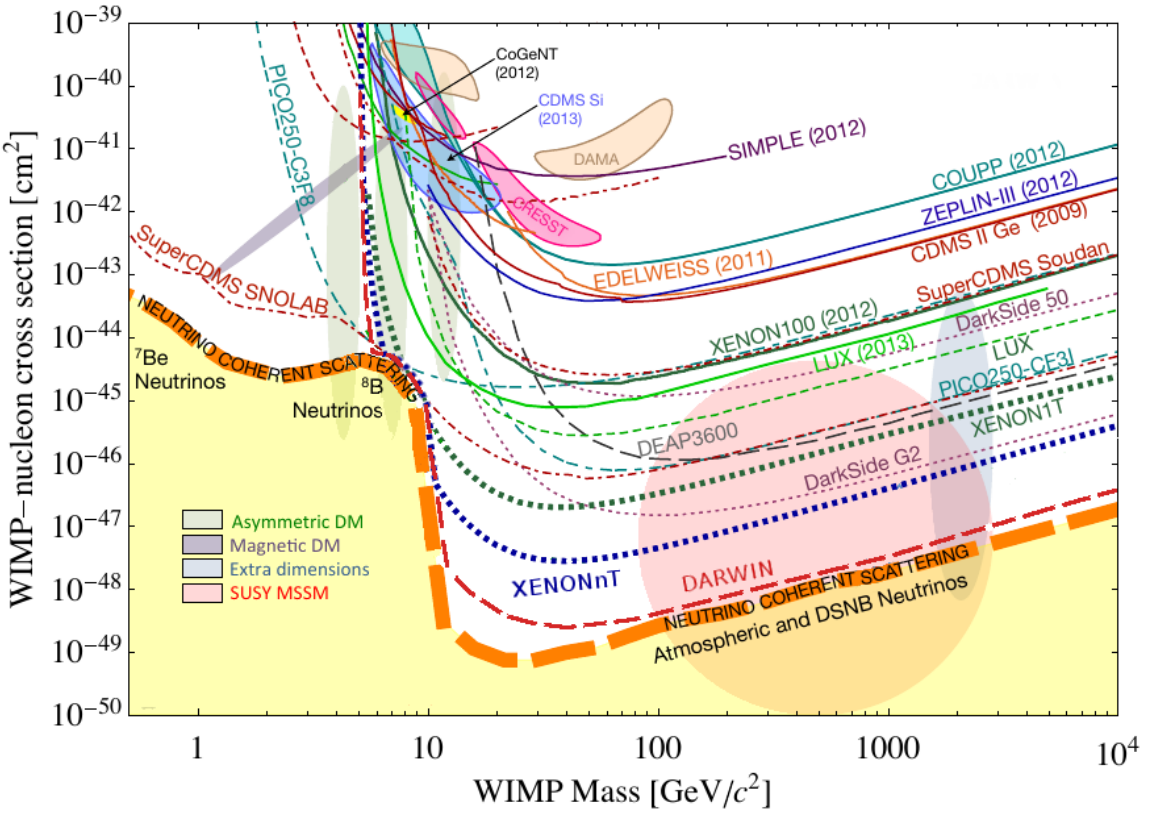

Figure 2.3: State of the WIMP search as of Nov. 2015. Solid lines represent exclusion curves from completed experiments. Dotted lines represent future experiments. Ovals/circles represent predictions from WIMP models. Enclosed curves represent statistically significant WIMP signals. (Credit: Klasen et al. [14]).

Chapter 3

Liquid Argon (LAr)

Liquid argon (LAr) is a popular means of detecting ionizing radiation [15, 16, 17, 18, 19, 20, 21]. It has a high scintillation yield, it is abundant in the atmosphere, and it is cheap to obtain and purify compared to alternative noble liquid scintillators. It also exhibits strong pulse shape discrimination (PSD) between nuclear and electronic recoils, allowing a suppression of beta and gamma backgrounds.

3.1 How it Works

Incoming particles or radiation can interact with an argon atom in two primary ways. The first way is through electromagnetic interactions with the atom's electrons; an incident gamma ray can impart some of its energy to an electron, ejecting it from the atom. This energetic electron then scatters about, losing energy by exciting and ionizing other argon atoms it its path. This process is called an electron recoil (ER). Another source of ER includes the electron ejected during beta decay. The second way argon interacts is through nuclear recoils (NR), in which a particle such as a neutron transfers some of its momentum to the argon's nucleus. The recoiling nucleus is slowed down by the surrounding argon as well, but produces a much shorter and

denser track than the ER due to the NR's higher stopping power ($\mathrm{d}E/\,\mathrm{d}x$). Another source of NR includes the sought-after WIMP.

Alphas, fission fragments, and the recoil nuclei from alpha decays also produce short, dense ionization tracts like the NR of an argon nucleus.

Excited argon atoms (excitons) quickly bond with neutral argon atoms to form excited "dimers" [22]. These dimers are short lived and produce light when they dissociate. The process (Pathway 1) is as follows:

$$\mathrm{Ar}^* + \mathrm{Ar} \rightarrow \mathrm{Ar}_2{}^* \tag{3.1}$$

$$\mathrm{Ar}_2{}^* \rightarrow 2\mathrm{Ar} + h\nu \tag{3.2}$$

where $h\nu$ is a 128 nm photon.

Argon ions are also capable of forming ionized dimers, which can recombine with a free electron and dissociate into heat and excited argon as follows (Pathway 2):

$$\mathrm{Ar}^+ + \mathrm{Ar} \rightarrow \mathrm{Ar}_2^+ \tag{3.3}$$

$$\mathrm{Ar}_2^+ + e^- \rightarrow \mathrm{Ar}^{**} + \mathrm{Ar}^* \tag{3.4}$$

$$\mathrm{Ar}^{**} \rightarrow \mathrm{Ar}^* + \mathrm{heat} \tag{3.5}$$

with the excitons resulting from steps 3.4 and 3.5 potentially continuing on through Pathway 1 to emit photons.

The initial ratio of excitons to ions (N_{ex}/N_i) is dependent on the nature of the incident radiation. Measurements of ER find $N_{ex}/N_i = 0.21$ [23], and measurements of NR find $N_{ex}/N_i \simeq 1$, depending on the recoil energy [24]. The presence of an electric field causes free electrons to be pulled away from the argon ions and results in less initial recombination, which decreases N_{ex}/N_i.

3.2 Pulse Shape Discrimination (PSD)

The excited electron in the photon-emitting Ar_2* exists in a singlet or triplet state with the rest of the dimer. The timescale of the scintillation (step 3.2) depends on the state of the electron. Singlet states decay quickly, with a lifetime of 4-7 ns. The decay of triplet states to the ground state are forbidden transitions and occur more slowly, with a lifetime of up to 1.6 µs, depending on the presence of argon impurities.

It is an experimental fact that ERs and NRs produce argon dimers with different singlet-to-triplet (S/T) ratios. Dimers formed from ERs are mostly in the triplet state, with $S/T \sim$ 0.3, while dimers for NRs are mostly in the singlet state, with $S/T \sim 3$ [25]. The time profile of the pulse of light from an ER is therefore different than for a NR. The difference is significant enough that argon experiments have demonstrated the ability to discriminate ER from NR to better than one part in 10^7 (meaning less than one ER in 10^7 is mislabeled as an NR) [16]. This is referred to as pulse-shaped discrimination, or PSD.

The nature of what exactly causes the difference in S/T for ERs and NRs has been the subject of much interest and debate, but no consensus has been reached. One theory is that the excited dimers directly excited through Pathway 1 are more likely to be in the singlet state than those that are formed through recombination (Pathway 2). This is because during the excitation process a singlet must remain a singlet due to spin selection rules, but during recombination, an electron has 3-to-1 odds of falling into the triplet state. This, in combination with the higher N_{ex}/N_i for NRs, could be the reason that NRs are more likely to produce singlet states [26].

3.3 Challenges

Argon faces two primary difficulties as a dark matter target. The first difficulty is the presence of ^{39}Ar, an isotope produced in atmospheric argon by cosmic rays. ^{39}Ar

undergoes beta-decay with a half-life of 269 years. With an activity in atmospheric argon of roughly 1 Bq/kg, ^{39}Ar quickly becomes the dominant background in large argon experiments.

In the last few years we have made significant advancement in solving the ^{39}Ar problem, primarily through the use of underground argon. Argon obtained underground, having been shielded from cosmic rays for millennia, has been found to have lower concentrations of ^{39}Ar [27]. The level of reduction relative to atmospheric argon has been measured to be more than 10^3 [28]. With ongoing efforts to expand the underground argon extraction facilities and further reduce the ^{39}Ar background through distillation, progress is now being made toward argon detectors measuring on the scale of tens of tons [29, 30, 31].

Another difficulty is argon's ultraviolet emission spectrum. The ultraviolet light is unable to directly penetrate the windows of the detector, so it must first be shifted to longer wavelengths using a wavelength shifter (WLS) which is evaporated onto the interior surfaces of the detector. The WLS absorbs the 128 nm photons from the argon scintillation and re-emits photons of a longer wavelength which can then penetrate the windows and be picked up by photon counters. Unfortunately, the re-emission by the WLS is isotropic and can obscure the original location of the event within the detector. The result is less precise position reconstruction, necessitating large fiducial cuts to avoid surface backgrounds.

Advancement toward reducing surface backgrounds has seen recent improvement and will be discussed in detail in Chapters 7 and 8.

Chapter 4

Wavelength Shifter (WLS)

A wavelength shifter (WLS) is a material that absorbs high energy photons and re-emits lower energy photons. Photon detectors are generally poor at detecting high energy (ultraviolet) photons, so WLSs are used to shift the photons to longer (visible) wavelengths where they can be counted more efficiently. The light emitted by LAr scintillation has a wavelength of 128 nm, putting it in the vacuum ultraviolet region. Window materials such as fused silica or acrylic are not transparent to such short wavelengths, so any detector that hopes to measure the scintillation must utilize WLSs[1].

4.1 How WLSs work

Wavelength shifting is a process brought about by the molecular structure of aromatic organic compounds. These compounds are composed of carbon atoms in phenyl groups or other structures of carbon atoms with multiple bonds (see Figure 4.1).

The ground state electronic configuration of carbon is $1s^2 2s^2 2p^2$. When a carbon atom forms a double bond, an electron in the $2s$ orbital is excited to the empty $2p$

[1]Research involving UV-sensitive photodetectors is very active and has lately yielded some successes in directly detecting argon scintillation light [32].

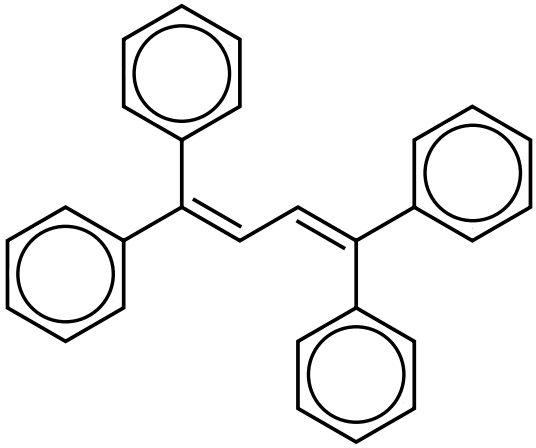

Figure 4.1: Skeletal formula of tetraphenyl butadiene. The π-bonds, represented as delocalized rings in the phenyl groups, lie above and below the plane of carbon atoms. These loosely bound electrons are responsible for this compound's wavelength shifting properties.

orbital, and the outer s orbital mixes with two of the p orbitals through a process called sp^2-hybridization. This mixing produces three identical sp^2 orbitals lying in a plane, separated from each other by 120°, with the leftover and unchanged p orbital lying perpendicular to the plane. The three sp^2 orbitals form strong bonds with other atoms, called σ-bonds. The remaining p orbital can then overlap with a neighboring atom's p orbital, forming a π-bond. While the σ-bonds form directly between neighboring atoms, the weaker π-bonds form above and below the molecular plane, with loosely bound electrons that are more easily excited and ionized. It is the excitation of the π-bound electrons that are responsible for the compound's wavelength shifting ability [33].

The π-bound electrons in aromatic compounds have energy level spacings on the order of eVs, ideal for absorbing UV light. These electronic energy levels can be denoted S_0 (ground state), S_1 (first excited singlet state), S_2, etc. Each electronic energy level is split by vibrational modes of the molecule, with energy spacings on the order of a tenth the size of the electronic levels [34]. The vibrational sublevels of S_0 are denoted S_{00}, S_{01}, etc.

A diagram of the wavelength shifting process can be seen in Fig. 4.2. At room or cryogenic temperatures, the majority of electrons occupy the ground state and sublevel, S_{00}. After absorbing a photon, the electron gets excited into some state S_{AB}, where $A >= 1$ and $B >= 0$. The electronic energy levels are near enough that the vibrational energy splitting causes some overlap between neighboring energy levels, such that an S_{40} electron can undergo radiationless internal conversion to some vibrational state of S_3, and quickly thermalize to S_{30} before converting to some vibrational state of S_2, and so on until it reaches the lowest excited state S_{10}. This whole process is dependent on molecular vibration, which is much more rapid ($\sim 10^{-12}\,\mathrm{s}$) than the process of spontaneous emission ($\sim 10^{-8}\,\mathrm{s}$), so these electrons normally reach S_{10} before emission.

The emission spectrum is therefore dependent upon the energy level S_{10} and the vibrational sublevels of the ground electronic state to which it can decay. A decay to any of the ground states results in an emission of a photon, which, due to energy lost in the internal conversion process, is lower energy than the absorbed photon. Thus we have wavelength shifting.

In the case where an absorbed photon results in an excitation directly from S_{00} (or the more sparsely populated vibrational states) to the lowest excited level S_{10}, the emitted photon could have similar wavelength to the absorbed photon. This leads to a slight self-absorption of the scintillation which varies from compound to compound.

It should be mentioned that a highly energetic photon ($\sim 10\,\mathrm{eV}$) would be capable of ionizing the π-bound electron. The scattered electron could then induce excitations in neighboring π orbitals before recombining.

The reader should now have a basic grasp of the wavelength shifting process. A full treatment of WLS scintillation would involve a discussion of the excited triplet states T_1, T_2... which exist alongside the singlet states. This is given in Appendix A.

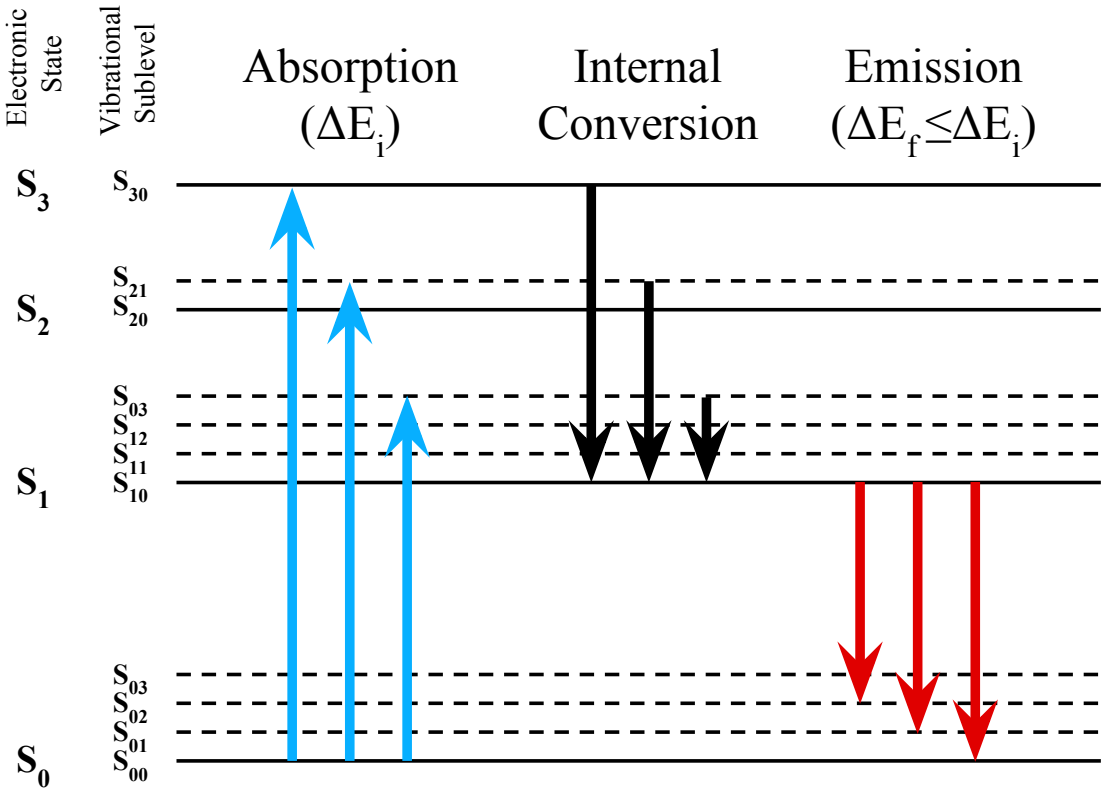

Figure 4.2: Energy level diagram of the wavelength-shifting process (inspired by [33]). At equilibrium, most electrons occupy the ground state S_{00}. After absorbing a photon and jumping up into an excited state, they undergo rapid and radiationless internal conversion to the lowest excited state S_{10}. The ΔE from this state to the vibrational sublevels of the ground state is less than the energy of the absorbed photon, so the emitted photon has a longer wavelength.

4.1.1 Choosing a WLS for Liquid Argon

There are three properties of WLSs that are of primary importance to light detection and are used to determine the optimal WLS for use in a given experiment. These properties are the absorbance and emission spectra, the re-emission lifetime, and the self-absorption rate. The most popular choice for liquid argon experiments is 1,1,4,4-Tetraphenyl-1,3-butadiene.

4.2 Tetraphenyl-Butadiene (TPB)

Tetraphenyl-butadiene (1,1,4,4-tetraphenyl-1,3-butadiene, or TPB) is an organic compound that exhibits wavelength-shifting properties. In the field of dark matter research, it is a common method of converting UV scintillation photons into longer wavelengths for efficient counting. A lot has been written about TPB over the years, so before delving into the attributes that make TPB the WLS of choice for liquid argon experiments, a brief summary will be given of some TPB papers that are of particular interest to dark matter detection.

4.2.1 History

The first measurements of TPB conversion efficiency as a function of incident wavelength were carried out in 1963 by Brunet et al., in which they found that TPB had significantly greater efficiency at converting vacuum-ultraviolet light than the widely used sodium salicylate [35]. This was confirmed again almost a decade later by Mai and Drouin in 1971, stating an efficiency three times that of sodium salicylate [36]. They also claim that the efficiency is at a maximum when the TPB is evaporated onto a surface to a density of $0.47\,\mathrm{mg/cm^2}$.

Interest in using TPB for commercial purposes began to grow, and in 1972 Burton and Powell published another study of TPB wavelength-shifting efficiency for UV astronomy [37]. They presented multiple efficiency curves with varying TPB thicknesses, claiming that the peak occurs at a surface density of $1.0\,\mathrm{mg/cm^2}$. This is at odds with the previous measurement by Mai and Drouin and those that came after.

With the advent of dark matter scintillation detectors in the 1990s, TPB was again looked at as a way to achieve efficient collection of UV light. A 1996 paper by Lally et al. claim an optimal TPB thickness of $\sim 0.1\,\mathrm{mg/cm^2}$ for shifting 175 nm light, near the xenon peak output wavelength [38]. They also show evidence of a

10%-15% degradation of the TPB efficiency over a six month period during which the samples were stored in sealed containers in the dark. They suggest that it is a result of oxidation and hydration of the compound.

Following shortly after Lally et al. is a 1997 paper by McKinsey et al. [39]. In it, they illuminate TPB with 58.4 nm (helium), 74.0 nm (neon), and 128 nm (argon) photons, and claim an optimal thickness of 0.2 mg/cm^2. They also show severe effects of exposing TPB to light. A 5 min exposure of TPB to a xenon UV lamp in atmosphere resulted in a reduction of pulse height by a factor of four. Exposure to fluorescent laboratory lighting in atmosphere over a 24 h period resulted in a factor of two reduction in pulse height.

After a decade of substantial growth in particle astrophysics, the use of TPB became widespread in neutrino and dark matter physics experiments. In 2011, Gehman et al. published a paper examining the TPB response to UV wavelengths in the range emitted by the noble liquids [40]. They found an optimal TPB thickness of 0.22 mg/cm^2, in agreement with McKinsey et al.

In 2013, an investigation into the mechanism behind TPB degradation was undertaken by Jones et al. for the LBNE experiment (now called DUNE) [41]. They found the degradation to be correlated with an increase in benzophenone, a UV-inhibiting impurity that is formed by photooxidation as the TPB sample was exposed to UV light. They show that the performance to TPB can be improved and the degradation can be delayed by forming a mixture with 20% 4-tert-butylcatechol, a free radical inhibitor.

The same year, another study of TPB scintillation efficiency as a function of thickness was published by Francini et al. [42]. They excited the TPB with a broad band of wavelengths using a xenon lamp. No significant variation in TPB efficiency was found for thicknesses between 0.35 mg/cm^2 and 1.45 mg/cm^2; however, they did measure a slight redshift in the emission peak, moving from 423 nm at 0.35 mg/cm^2

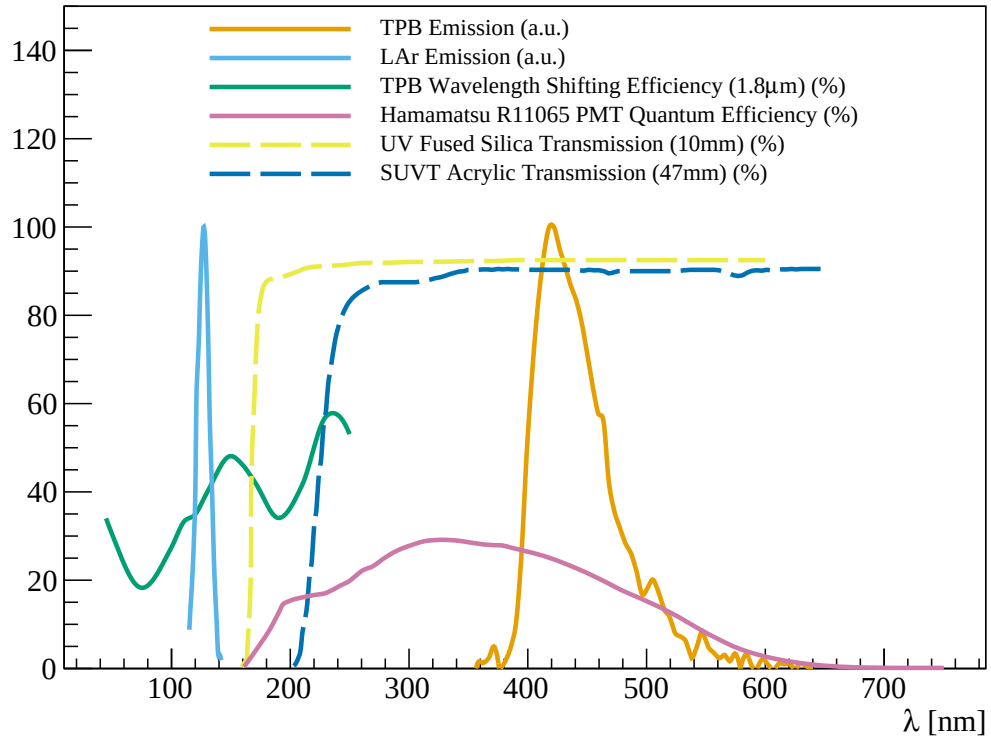

Figure 4.3: The motivation for using TPB in a liquid argon experiment. The TPB wavelength shifting region (blue-green) overlaps the LAr emission region (light blue). The TPB emission spectrum (orange) is ideal for transmittance through detector windows which are typically made with UV-grade fused silica (yellow) or acrylic (dark blue). The wavelength also matches the range for which many PMTs have peak quantum efficiency (violet). Curves obtained from [43, 40, 44, 45].

to 428 nm at 1.875 mg/cm^2. This is attributed to the thicker TPB having greater self-absorption, which affects short-wavelength light more due to its overlap with the absorption spectrum.

With this summary, we can see the major developments of TPB research that have taken place over the last 50 years as well as the general interest the scientific community has in the material. Other important TPB measurements, namely those involving direct stimulation of the TPB with alpha and beta radiation, deserve special attention due to their role in surface backgrounds. These papers will be discussed in Chapter 7.

4.2.2 TPB for Liquid Argon Experiments

TPB is the WLS of choice for most liquid argon experiments for several reasons.

First, the TPB absorption can absorb the 128 nm photons produced by the argon, and the emission spectrum is well aligned with the PMT efficiency curve and transmission curves for common window materials (see Fig. 4.3).

Second, the decay lifetime of excited TPB is short (<10 ns). This is of particular importance for liquid argon dark matter searches, as their primary means of rejecting electron recoil backgrounds (gammas, betas) is through pulse-shape discrimination (PSD). The longer the decay lifetime of the WLS, the more smeared out the primary signal becomes, which makes PSD more difficult.

Third, the vacuum evaporation procedure for coating TPB onto surfaces is simple and produces a layer of constant thickness over the surface. It can also withstand the stress of being exposed to liquid argon over a prolonged period.

Chapter 5

Alphas

An alpha decay occurs when the nucleus of a radioactive atom emits a particle comprising 2 protons and 2 neutrons, also known as a helium nucleus or alpha particle. The atom, which now has a reduced atomic mass and atomic number, is therefore a new element, and is called the "daughter" of the decay. The daughter may be stable, or it may be radioactive and decay again into another element, and so on. A line of successive decays is called a decay chain.

Radioactive elements can also undergo other types of decay, emitting beta particles (electrons) and gamma rays. When these interact with the argon they produce electron recoil signals, which LAr detectors are good at discriminating against (see Chapter 3). In contrast, alpha particles ("alphas") do not produce electron recoil signals in LAr and therefore deserve special attention.

5.1 Source of Alphas

Alphas can be readily found in nature. Elements such as uranium and thorium are naturally occurring, having been created in supernovae billions of years ago, eventually finding their way into the Earth's crust as it was forming. Their long half-lives

mean that they are still present today. They are the source of long decay chains which contain several alpha decays (see Fig. 5.1), as well as beta decays.

Trace amounts of these radioisotopes can be found to varying degrees in virtually every substance on Earth. Low background experiments, such as those searching for dark matter, utilize special materials that have been screened to ensure that they have exceptionally low levels of this radioactivity. Screening involves putting a sample of the material into a radiation counter that will measure alphas or gamma rays coming from the sample. This information is then used to estimate the abundance of different radioactive elements within the material.

A material that is too radioactive in this context does not mean that it is dangerous from a human health and safety point of view. To even be considered for a low background experiment, a material needs to be far lower in natural radioactivity than most things humans interact with daily (including other humans).

Alphas are a concern for LAr detectors both directly and indirectly. Directly, alphas themselves can produce signals in the argon. Alphas are charged and relatively slow (non-relativistic), so they lose energy quickly and cannot travel very far or penetrate through thick layers of material; nevertheless, if they are emitted within the LAr itself or on the interior surface of the detector, they can deposit all or some of their energy in the argon. While the typical alpha has an energy on the order of MeVs – well above the region of interest for a dark matter search – some alphas that get produced at a slight depth in the detector wall can lose a large fraction of this energy on their way into the argon, resulting in a more dangerous low energy NR-like signal. An alpha decay on the surface of the detector can also send the alpha into the wall and the recoiling nucleus into the argon, again producing a low energy NR-like signal.

Indirectly, alphas can hit another atom's nucleus and knock out a neutron in a so-called (α, n) reaction. This neutron, even if initially far from the detector, can

travel a long distance and find its way to the argon, producing a nuclear recoil signal that may look like dark matter. This indirect alpha-induced background typically falls under the umbrella of neutron backgrounds rather than alpha backgrounds, and is discussed in detail elsewhere [26].

5.2 "Upper" and "lower" decay chains

The uranium and thorium decay chains begin with several alpha and beta decays until they arrive at, temporarily, an isotope of radon. Unlike the prior elements in the chain, radon is a gas, and its gaseous nature gives it a greater ability to diffuse through the rock, steel, or other material in which it was produced and mix with the air – or in the case of DarkSide-50, the argon. Once mixed in with the bulk argon, the alpha decay from radon and the elements following it will produce clear signals in the detector.

Radon's unique behavior causes a splitting of the decay chain, with the elements coming before and after radon comprising the "upper" and "lower" chains, respectively.

The alphas in the upper chain are not often seen in detectors because they do not have enough energy to make it out of the material and into the detector medium unless they happen to be extremely close to the surface (a 5 MeV alpha loses 100% of its energy after travelling only 10 µm in steel [46]).

This thesis is interested in alphas that directly produce signals in the detector, and will therefore be focused on alphas from the lower decay chains.

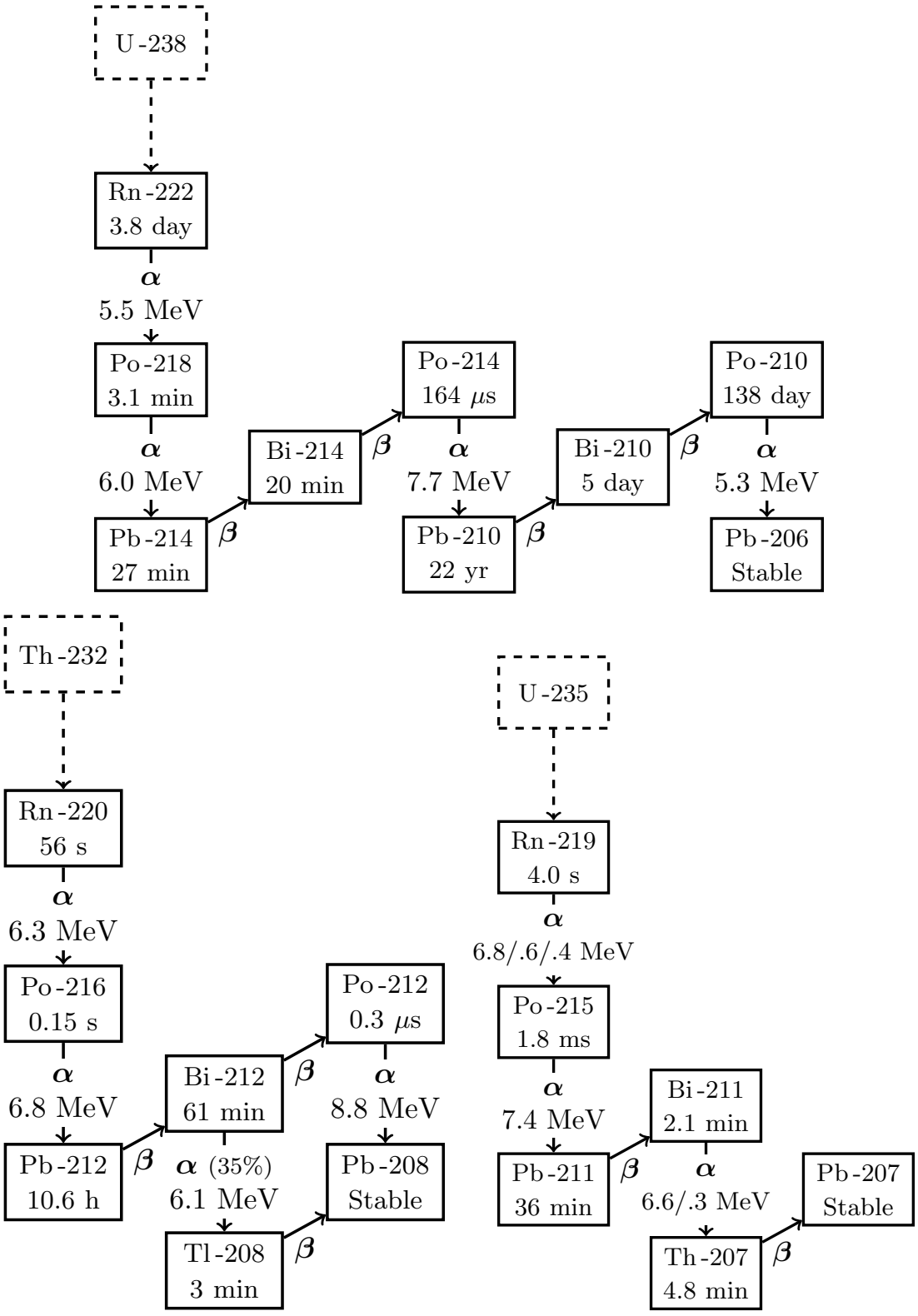

Figure 5.1: Naturally occurring decay chains. The times listed are the half-lives. Shown in solid black are the lower parts of the chains beginning with Rn.

Chapter 6

Surface Backgrounds

Surface backgrounds, in the context of scintillation counting experiments, are undesired scintillation events originating on the surface of the detector—such as a wall or a window—that is containing the target volume. A primary example is ^{210}Po, a radioisotope that undergoes alpha decay with a half-life of 138 days. It is part of the naturally occurring ^{222}Rn decay series, and can be introduced onto the detector surfaces if they come into contact with even trace amounts of radon or its daughters.

Completely clean surfaces are unattainable, so surface backgrounds are ordinarily suppressed by making position-based cuts. This involves throwing out all the events that occur near the surfaces, effectively reducing the volume of the target to an inner "fiducial" volume. Depending on the precision of the position reconstruction algorithm, substantial fiducial cuts may be needed to suppress this background, particularly in dark matter experiments that try to avoid even a single background event. It is not uncommon to lose 50% of a detector's target mass to fiducial cuts [47].

Alternative methods for surface background rejection, such as the one described in Sec. 7.2, could allow experiments to retain significantly more of their target volume. This has an enormous impact on the current generation of detectors, as a doubling of the fiducial volume amounts to a doubling of the exposure. It also impacts future

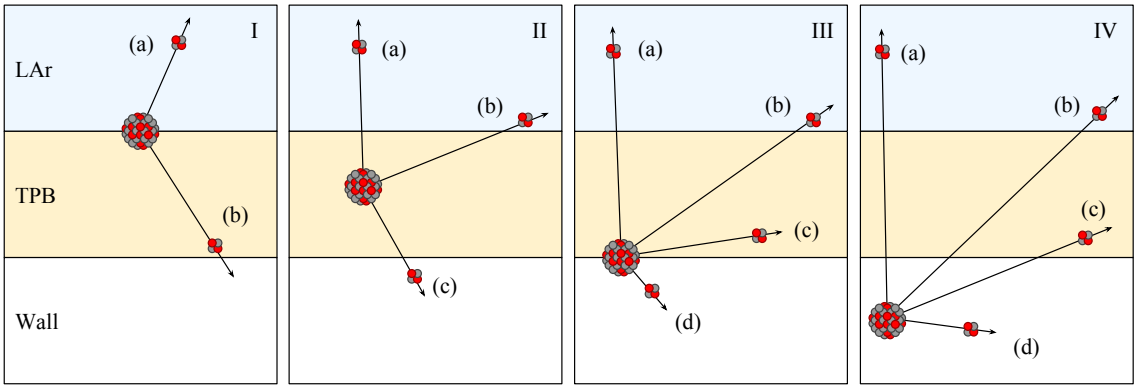

Figure 6.1: Alphas decay modes on the surface of a liquid argon detector depend on the origin of the radioisotope. Significant scintillation is expected whenever an alpha travels through LAr or TPB, or when the nucleus travels through LAr. Of particular concern is decay mode I(b), which has a low energy signal produced in the liquid by the recoiling nucleus, as well as decay modes (II-IV)(b), which have low energy signals produced in the liquid by a degraded alpha. Decay modes (II-IV)(c) produce scintillation only in the TPB, but this can still be a concern for experiments that do not rely on charge collection.

experiments that aim to achieve a given exposure by lowering the necessary target volume required and thereby reducing the cost.

6.1 Surface Decay Modes

The presence of TPB on the surfaces of a LAr detector presents a complicated picture for the decay modes of the radioisotope. A variety of signals can be produced depending on the location of the isotope and the direction of the decay products. The possible modes for surface alpha decays are illustrated in Fig. 6.1. Each case will be examined and its potential for creating a concerning background will be discussed.

(I-IV)(a): The alpha deposits a large fraction of its energy (∼MeV) in the LAr. This mode does not pose a background for detectors looking for low energy interactions.

I(b): The alpha is directed toward the wall, and deposits some or all of its energy in the TPB, depending on the angle. The recoiling nucleus can be ejected from the surface into the LAr and produce a low energy nuclear recoil, a potential background.

(II-IV)(b): The alpha is degraded as it passes through surface material, and has the potential to be degraded enough to fall in the detector's low energy search region.
(II-IV)(c): No signal is produced in the LAr, but the alpha will still produce a signal in the TPB. The alpha scintillation in TPB is known to be heavily quenched [48], so this could result in a low energy signal. It could pose a background for experiments that do not depend on charge collection from interactions in the LAr.
(III,IV)(d): The alpha is emitted directly into the detector wall. Alpha scintillation has not been seen in the common detector wall materials, such as Teflon, fused silica, or acrylic, so these modes do not pose a background. The recoiling nucleus ($\sim$100 keV) does not have enough energy to reach the LAr.

This examination of the surface decay modes reveals that each mode carrying a risk of background features some amount of alpha scintillation in TPB. It is therefore useful to study this process, because if it produces a signal that significantly differs from a nuclear recoil in LAr, it can be used to reject surface backgrounds. The results of a dedicated study of the behavior of TPB under various forms of radiation is detailed in Chapter 7.

Chapter 7

Radon Daughter and Organic Scintillator Experiment (RaDOSE)

The **Ra**don **D**aughter and **O**rganic **S**cintillator **E**xperiment was designed and operated at Princeton University by Chris Stanford, Jingke Xu, and Shawn Westerdale, with help from Allan Nelson.

7.1 Overview of the Detector

A diagram of the detector can be found in Fig. 7.1. It consists of two stainless steel chambers separated by a quartz window, which forms a hermetic seal with a Teflon gasket. The upper chamber houses a single Hamamatsu R11065 photomultiplier tube (PMT) directed downward at the window. The PMT has a negative HV base [49] and is typically biased at -1300V. The lower chamber, measuring approximately $230\,\mathrm{cm}^3$, is lined with 1 cm-thick Teflon, forming a reflecting cup. Samples containing TPB are placed into this cup with radioactive sources. The chambers are connected to a Pfeiffer turbopump [50], which is capable of producing a 10^{-6} mbar vacuum in the lower chamber. The system is connected to a high purity (99.9997%) argon gas bottle obtained from Airgas Specialty Gases, with ~ 1 ppm N_2. The N_2 was further reduced

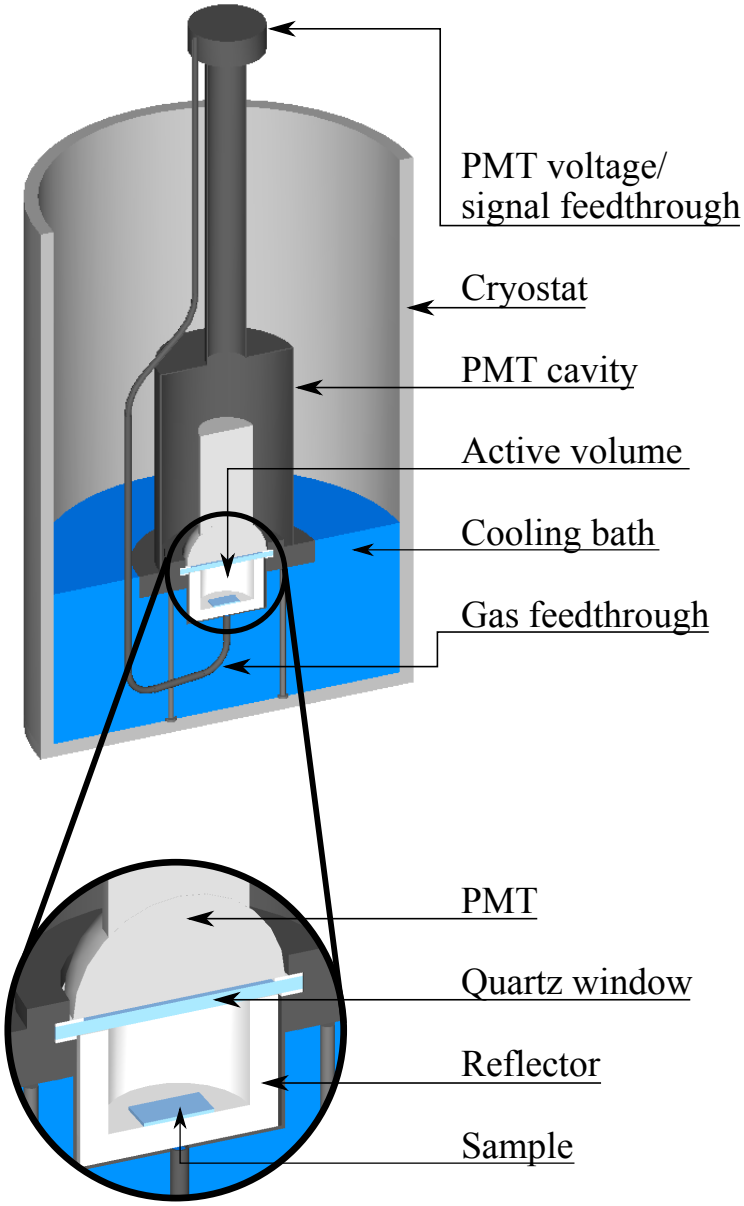

Figure 7.1: A cutaway view of the detector. The zoomed inset of the lower chamber shows the sensitive volume where the samples are placed.

with a SAES getter [51], allowing the chambers to be filled with scintillation-grade argon. The pressure in the upper and lower chambers is monitored with a pair of OMEGA DPG1000B-30V100G pressure gauges.

The detector is mounted on three legs, allowing it to stand upright, and to be lowered into the bottom of an open double-walled dewar. The dewar can then be

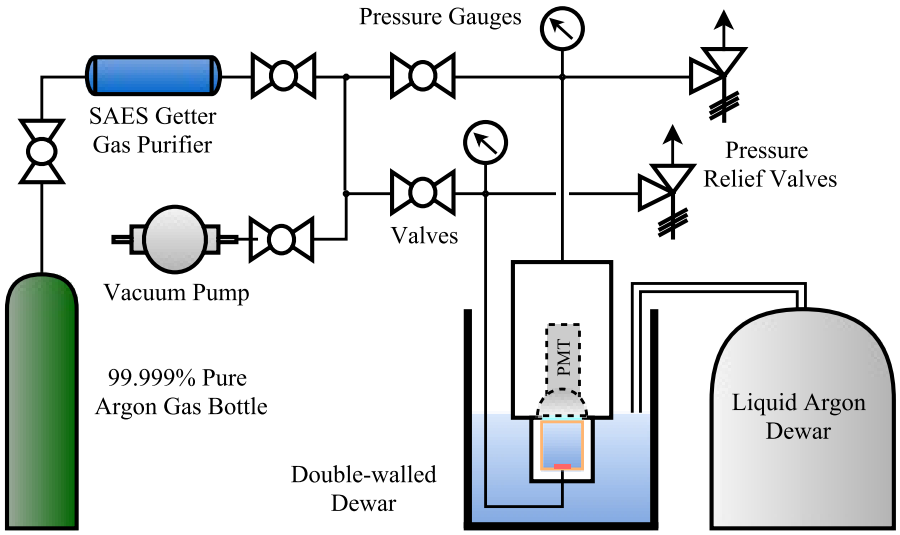

Figure 7.2: The RaDOSE support system

filled with liquid nitrogen (LN_2) to perform cryogenic vacuum measurements, or filled with LAr to condense the argon gas in the system to study LAr scintillation.

After a measurement with LAr, it takes 24 to 36 hours for the liquid in the dewar and the detector to evaporate and for the system to reach equilibrium with the lab temperature. Each chamber has a pressure relief valve set at 5 psig to release the high pressure gas that forms when the liquid argon inside the detector evaporates during this process.

A schematic of the support system for RaDOSE can be found in Fig. 7.2. The entire system was checked with a Pfeiffer leak detector [52] and found to have a leak rate below 10^{-7} mbar L/s.

The data acquisition system consists of an analog amplifier and a CAEN V1720 analog-to-digital converter [53] with a 4 ns sampling rate. The digital signal is delivered to a PC via a CAEN A2818 optical controller and recorded with the Daqman software [54]. Daqman is also used to process the raw waveforms and analyze the data.

7.1.1 Design

RaDOSE was designed to study the alpha scintillation from ^{214}Po, obtained by exposing a sample material to ^{222}Rn. The source's lifetime was therefore set by the longest-lived radon daughter prior to ^{214}Po, which is ^{214}Pb with a 27 min half-life. The short lifetime of the source drove several key features of RaDOSE's design, which might otherwise seem strange.

The primary goal was to start with a warm detector, which had just been exposed to the lab air while inserting the sample, and be able to take data with high purity liquid argon in under three hours, before the sample decayed away.

The triplet state of argon scintillation (see Sec. 3.2) is highly sensitive to N_2 contamination, even at the ppm level [55]. After it was exposed to N_2 during sample placement, the detector had to be pumped down to a vacuum and purged with high purity argon several times to flush the system of N_2. The speed at which this can be done is directly proportional to the volume being flushed, hence the choice of having two volumes hermetically separated by a window. The small, lower volume, which contains the liquid argon, could be pumped down to 10^{-6} mbar in a just a few minutes. The larger, upper volume, which houses the PMT, also went through several pumping and purging cycles, but not the the same extent. This was done to reduce the N_2 concentration of any gas that might leak from the upper chamber to the lower through the Teflon gasket.

A closer view of the Teflon gasket and quartz interface can be seen in Fig. 7.3.

Ultimately, the design proved to be flexible and allowed us to make many different measurements that were not conceived of until after the construction. The sealed window design allowed us to pump the detector cavity down to vacuum to make measurements of alphas unimpeded by air, while the PMT remained at atmospheric pressure in the upper chamber where it could dissipate heat.

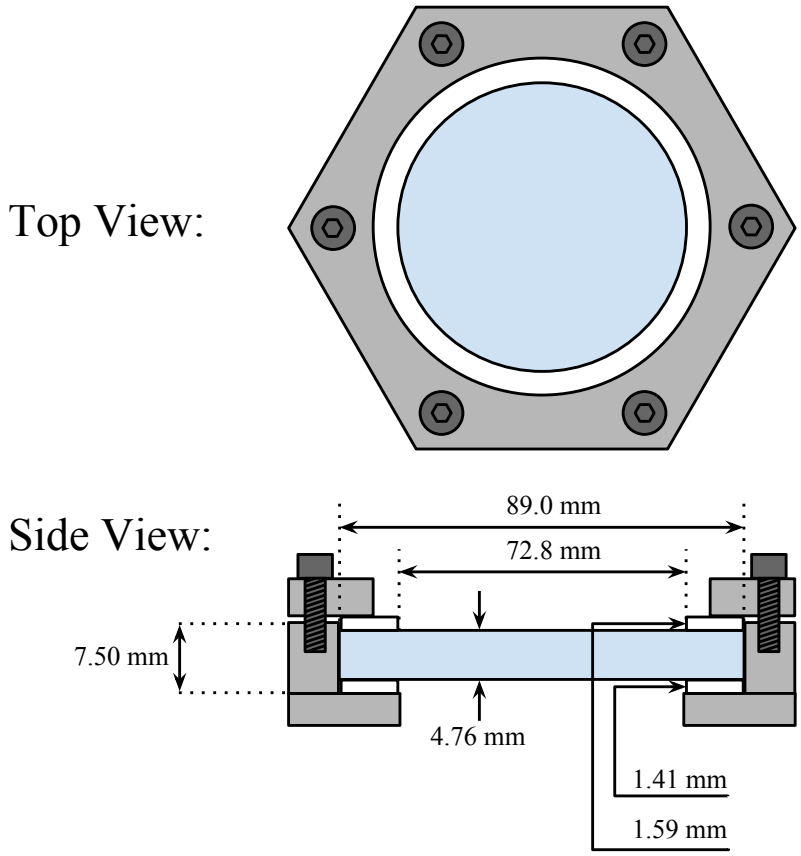

Figure 7.3: Dimensions of the window seal in the RaDOSE detector.

7.1.2 Pictures

Pictures of the TPB evaporation chamber and the radon deposition system can be seen in Fig. 7.4. More details about these two systems can be found in [56].

Pictures of the exterior and interior of RaDOSE can be seen in Fig. 7.5 and 7.6, respectively.

A picture of a TPB-coated quartz slide used to perform a measurement can be seen in Fig. 7.7 under illumination from a UV lamp.

(a) The TPB vacuum deposition system.

(b) The radon deposition system

Figure 7.4: The TPB vacuum deposition system and the radon deposition system.

7.2 Measurements

The lower chamber was configured in different ways to study different sources. These configurations can be seen in Fig. 7.8(A-D). The scintillation response of TPB was measured for alphas and betas in a vacuum (A&B), for alpha decays from radon daughters in LAr (C), and for 128 nm photons in LAr (D).

The purpose of the vacuum measurements was to determine the response of TPB to various forms of ionizing radiation, while the purpose of the radon daughter measurement was to produce the expected background signal from actual surface events that could be seen in a LAr detector (decay mode I(b) in Fig. 6.1). The final measurement involving 128 nm photons was required to compare these results to TPB-shifted scintillation light produced by a regular interaction in the bulk LAr.

(a) The RaDOSE detector.

(b) The lower volume with the gas flow tube.

Figure 7.5: The RaDOSE exterior.

(a) The quartz window seal between the upper and lower volumes, with TPB evaporated on the surface. Some measurements used a clear window without TPB.

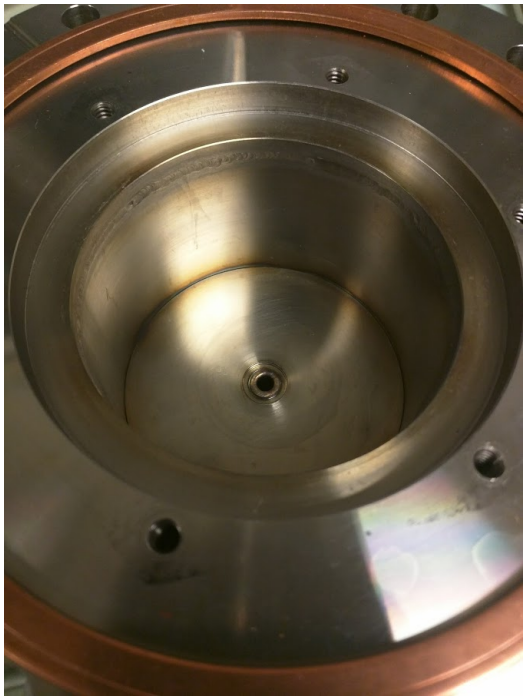

(b) The empty lower volume before the reflector and sample are placed inside.

Figure 7.6: The RaDOSE interior.

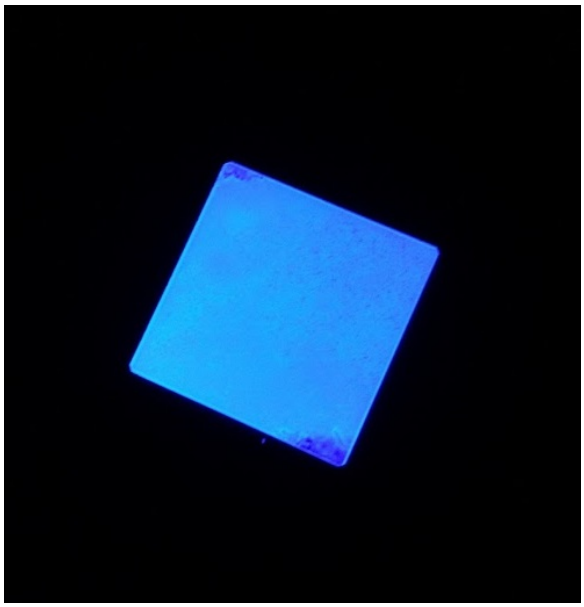

Figure 7.7: A TPB-coated quartz slide under illumination from a UV lamp.

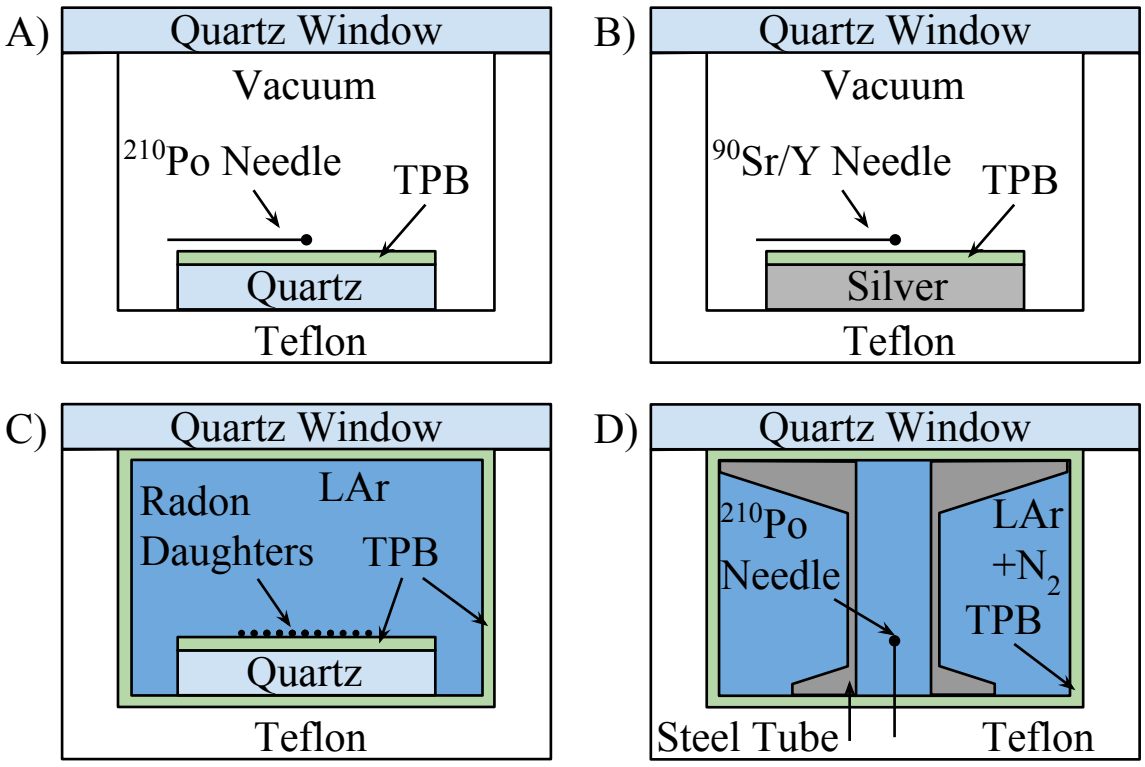

Figure 7.8: Diagrams of the detector configurations for the different measurements.

7.3 Procedure

Measurement A: Vacuum Alphas (Fig. 7.8A)

For the first measurement, a ^{210}Po alpha needle source (E=5.3 MeV) was secured with PTFE tape to the top of a quartz slide coated with ($205 \pm 10\,\mu g/cm^2$) TPB. The slide was placed in the detector, and the chamber containing the source was pumped down to 10^{-3} mbar.

Prior to TPB deposition, the quartz slide was cleaned in an ultrasonic bath for thirty minutes and left to bake in a vacuum oven at 120°C for a minimum of five hours. This procedure was followed for all substrate materials used in the different studies.

The measurement was performed at two temperatures: ambient lab temperature (295 K) and LN_2 temperature (77 K). To obtain the LN_2 temperature data, the bot-

tom half of the detector (the entirety of the lower chamber) was submerged in LN_2. Measurements were recorded after the detector had been submerged for 1 hour to allow enough time for the TPB to reach equilibrium with the LN_2.

Measurement B: Vacuum Betas (Fig. 7.8B)

The TPB scintillation response to beta excitation was measured using a ^{90}Sr/Y needle source [57], a nearly-pure beta emitter ($I_\gamma \sim 0.01\%$) [58]. The source was fastened to a pure silver slide coated with TPB using PTFE tape. Since betas have a higher penetrating power than alphas, a thicker layer ($1290 \pm 50\,\mu g/cm^2$) of TPB was used to capture more of the beta energy. The silver slide was chosen to prevent the release of Cherenkov light from the substrate when the beta passes through the TPB and enters the slide material.

The beta response was observed at lab temperature and LN_2 temperature in the same manner as the alpha measurements.

Measurement C: Surface Decay in LAr (Fig. 7.8C)

The full signal from a surface decay includes the 128 nm light produced by the recoiling nucleus in the LAr. A layer of ($265 \pm 50\,\mu g/cm^2$) TPB was evaporated onto the quartz window and Teflon reflecting cup to shift this light to longer wavelengths.

The quartz slide was coated with the same thickness of TPB, and was left for ten hours in a chamber filled with argon and ^{222}Rn gas obtained from a ^{226}Ra source. The slide was then removed from the radon chamber and the initial activity was measured with a Geiger counter to be about 500 Bq, or $100\,Bq/cm^2$. The slide was then immediately placed in the Teflon cup and the detector was closed and pumped down to a vacuum. The detector was purged with clean argon gas several times to remove N_2 gas from the system.

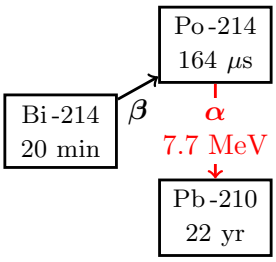

Figure 7.9: The ^{214}Po alpha decay observed in Measurement C. A delayed coincidence search with the preceding ^{214}Bi decay provides efficient means for reducing the background in this measurement.

After achieving a 10^{-6} mbar vacuum, the detector was filled with gas from the argon purification system. The detector was placed in an empty dewar which was then filled with LAr until the lower chamber was submerged. As the argon gas in the lower chamber condensed into a liquid, it drew in more gas from the system. This continued for 2 hours until the lower chamber was filled with LAr, submerging the quartz slide. Data collection began once the gas flow through the purification system ceased, indicating that the chamber was in equilibrium with the surrounding LAr bath. Later, the detector was cooled down with the PMT and upper chamber removed, and it was verified by observing the liquid level through the quartz window that the lower chamber is completely filled with liquid once it reaches equilibrium and the gas flow rate from the argon bottles ceases.

The alpha decay of interest for this measurement was the decay of ^{214}Po. ^{214}Po's short half-life of 164 µs allows it to be tagged by its delayed coincidence with the preceding beta decay of ^{214}Bi (see Fig. 7.9) for a substantial reduction in background.

Measurement D: LAr 128 nm photons (Fig. 7.8D)

The TPB-coated quartz window and Teflon cup from the radon daughter study remained in the detector for this measurement. A ^{210}Po needle source was stuck into the bottom of the cup, standing upright so that the eye of the needle was in the center of the volume, far from any TPB surfaces.

To produce prompt 128 nm light pulses in the detector, the detector was fed a mixture of roughly 99.9% Ar and 0.1% nitrogen. N_2 is known to heavily quench the light production from the longer-lived triplet state of argon. A dedicated study of this phenomenon can be found in [55], which showed that the triplet state disappears at the 500 ppm level. Since our measurement was not concerned with light yield, we surpassed this concentration to ensure that when the alpha from the needle interacted with the liquid, the resulting pulse would be fully prompt with no measurable late component. Thus, any longer time structure in the measured pulses could be attributed to the response of the TPB to the 128 nm light.

Note that the 5.3 MeV ^{210}Po alphas, when depositing their full energy in LAr as they do here, would produce enough light to saturate the digitizers. To avoid this, a 1.3 cm diameter stainless steel tube was placed upright in the detector, coaxial with the needle source. The tube drastically reduced the light yield, as the 128 nm LAr light had only a small solid angle through which to escape the tube and reach the TPB.

7.4 Pulse Shapes

In analyzing the TPB scintillation from ^{210}Po alphas (Measurement A), it was discovered that a significant fraction of the scintillation light had a lifetime on the order of milliseconds. This is orders of magnitude longer than previously reported TPB scintillation lifetimes [59, 60]. An example of a waveform from a single interaction of an alpha in TPB can be seen in Fig. 7.10.

The milliseconds-long lifetime of the TPB scintillation is also orders of magnitude longer than that of pure argon scintillation, for which the longest-lived component has a lifetime of only 1.4–1.6 µs, depending on argon purity [61]. Therefore, if the magnitude of this "tail" is substantially different between alpha excitation and the

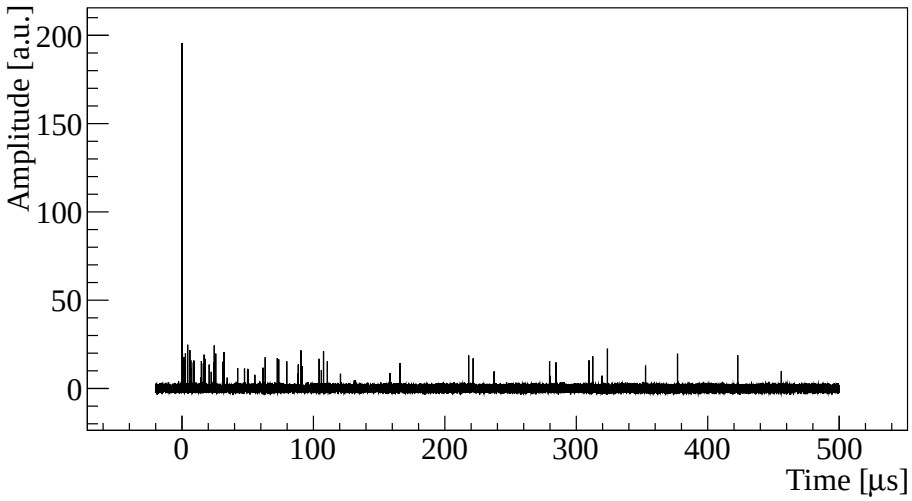

Figure 7.10: A single waveform from alpha scintillation in TPB at LN_2 temperature. The prompt occurs at Time=0 and has a lifetime of a few nanoseconds, while the late component has a lifetime of milliseconds. The small pulses throughout the tail of the pulse are made up of single photoelectrons.

UV wavelength shifting process, PSD could be used to get a strong suppression of surface events.

The results of the remaining measurements with betas and UV photons led to the discovery that while the TPB tail is still present under these forms of excitation, its magnitude is greatly reduced. The results are compared through the use of average waveforms.

Average Waveforms

Thousands of waveform samples were collected for each measurement. Data selection cuts were applied to remove waveforms containing PMT afterpulses, pileup pulses, or Cherenkov backgrounds (characterized by large, entirely prompt pulses). The systematic uncertainties introduced by these cuts were studied by comparing the results with and without these cuts, and are included in the final results.

The waveforms passing the cuts for each configuration were summed, with each waveform weighted by its integral. The summed waveforms were then normalized to an integral of 1, which we call the average waveform (AW).

The AWs exhibit both high intensity at short timescales and low intensity at long timescales, so it is useful to display them on log-log axes. Before computing the AW, the time axis for each waveform was divided into exponentially increasing bin sizes, such that the bin widths would appear constant on a log axis. The average value of the waveform within each bin was then used to compute the AW.

After the AWs were obtained, they were passed through a deconvolution algorithm to remove the smearing effect of the single-photoelectron response of the PMT. This response of the PMT was obtained using a HORIBA NanoLED pulsed picosecond laser of similar wavelength to the TPB emission spectrum.

The final AW for each measurement can be seen in Fig. 7.11.

Several measures were undertaken to study other sources of systematic uncertainties. First, background runs were taken without a radiation source to quantify the baseline noise and dark count rate of the PMT, as well as external backgrounds in the LAr like gammas and cosmogenic muons. Second, multiple PMTs were used to verify that the TPB tail was not a result of a faulty detector. Third, multiple substrates were tested under alpha excitation, including quartz, Teflon, acrylic, and silver, to verify that the scintillation was coming only from the TPB and not the substrate itself. Fourth, every trigger of the data acquisition system recorded a minimum of 50 µs prior to the trigger to ensure a clean baseline before an event.

The external background rate in the LAr configurations was measured to be less than 1 Hz, thanks to both the lead shielding surrounding the detector and the detector's small target mass. The LAr Measurement C removes this background with the ^{214}Bi–^{214}Po delayed coincidence search. Measurement D, which looks for MeV-scale

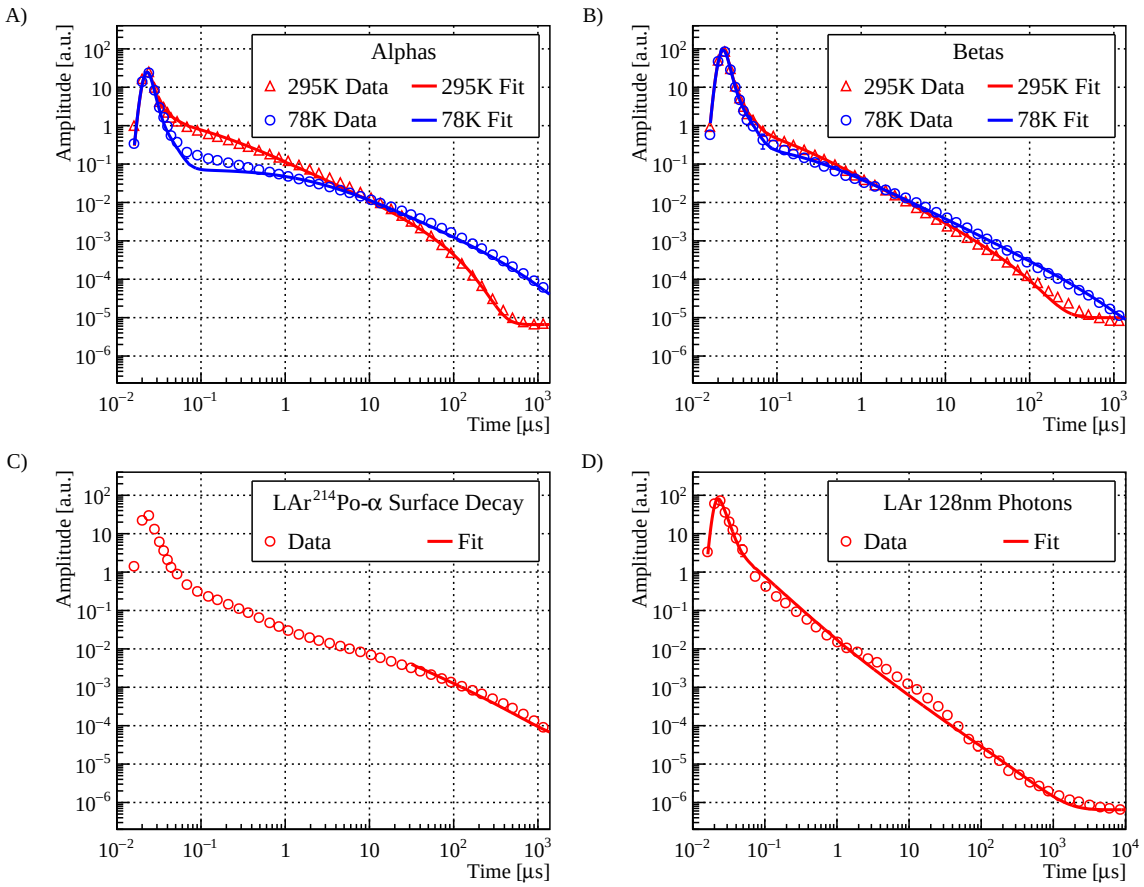

Figure 7.11: The average waveforms of TPB scintillation pulses from different sources and under different conditions. **Top:** Measurements A and B involving alpha and beta needle sources at room temperature and LN_2 temperature. **Bottom left:** Measurement C involving surface alpha decays in LAr. **Bottom right:** Measurement D involving the 128 nm photons from LAr scintillation.

signals from alpha depositions in LAr, eliminates the external background by setting a high energy threshold.

The TPB tail remained unchanged with different PMTs, and no measurable scintillation was found from alpha excitation in the tested substrates. The baseline noise and dark rate can be directly seen in the AWs, and will be discussed with the waveform fitting procedure.

The Model

The long tail of the AWs does not follow an exponential decay process. Rather, the shape resembles a power-law decay with an exponential cutoff. In [62], R. Voltz and G. Laustriat describe this behavior using a model of the scintillation process of organic compounds which considers both the prompt and delayed response of the scintillator. The following is a summary of their model.

Voltz and Laustriat Model

After ionizing radiation is absorbed by the compound, the electrons fall into excited singlet and triplet states. The singlet states decay quickly while the triplet states have a longer decay lifetime and produce a "delayed" signal. This process is not represented simply by an extra exponential term, because in regions of the scintillator that have received high levels of ionization, such as the track produced by an alpha particle, intra-molecular interactions become significant; triplet states can be destroyed through triplet-triplet annihilation with timescales related to the diffusion of these dense pockets of ionized species.

The full equation describing the instantaneous intensity of the scintillation versus time takes the form:

$$I(t) = I_p(t) + I_d(t)$$

where $I_p(t)$ and $I_d(t)$ represent the instantaneous intensities of the prompt and delayed components, respectively. $I_p(t)$ is a result of the decay of the short-lived singlet states and is represented by an exponential:

$$I_p(t) = \frac{N_p}{\tau_S} \exp(-t/\tau_S)$$

where N_p is the total integrated intensity of $I_p(t)$ and τ_S is the lifetime of the singlet states.

The instantaneous intensity of the delayed component, $I_d(t)$, is derived by considering the diffusion of densely packed triplet states and their interactions with each other. The full form of $I_d(t)$ is cumbersome, but a simplification can be made for $t \gg \tau_S$, and can be justified by the fact that $I_p(t)$ is dominant in the $t \sim \tau_S$ regime by several orders of magnitude. The simplified form is:

$$I_d(t) = \frac{N_d}{\tau_d} F(t)$$

Where N_d is the total integrated intensity of $I_d(t)$ and $\tau_d = \int_0^\infty F(t)\mathrm{d}t$. $F(t)$ is defined as:

$$F(t) = \frac{e^{-2t/\tau_T}}{\left\{1 + A\left[\mathrm{Ei}(-\frac{t+t_a}{\tau_T}) - \mathrm{Ei}(-\frac{t_a}{\tau_T})\right]\right\}^2 (1 + t/t_a)}$$

Where:

- τ_T is the lifetime of the triplet state,
- t_a is a time constant defined as $t_a = r_0^2/4D_T$, where r_0 is the characteristic width of the ionization track and D_T is the diffusion coefficient of the triplet states,
- $A = \frac{t_a}{2t_b} \exp\left(\frac{t_a}{\tau_T}\right)$, where $t_b = [\chi_{tt} C_T(0)]^{-1}$, with χ_{tt} being the rate constant for bimolecular quenching of triplet states and $C_T(0)$ is the initial concentration of triplet states,
- $\mathrm{Ei}(-x) = -\int_x^\infty \frac{e^{-\alpha}}{\alpha}\mathrm{d}\alpha$ is the exponential integral.

Visually, $F(t)$ looks flat up until t_a, then it transitions to a power-law decay, which appears as a straight line on a log-log plot, with the slope affected by A. After reaching $\tau_T \gg t_a$, the exponential term begins to dominate, cutting off the power-law.

Fitting the Model to Data

The formula $I(t)$ given by Voltz and Laustriat underwent two modifications before it was fit to the data.

The first modification to the fit function was a result of the fact that the rise-time of the event was not completely removed by the PMT response deconvolution. This could be due in part to very small variations in the arrival time of emitted photons caused by the reflector and detector geometry, and in part to the discrete 4 ns sampling rate. To account for this, a Gaussian term $G(t; \mu, \sigma)$ was convolved with $I(t)$.

The second modification was due to the presence of an intermediate component that could not be fit by the function as given. A much better fit was found by introducing an additional exponential term ($\tau \sim$10 ns) to fit the intermediate region. A possible explanation for this component is the simplification made in the Voltz and Laustriat model that treats the prompt and delayed components as separate processes. This simplification may be invalid during the transition between the two timescales, where neither process is dominant. The addition of the exponential term to model this region is an empirical change only, and is not suggested to correctly describe the underlying physics.

After the addition of the Gaussian convolution term and the intermediate component $I_m = N_m \exp(-t/\tau_m)/\tau_m$, with integrated intensity N_m and lifetime τ_m, the full fit function becomes:

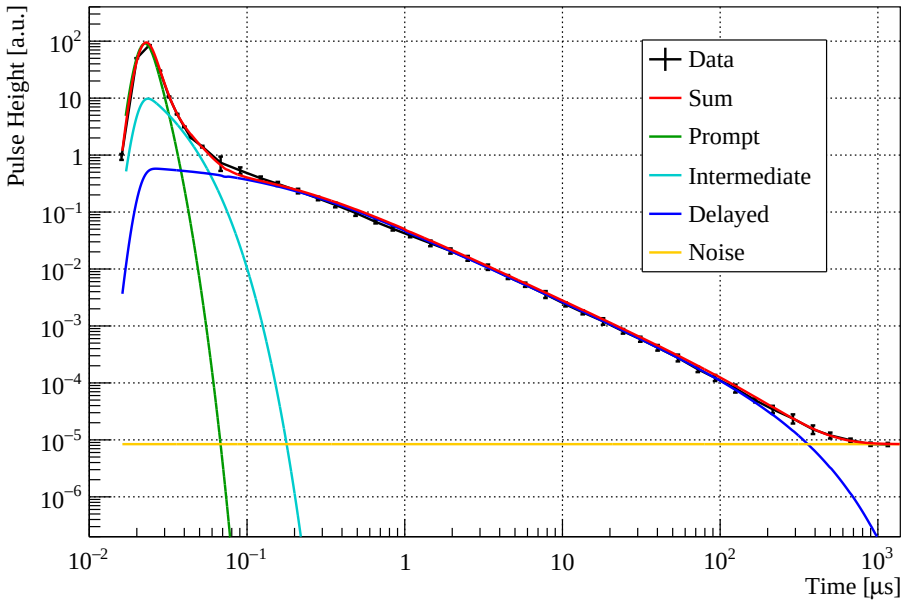

Figure 7.12: A breakdown of a fit to an average waveform showing the different components of the fit function. This average waveform comes from the scintillation of betas in TPB at room temperature.

$$I_{fit}(t) = G(t;\mu,\sigma) * \Big(I_p(t;N_p,\tau_S) + I_m(t;N_m,\tau_m) + I_d(t;N_d,A,t_a,\tau_T) \Big) + C$$

where C represents a constant rate from dark counts and baseline noise. Since C does not represent any component of the TPB scintillation, this term is subtracted after the fit and a re-scaling is performed on each of the integrated intensity terms such that $N'_x = N_x/(N_p + N_m + N_d)$ for $x = p, m, d$. Doing this allows N'_p, N'_m, and N'_d to be interpreted as the faction of light of the TPB scintillation that is due to the prompt, intermediate, and delayed components, respectively.

An example of a fit showing the different components can be seen in Fig. 7.12.

In the case of radon daughter measurement shown in Fig. 7.8C, only the tail of the AW was fit. This is because at $t < 10\,\mu s$ there are additional components from the

Description	N'_p	τ_S(ns)	N'_m	τ_m(ns)	N'_d	A	t_a(µs)	τ_T(µs)
Betas @ 295K	0.62(4)		0.14(5)		0.24(3)	0.15-0.30	0.05-0.20	100-500
Alphas @ 295K	0.15(3)	< 5	0.051(2)	11(4)	0.80(2)	0	0.08-0.2	
Betas @ 77K	0.60(3)		0.13(3)		0.26(2)	< 0.052	0.1-0.3	1000-5000
Alphas @ 77K	0.17(1)		0.033(2)		0.80(3)	0	1-2	
Surface Decay	-	-	-	-	0.84(5)	0		
128nm photons	0.73(3)	5.2(10)	-	-	0.27(3)	1.9(3)	0.078(20)	

Table 7.1: The parameters for $I_{fit}(t)$ when fit to the average waveforms for each measurement. The total errors, which are dominated by systematics, are shown in parentheses, with n digits in parentheses indicating the error on the last n digits.

argon scintillation of the recoiling nucleus [48], which are not included in the model. The fraction of light in the delayed component, N'_d, is the most valuable parameter for this study, and can still be extracted from this fit.

In the case of the 128 nm photon measurement, the two exponentials $I_p(t)$ and $I_m(t)$ were smeared out by the width of the signal, which is set by the lifetime of the singlet state of excited argon. For this fit the $I_m(t)$ component was dropped, and $I_p(t)$ can be considered as the effective lifetime of prompt argon scintillation light after being shifted by TPB. The lifetime of the prompt argon scintillation is not known to high enough precision for there to be a value in deconvolving this signal [61].

The fitted parameter values for each AW can be found in Table 7.1. Several of the parameters were subject to constraints to guide and ease the computational burden on the fitter and will be discussed.

Fit Constraints

Several measures were taken to reduce the total number of free parameters that the fitting algorithm had to deal with.

The constant term C representing the noise was constrained to be within 1σ of a constant fit to the 50 µs baseline region of the AW preceding prompt. The trigger threshold for the data acquisition was set above the single photoelectron threshold to avoid biasing this value. Otherwise, an uncorrelated photoelectron could occur in

the tail of the pulse, but not the in the pre-prompt region (because it would have triggered the data acquisition system).

Since the AWs were normalized to 1, the term N_d could be eliminated be redefining it as $N_d = 1 - N_p - N_m - C \cdot t_{\max}$, where $t_{\max}$ is the size of the integration window.

Several parameters were expected *a priori* to be independent of temperature and radiation type. These are μ, which depends on the arbitrary definition of the start of the pulse, and σ, which depends on the optics of the light collection and the digitizer resolution. The lifetime of the singlet to ground state transition, τ_S, was also suspected of being independent.

The lifetime of the triplet to ground state transition τ_T is an intrinsic property of the TPB and should be independent of the radiation type. However, phosphorescence has been known to depend on temperature [63], so τ_T was only fixed across measurements of the same temperature. Degradation of the TPB from exposure to the lab environment (see [38, 39, 41]) may also impact τ_T, but this has not been studied.

After an initial fit of each AW with all parameters left free, μ, σ, τ_S were found to remain constant within statistical errors from one fit to the next as expected. The intermediate component lifetime, τ_m, for which the origin is uncertain, was also found to remain constant. The Gaussian parameters μ and σ had mean values of 21 ns and 2 ns, respectively.

These parameters were then fixed to their mean values from the previous fits, and a second fit was performed to each waveform with fewer free parameters. These are the results shown in Table 7.1. The variance of each parameter's value between the free and constrained fits is included in the systematic errors.

Discussion

There are several observations to be made regarding the results of the fit.

The waveforms for alphas at room temperature and LN_2 temperature each have combined prompt and intermediate (N'_p and N'_m) values of around 0.2, indicating that in these cases the delayed component ($N'_d \sim 0.8$) is in fact the dominant component. This confirms the earlier observations by eye that alpha scintillation in TPB had a large tail. The fitter also strongly preferred a null value for A for alpha scintillation. In terms of the Voltz and Laustriat model, this means that the product $\chi_{tt}C_T(0)$ must be small, where χ_{tt} is the rate constant for bimolecular quenching of triplet states and $C_T(0)$ is the initial concentration of triplet states. It is unclear why either of these values would be smaller for alpha scintillation than for other forms of radiation. It is possible that this is simply an insufficient model for the alpha data.

The fitter also favored $A = 0$ for the in-situ surface background measurement with radon daughters. Since only the tail of this function was fit ($t \gg t_a$), this caused the parameter t_a to become degenerate with N_d. Therefore t_a became a fixed parameter and was set to the value obtained by the fit to the AW of alphas at LN_2 temperature.

The intermediate region of the alpha AW at LN_2 temperature is not well fit, indicating that our introduction of an extra exponential term for this region may be an oversimplification.

For betas, the delayed component was significantly smaller than for alphas, but still non-negligible with $N'_d \sim 0.3$. However, the beta particles have higher penetrating power, and often pass through the TPB while depositing only a small fraction of their overall energy ($\sim 0.1\%$ for 500 keV betas in 2 µm-thick TPB [64]), producing a smaller absolute pulse size compared to alphas. Thus, in practice, this tail was much harder to notice. Observing beta scintillation in thicker (mm) layers of TPB could be an interesting future study.

For both alphas and betas, there was an observed temperature dependence. While the fraction of light in the delayed component remained nearly constant, the observed triplet lifetime τ_T increased by an order of magnitude when going from warm to cold.

This is consistent with observations of temperature dependence of phosphorescence reported in [63].

The fit of the TPB response to 128 nm photons yielded the largest prompt fraction at 0.73. Calculations using the integral of the fitted curve show that 97% of the scintillation comes from the first 7 µs, meaning that argon experiments, which normally use integration windows of this size, lose a small amount of their light yield to this effect.

Lastly, there was an observed energy dependence of the AW on the energy, most notably for alpha scintillation. In other words, alphas that passed normally through the TPB deposited less energy than alphas that passed through at a steep angle, and if an AW is produced for each case, slight differences can be seen. We attribute this to the fact that as the alpha is slowed down by the TPB, it experiences different values of $\mathrm{d}E/\mathrm{d}x$ along its track, producing different initial concentrations of ionization. This is at odds with the model, which assumes a constant $C_T(0)$, and may explain some of the discrepancy in the fits of the alpha data. Rather than divide up the alpha spectrum, the AWs we present here are weighted sums over all energies, which correspond to weighted sums over all solid angles. This represents the average signal expected from a decay, which can eject its products in any direction.

7.5 Surface Background Suppression

Based on the results of Measurements C and D, we find that when comparing surface alpha decays to 128 nm argon scintillation photons, the former produce pulses with a larger fraction of light in the delayed component. This suggests that surface decays can be separated from events that take place in the bulk argon.

To quantify this rejection power, we compare the results of Measurement C to data published by DarkSide-50, a dark matter experiment with a liquid argon target

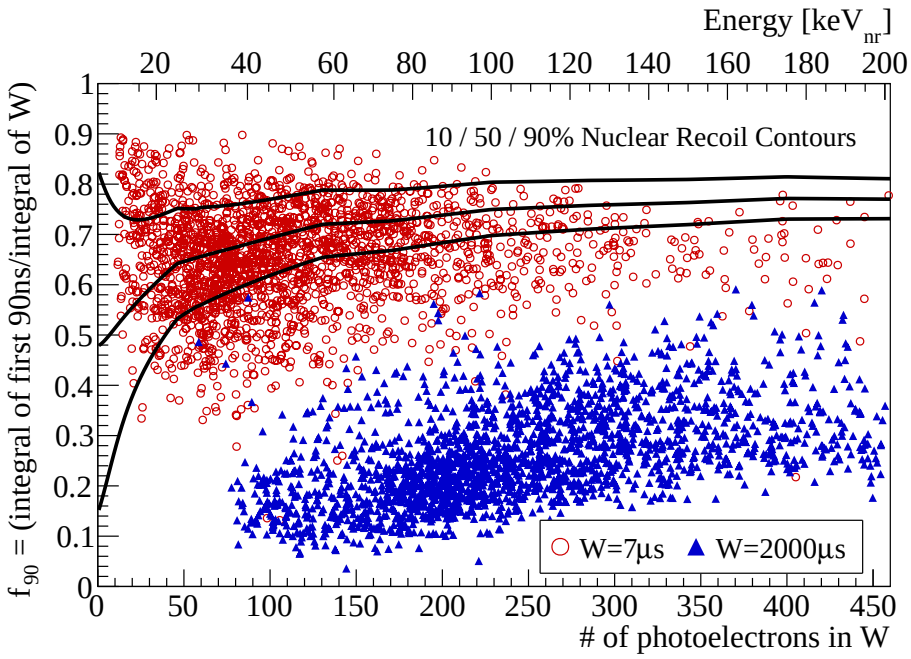

Figure 7.13: The effect of the integration window size W on the pulse shape parameter f_{90}. By using a larger window, more of the photoelectrons from the delayed component are included, and the events are moved away from the nuclear recoil band. Contours obtained from [28].

mass [28]. DarkSide-50 uses a parameter called f_{90}, defined as the integral of the first 90 ns of the pulse divided by the integral of the first 7 µs of the pulse, to separate nuclear recoil signals from the electron recoil backgrounds. Fig. 4 of the cited paper features a plot of f_{90} vs. the number in photoelectrons in the first 7 µs of the pulse. A line is drawn on the plot as the 90% nuclear recoil acceptance contour ("90% line"), which is used for the dark matter search. Therefore, the number of interest is the fraction of surface decays that will produce a signal that fall above this line.

To properly compare results across the two experiments, the pulse integrals from our experiment were multiplied by a factor of 7.9/6.23, which corrects for the difference in light yield between the two experiments. The zero-field light yield for DarkSide-50 was found in [15], and the light yield for our experiment was calibrated with the 60 keV gamma from an ^{241}AmBe source.

Due to the large, long-lived tail of the TPB scintillation, the region of f_{90} space that surface backgrounds occupy is heavily dependent on the chosen size of the integration window, which we will call W. A larger choice of W will result in a larger denominator in the f_{90} calculation, pushing the events downward in f_{90}, away from the nuclear recoils. A visualization of this can be seen in Fig. 7.13, where the same events have been plotted twice: once with $W = 7\,\mu s$ and once with $W = 2000\,\mu s$. With the shorter integration window, 63% of ∼2500 surface alpha decays produced a signal above the 90% line. With the larger integration window, none did.

Furthermore, we know that the nuclear recoils themselves will not experience the same shift in f_{90} because Measurement D showed that >97% of the argon scintillation light from the nuclear recoil that is shifted by the TPB will be detected within 7 µs. This means that with a large W, the average nuclear recoil will experience shift downward in f_{90} of about 3% (slightly more due to the delayed photons from the triplet argon scintillation).

An order-of-magnitude estimate of the surface background acceptance (fraction of surface decays that fall above the 90% line) for $W = 2\,ms$ can be obtained by fitting a Gaussian to each bin along the x-axis, thereby obtaining a probability of a surface event with a given energy to fall in the region of interest. Integrating over the entire range gives an acceptance of 10^{-6}.

For reasons such as trigger rate and pile-up signals, the use of millisecond-long acquisition windows may be impractical for some experiments. We have extended the acceptance estimation method to different choices of W to obtain the acceptance as a function of W, which can be found in Fig. 7.14. The error bars show the difference between the Gaussian estimation method and a direct counting of the number of events above the 90% line. At least one event in the ∼2500 event data set, possibly an accidental coincidence, remains above the line up until W=1000 µs. As mentioned previously, with W=2000 µs, no events were found above the line.

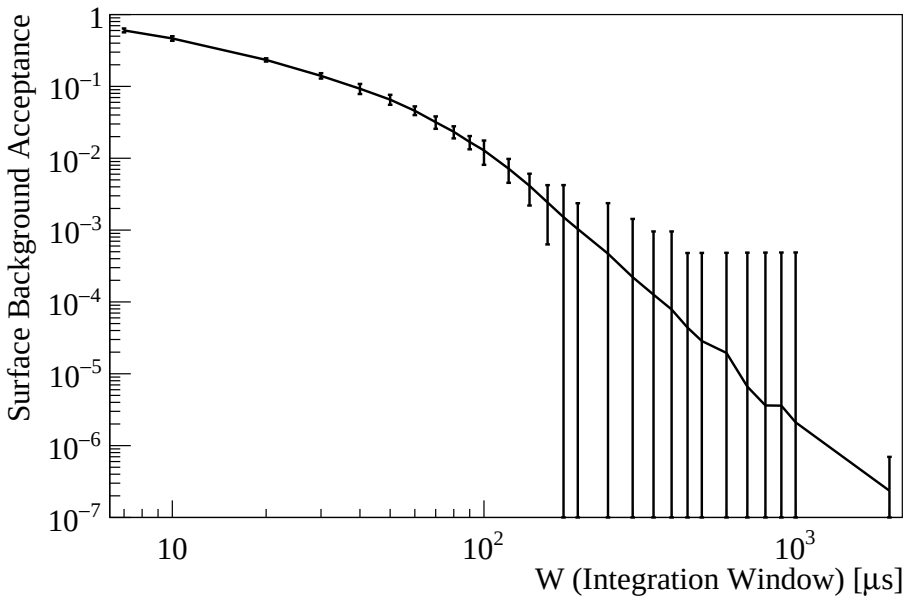

Figure 7.14: Surface background acceptance as a function of integration window size

The surface background suppression factor is the inverse of the surface background acceptance, reaching a value of up to 10^6 with the longest integration windows. This should be understood as the suppression factor for surface decay mode I(b), which is only one mode of surface background. However, each other mode that carries a risk of background must also have a similar or larger fraction of its light come from TPB, making this measurement an estimate of the suppression of surface backgrounds as a whole.

7.6 Conclusions

We have demonstrated the existence of a "delayed" component of TPB scintillation that has a lifetime for on the order milliseconds, and that the magnitude of this component depends strongly on the ionization density induced by the incident radiation. Scintillation pulses caused by alpha particles contain most of their light in the delayed component. This allows for pulse-shape discrimination to be used to re-

ject surface backgrounds. When compared to the dark matter search region used by DarkSide-50, a surface background suppression factor of 10^6 can be obtained when using millisecond-long integration windows.

7.7 Broader Application

This technique can be extended beyond LAr experiments by coating detector materials with TPB and vetoing signals with long scintillation tails.

While TPB may not be suitable for use in every experiment, the long-lived scintillation component does not appear to be unique to TPB. Although the detailed results are beyond the scope of this work, two other compounds were discovered to have delayed scintillation components like TPB.

The first compound was p-Terphenyl, another organic wavelength shifter, which suggests that the TPB tail is a property of aromatic scintillators in general. The second compound was MgF_2, an inorganic compound. MgF_2 may be more suitable for liquid xenon experiments, which tend to dissolve organic compounds like TPB and p-Terphenyl [65, 66]. MgF_2 is also transparent to the liquid xenon scintillation light. Further investigation into these compounds is ongoing.

Chapter 8

DarkSide-50

8.1 Overview of the Detector

DarkSide-50 is a dark matter experiment searching for Weakly Interacting Massive Particles (WIMPs). It has been collecting physics data since late 2013 at Laboratori Nazionali del Gran Sasso (LNGS). To detect WIMPs it uses a two-phase liquid argon time projection chamber (LAr TPC) with a target mass of roughly 50 kg, shown in Fig. 8.1.

8.1.1 The TPC

A diagram of the TPC is found in Fig. 8.1. The TPC is contained within a cylindrical stainless steel cryostat which maintains the liquid argon temperature. On the inside, an active volume of argon is formed out of a cylindrical Teflon reflector with a fused silica window on each end. The volume has a radius and height of approximately 20 cm and 40 cm, respectively. It is filled mostly with liquid argon, except for the top $\sim$1 cm of the volume which is maintained as an argon "gas pocket".

A series of electric fields are present in the TPC, created by voltages applied to thin layers of indium tin oxide (ITO) on the bottom (cathode) and top (anode)

windows, and to an etched metal grid sitting in the liquid just beneath the gas pocket. These electric fields are responsible for drifting free electrons to the top of the liquid (drift field) and extracting them into the gas pocket for detection (extraction field).

A Teflon reflector is used to redirect photons toward the windows. Both the Teflon and the windows are coated with TPB (Sec. 4.2) to absorb the 128 nm argon scintillation photons and re-emit them at longer wavelengths that can be reflected by the Teflon and transmitted through the windows.

Outside each window of the TPC is an array of 19 photomultiplier tubes (PMT). The PMTs detect the photons and send the signals to the data acquisition system (DAQ) to be recorded. Each PMT is calibrated with a laser to determine the average signal size from a single photoelectron (PE).

When ionizing radiation interacts with the LAr in the TPC, it both excites and ionizes the argon (see Fig. 8.1). The excited argon quickly returns to the ground state, and many of the ionized argon atoms recombine with an electron. The pulse of light given off during this process is called the primary scintillation, or S1.

Due to the drift field, some of the freed electrons are pulled away from the argon ions and escape the recombination process. They drift upward until they reach the gas pocket, where the extraction field pulls the electrons out of the liquid and through the gas. Electrons travelling through the gas excite argon atoms in their path, producing a pulse of secondary scintillation light, called S2. S1 and S2 are measured in terms of how many PE they contain.

The delay between the arrival of the S1 and S2 pulses depends strictly on the vertical (z) position of the event within the detector. This delay is called the drift time, and ranges from 0 for events at the top of the detector to 376 µs for events at the bottom of the detector.

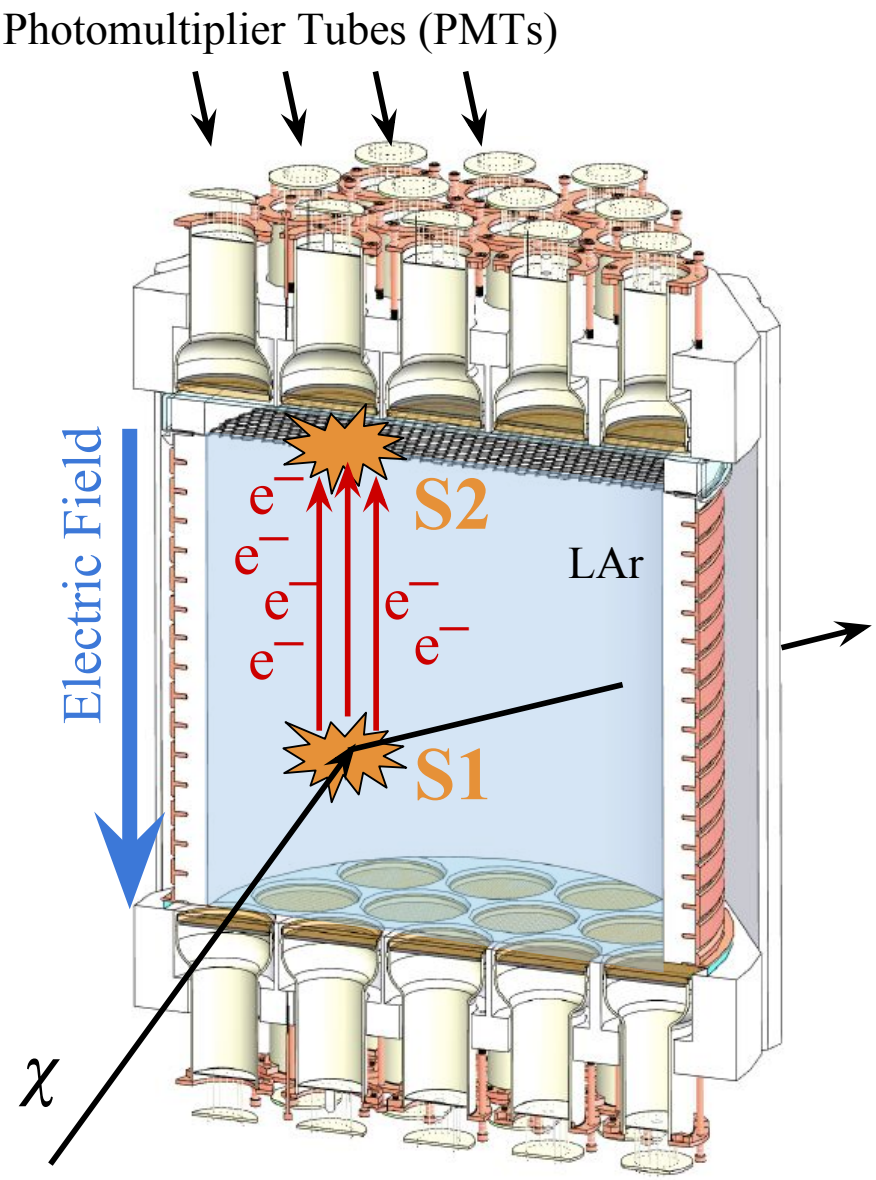

Figure 8.1: A cartoon of an interaction in the DarkSide-50 TPC.

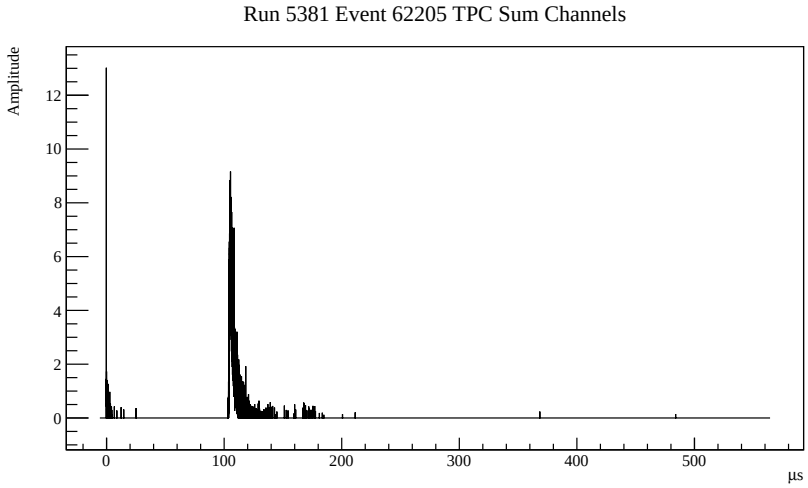

Figure 8.2: An event in DarkSide-50. The S1 and S2 pulses are visible at 0 µs and 100 µs, respectively.

Since the S2 is produced at the top of the TPC, the pattern of light on the upper array of PMTs can be used to measure the transverse (xy) position of the initial interaction.

When at least two PMTs see a pulse of light at the same time, the DAQ is triggered and 440 µs of consecutive data is recorded in order to capture both the S1 and S2 signals. This 440 µs snapshot is called an "event". An example of an event can be seen in Fig. 8.2.

8.1.2 Data Reconstruction

Processing of the raw event data is done with software called DarkArt, which performs the function of reconstructing the variables that are used in the analysis. Examples include the start time of each pulse, the size of S1 and S2, and the drift time.

One important parameter that DarkArt calculates is the f_{90} for each pulse, which is defined as the integral of the first 90 ns of the pulse (called the "prompt") divided by the integral of the first 7 µs of the pulse. It acts as a measurement of the shape of the pulse and can be used to identify the nature of the pulse. A pulse with an f_{90} of 1 means that it contains the entirety of its light in the first 90 ns. A pulse this fast

is likely caused by a flash of Cherenkov light in the fused silica or Teflon material. A pulse with an f_{90} of 0.6–0.7 indicates that most of the light is prompt, and based on the properties of argon scintillation discussed in Chapter 3, is likely an S1 from a nuclear recoil of an argon atom, as expected from a neutron or WIMP. An f_{90} of ~ 0.3 is expected for electron recoil S1 pulses from gammas or betas, and finally an f_{90} below 0.1 is a sign that the pulse is an S2, which has a long rise times and lasts for tens of microseconds.

8.1.3 Outer Detectors

In the case where a neutron interacts only once with the argon, it is indistinguishable from a nuclear recoil caused by a WIMP[1]. DarkSide-50 takes two measures to protect itself from neutrons: first, it uses materials that have had their radioactive content measured to ensure that few neutrons will be produced near the detector over its lifespan; second, it uses outer detectors to act as shielding from external neutrons and as a veto to neutrons coming out of the TPC.

A drawing of DarkSide-50's nested detectors can be seen in Fig. 8.3. From out to in, the detectors are the Water Cherenkov Detector (WCD, 11 m diameter), the Liquid Scintillator Veto (LSV, 4 m diameter), and the TPC. The WCD vetos signals induced by cosmogenic muons, and the LSV contains a boron-loaded scintillator cocktail that produces light when a neutron is thermalized or captured within it.

More details concerning the outer detectors can be found in [26, 67, 68].

[1] If a neutron or gamma ray interacts with the argon, it may scatter multiple times. If this happens, the multiple S1s will be simultaneous and indistinguishable, but the event will contain multiple S2s, one for each interaction's z-position.

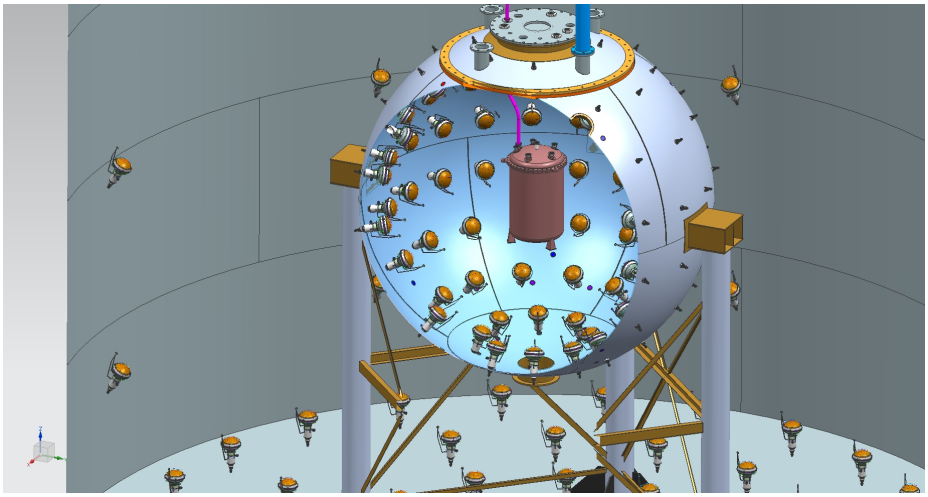

Figure 8.3: All the detectors that make up DarkSide-50. From out to in: The water Cherenkov detector, the liquid scintillator veto, the TPC.

8.2 Results

DarkSide-50 has published two sets of dark matter search data: [15] and [28]. The first consisted of a (1422±67) kg day exposure, and used argon obtained from atmospheric sources. The second consisted of a (2616±43) kg day exposure, and used argon obtained from an underground source, which has a lower level of the ^{39}Ar radioisotope. They are referred to as the 50- and 70-day dark matter search campaigns, respectively.

WIMP Search Region

The WIMP search region (also called the dark matter search region, or WIMP box) is an area of S1-f_{90} space. The WIMP search region for the 70-day campaign is shown in Fig. 8.4. The line along the bottom of the region is defined such that any events falling above it are 90% likely to be caused by a nuclear recoil with the LAr. The left edge of the region is set at a level such that the total number of events from the electron recoil band at $f_{90}\sim$ 0.3 that leak into the search region is less than 0.1 events.

Neither the 50- or 70-day campaign saw any events in the WIMP search region.

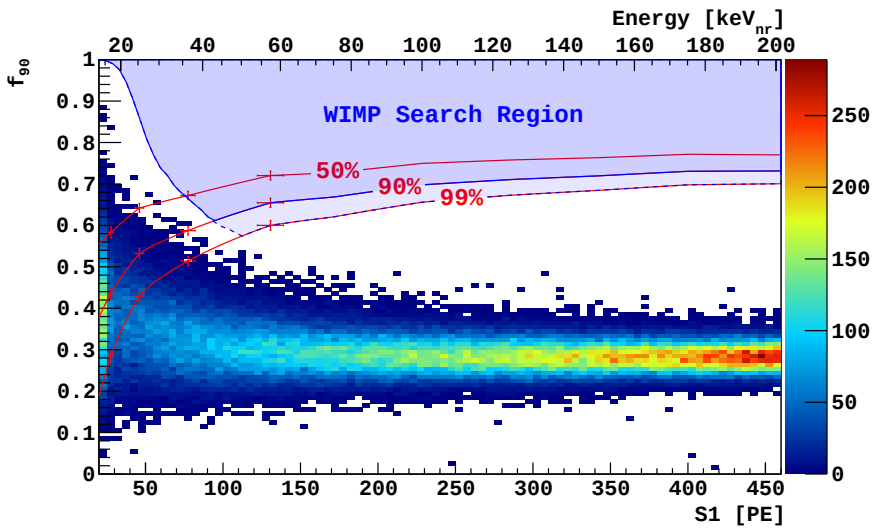

Figure 8.4: Results from the DarkSide-50 70-day dark matter search [28].

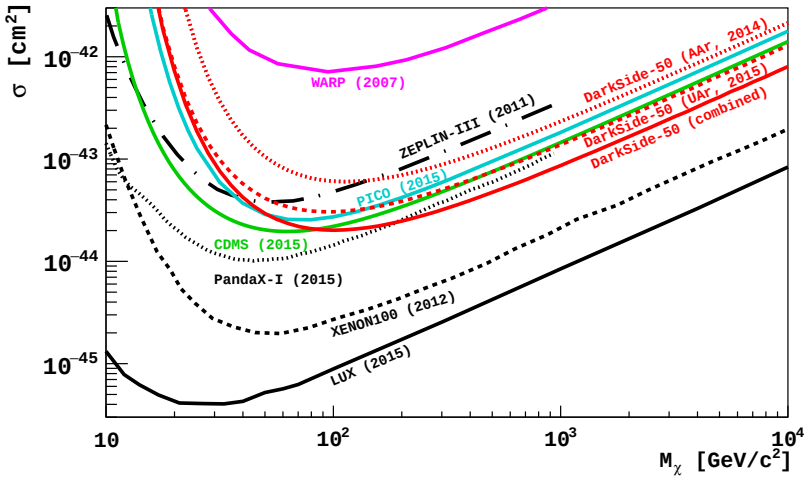

Figure 8.5: Dark matter sensitivity curves for the 50- and 70-day search campaigns, along with contemporary limits from other experiments [28].

Sensitivity

Given the lack of any signal or background in the WIMP search region, only an upper limit on the WIMP mass and cross-section could be set. The sensitivity curves for each campaign can be seen in Fig. 8.5, along with the sensitivity curves of contemporary results from other experiments.

8.2.1 Future

DarkSide-50 has continued to acquire data since the previous publications and has to date collected over 500 live days of additional data with underground argon. For the duration of the campaign, a blinding box has been applied to the S1-f_{90} space that covers the WIMP search region and some space beyond. The lack of knowledge of what lies within the box ensures that any analysis cuts developed to remove background events remain unbiased.

Currently, the expected background from various sources (neutrons, gammas, betas, Cherenkov, alphas, and surface backgrounds) has been estimated for a 500-day campaign. To combat the higher backgrounds associated with a greater exposure, several analysis cuts have been developed beyond those used in the 70-day analysis.

This chapter, which is focused on alphas and surface backgrounds in DarkSide-50, provides the background estimates from these sources for the 500-day campaign.

8.3 Alphas in DarkSide-50

8.3.1 Identifying Alphas

Alphas can be easily identified in DarkSide-50 data. We define any pulse with $f_{90} > 0.5$ and $f_{90} < 0.9$ as an "alpha-like" S1 signal. At high energy, the region of the f_{90}-S1 phase space is far removed from other classes of events, and allows for a clean look at the alpha spectrum. As seen in Fig. 8.6, the alpha events have a tail that extends down to low S1 values. These are degraded alphas and will be discussed in Sec. 8.7. For now, we will just consider the high energy alpha spectrum.

Alpha S1s are so large that the DarkSide-50 analog-to-digital converters (ADCs), which are tuned to low energy thresholds to look for WIMPS, can be saturated by the alpha scintillation light (see waveform in Fig. 8.7 (left)). To accurately measure

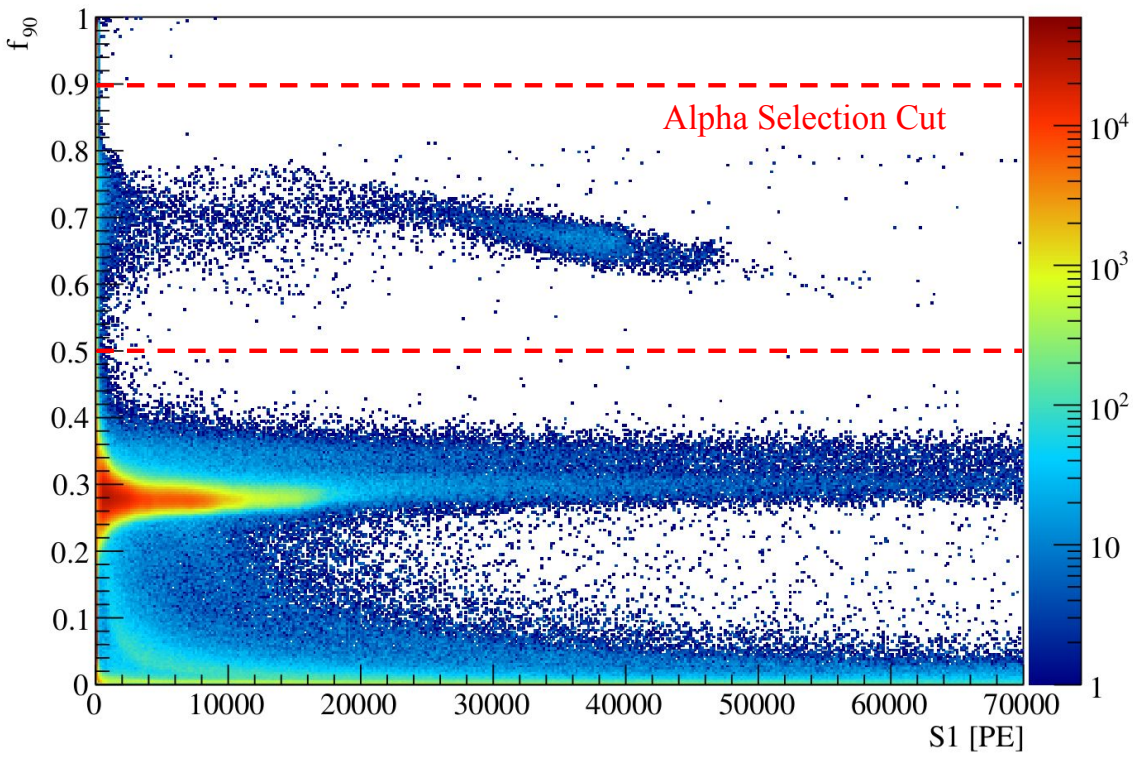

Figure 8.6: The events from the DarkSide-50 70-day campaign with no cuts. The S1 and f_{90} values have been corrected for ADC saturation effects. The band of alpha events can be seen at $f_{90}\sim$ 0.7, well separated from the electron recoil band. The slight downward slope toward higher S1 appears to be an artifact of the use of f_{90}. Alphas typically saturate the ADCs for over 100 ns. The use of longer pulse shape parameters, such as f_{200}, removes this slope.

the S1 of such signals, DarkSide-50 uses another set of low-gain ADCs that do not saturate. By measuring smaller signals passed through both sets of ADCs, a linear mapping can be made between the two. Then, when a event saturates on the high-gain ADCs, its S1 can be corrected based on how much it deviates from this linear mapping (see Fig. 8.7 (right)). This mapping was the work of collaborator Xin Xiang at Princeton University.

When checking to see if a pulse is alpha-like, the saturation-corrected values for S1 and f_{90} are always used. The formula for the f_{90} correction is:

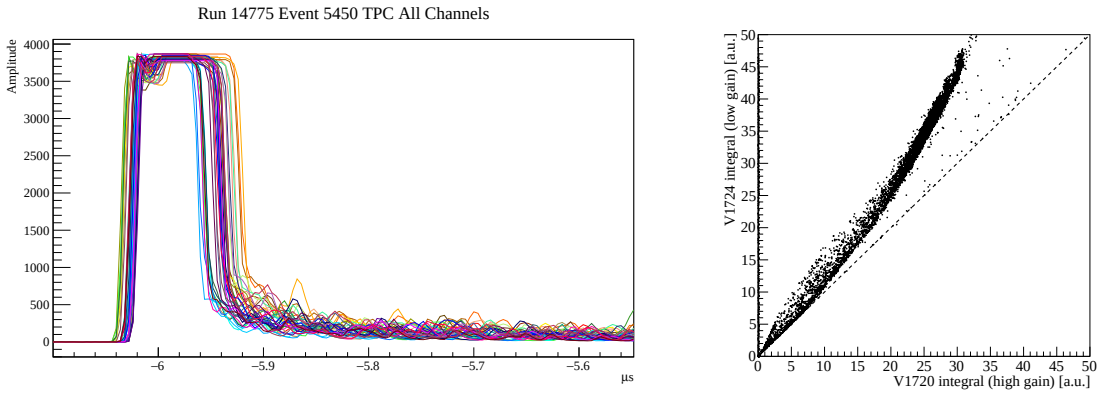

Figure 8.7: **Left**: A zoom-in of the prompt region of an alpha S1, showing the effect of saturation in the flattened peak at $-6\,\mu s$. Each colored line represents a different PMT channel, all of which are saturated by this event. **Right**: A comparison of pulse integrals between the high-gain (x-axis) and low-gain (y-axis) ADCs. The bend away from the diagonal for larger pulse integrals shows the saturation of the high-gain ADCs.

$$f'_{90} = (\mathrm{S1}' - (1 - f_{90})\mathrm{S1})/\mathrm{S1}'$$

where the symbol ($'$) refers to the saturation-corrected quantity.

8.3.2 Spectrum

The S1 spectrum of alphas in DarkSide-50 can be seen in Fig. 8.8. Two corrections have been made to the S1 values. The first is the ADC saturation correction. The second correction is to counteract an observed z-dependence of the light yield in the TPC. Normally, an event's z-position is determined using its drift time; however, some of the alpha S1 signals seen in DarkSide-50 lack an accompanying S2, and therefore have no definite drift time (see Sec. 8.7.1). So for all the DarkSide-50 alpha S1 studies described in this thesis, an alternate method of performing the z-correction was used. The method is based on the ratio of light received by the top and bottom PMTs, and is called the top-bottom asymmetry. The correction algorithm is explained in more detail in Sec. 8.5.

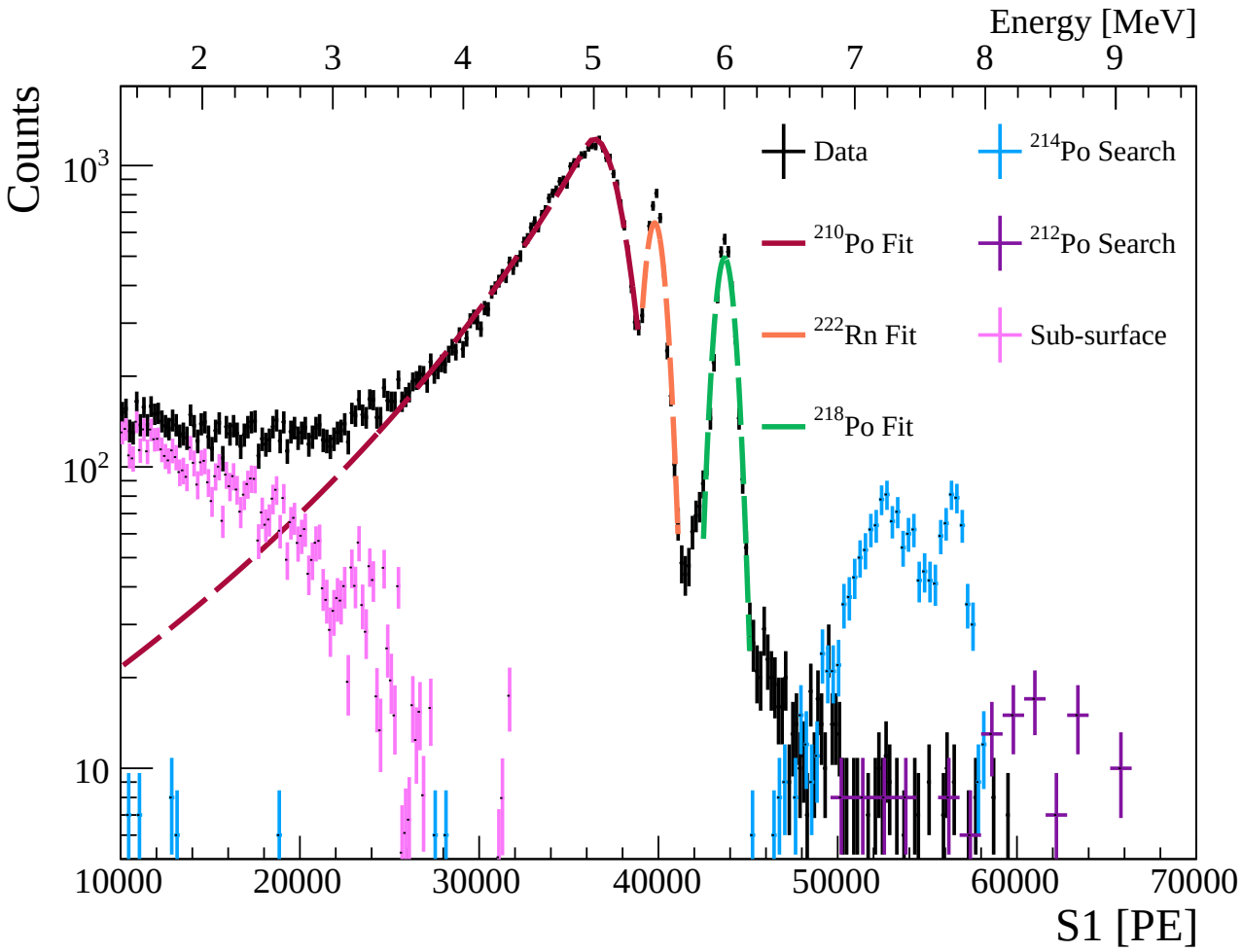

Figure 8.8: The alpha spectrum in DarkSide-50.

The black histogram is the data in which the first pulse in the waveform was alpha-like. Some alphas, such as ^{214}Po, are very short lived, and the data acquisition system triggers on the preceding ^{214}Bi decay, making the alpha S1 the second or later pulse in the event, depending on the placement of S2s. In order to find these events, the second, third, and fourth pulses (if they exist) of each event were scanned for alpha-like pulses (see Sec. 8.3.3), and these events are shown in the blue histogram. In the case of ^{212}Po, which shares such a near coincidence ($\tau_{1/2} = 300\,\text{ns}$) with ^{212}Bi that they are normally classified as a single pulse, a sub-pulse scan was performed on the S1 pulse to see if it contained an alpha (see Sec. 8.3.4), and these events are shown in the purple histogram.

The initial identification of the peaks in the spectrum comes from observing the timing of the events in the peaks labelled ^{222}Rn and ^{218}Po. The separation in time between an event in the ^{222}Rn peak and the following event in the ^{218}Po peak closely matches an exponential distribution with a half-life matching the 3 minute half-life of ^{218}Po. Once identified, the energy scale was calibrated based on a fit to the ^{218}Po peak, giving a light yield of 7.279 ± 0.002 (stat.) PE/keV at 200 V/cm drift field. The other peaks could then be verified by assuming a linear relationship between energy and S1. Note that for this calibration, the effect of the recoiling daughter nucleus in the argon is ignored. Measurements have shown that this signal is heavily quenched in argon, and would be responsible for less than 0.1% of the light produced during an alpha decay in the bulk [48].

Rather than a Gaussian, the ^{210}Po peak is fit with a crystal ball function, which models energy loss through a thin film. This is because its suspected origin is on the surface beneath the TPB, causing the alphas to lose a fraction of their energy dependent on their angle of ejection. The low energy tail shows significant deviation from this fit, pointing to degraded alphas coming from deeper in the material. The excess is shown in the pink histogram.

The alpha spectrum reveals many interesting aspects of the detector when one examines each alpha in greater detail. Understanding these alphas aids in both the risk assessment for background events in a dark matter search and the reduction of such risk in future experiments.

As mentioned in Sec. 5, it is the lower chain alpha decays that are more commonly seen inside a detector. Each of these decays will now be discussed in detail with references back to the alpha spectrum.

8.3.3 Lower ^{238}U Chain

^{222}Rn and ^{218}Po

^{222}Rn undergoes alpha decay with a 3.8 day half-life. At sea level, the atmosphere contains an average concentration of 6×10^{-20}mol/mol of ^{222}Rn gas [69], which means that in every cubic meter of air, there is an average 20 atoms of ^{222}Rn decaying every second. Due to radon's large mass, and its production in the Earth's crust, the underground labs that dark matter detectors inhabit can experience much higher concentrations. It can find its way into DarkSide-50 through the argon recirculation system (a radon trap helps to reduce this effect) or through emanation of radon from detector materials.

^{218}Po is the daughter of ^{222}Rn and undergoes alpha decay with a 3 minute half-life. Its relatively short half-life often allows it to be identified with its parent ^{222}Rn decay. This delayed coincidence has several practical benefits which are discussed in Sec. 8.6.

^{222}Rn and ^{218}Po are two of the most dominant alpha emitters in DarkSide-50. They can be seen in the alpha spectrum (Fig. 8.8) as the peaks fit with the orange and green Gaussians, respectively. The ^{218}Po peak is the most isolated of all the alpha peaks and is used to determine the alpha light yield.

^{214}Po

^{214}Po is the next alpha in the ^{238}U decay chain. It has a half-life of only 164 µs, and emits one of the most energetic naturally occurring alphas, with an energy of 7.7 MeV. Its short half-life means that it has a delayed coincidence with the preceding beta decay from ^{214}Bi. Sometimes termed "BiPo", the coincidence can be used to measure ultra-low radon radioactivity levels [70].

DarkSide-50, when it records an event, saves an approximately 440 µs-long snapshot, or "window", following the trigger. This means that when it triggers on the

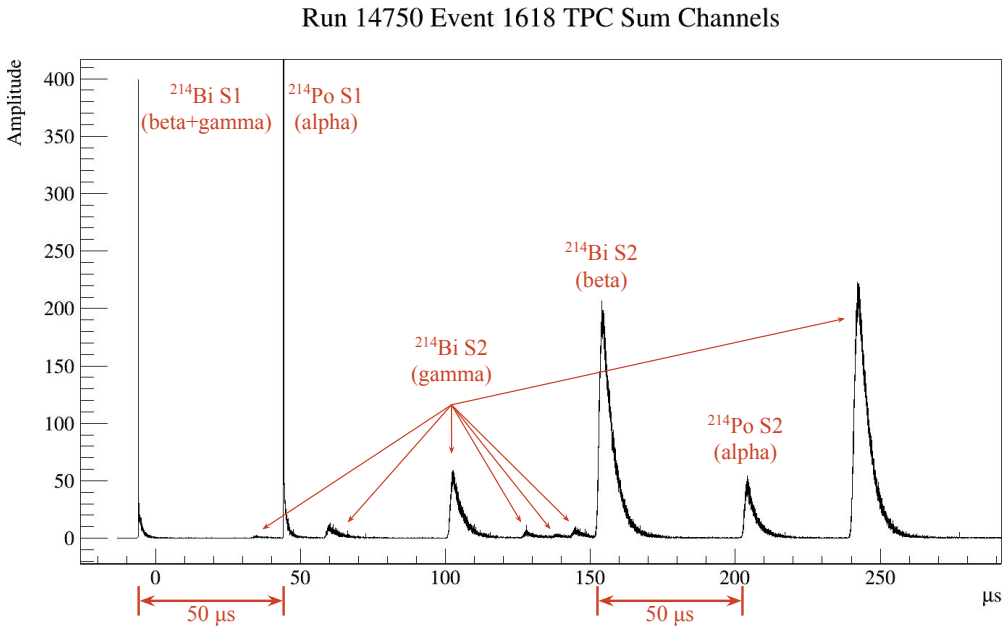

Figure 8.9: A BiPo event with many S2s coming from coincident ^{214}Bi gammas.

S1 of the ^{214}Bi decay, the alpha S1 signal from the ^{214}Po decay can often be seen later in the window. Each S1 will have a corresponding S2, but depending on how long it takes to decay and how near to the bottom of the TPC the event is, the S2 from the ^{214}Po may fall outside the window and be lost. Additionally, when the ^{214}Bi decays, it has an 81% chance of simultaneously emitting one or more gamma rays. These gammas could interact with the argon themselves, producing an S1 that is concurrent with the ^{214}Bi S1, and an S2 that will appear offset from the ^{214}Bi S2 if the gamma deposits energy at a different z-position. Each gamma can, of course, interact multiple times as well. This causes many of the BiPo events to be "messy", with many gamma S2s (see Fig. 8.9).

The fact that ^{214}Po comes later in the chain after the ^{222}Rn and ^{218}Po alpha decays means that there is an elevated chance of finding it on the cathode surface, because one of the previous isotopes could have been ionized after it decayed and then been drifted to the cathode by the electric field. Cathode surface ^{214}Po BiPos can escape

detection from a dedicated BiPo search if the products from one or both of the decays get absorbed by the surface.

Looking back at the alpha spectrum (Fig. 8.8), the ^{214}Po S1 pulses tagged by the BiPo search can be seen in the blue histogram between 6 and 7 MeV. The odd, double-peak shape is suspected to be the result of an artifact in the S1 correction algorithm, which is based on the asymmetry of light collected by the top and bottom arrays of PMTs. This correction is known to have problems on the cathode surface due to the large bias that the asymmetry correction has toward events directly above the reflective surface that fills the gaps between the PMTs. Evidence for this stems from the fact that the events in the narrower 57000 PE peak, which corresponds to the "correct" alpha energy of 7.7 MeV, primarily occur in the bulk argon, as judged by their drift time. The events in the broader peak at 52000 PE are found to be almost entirely from the cathode. Each peak's coincidences match the expected lifetime of ^{214}Po, ruling out the possibility that we are seeing two distinct alphas.

Ultimately, the BiPo coincidence does not offer much useful information for liquid argon detectors at the scale of DarkSide-50. One potential use could be to count the level of radon contamination in the liquid, but this would involve determining the BiPo tagging efficiency, which, for reasons mentioned above, can be a significant challenge. A more accurate measurement of the radon contamination can be obtained with less effort by simply measuring the size of the ^{222}Rn peak in the alpha spectrum. A second use could be for a position reconstruction algorithm, to verify that both the ^{214}Bi and ^{214}Po decays are reconstructed in the same place. However, the limited number of "clean" BiPos with two isolated S1s and two isolated S2s makes this difficult, and again a better sample can be easily obtained by looking at short-lived ^{222}Rn–^{218}Po or ^{220}Rn–^{216}Po coincidences.

^{210}Po

The last alpha in the ^{238}U chain is ^{210}Po, with a half-life of 138 days. Its parent isotope, ^{210}Pb, is a beta-emitter with a half-life of 22 years.

The long-lived nature of ^{210}Pb has several consequences. First, it tells us that any exposure to ^{222}Rn will result in ^{210}Pb and ^{210}Po contamination that will outlast the length of the experiment. Any experiment that is concerned about a background from these isotopes must find a way to deal with them, unlike other lower chain isotopes which quickly decay away.

Second, it tells us that the lower ^{238}U chain does not necessarily have to be in secular equilibrium; the ^{210}Po alpha rate may not match the ^{222}Rn rate. This is because ^{210}Pb could be introduced in large quantities to the detector surface during assembly through lead-contaminated water or dust, and it would take decades for the ^{210}Pb rate to equilibrate with a constant supply of ^{222}Rn in the detector. Evidence of this disequilibrium can be seen by eye in the DarkSide-50 alpha spectrum, and in the rates reported in Tables 8.1 and 8.4.

Third, it tells us that ^{210}Pb (and therefore ^{210}Po) will almost always be found on surfaces rather than in the bulk argon, since for it to be found in the bulk it must avoid adhering to a surface for many years.

The shape of the ^{210}Po peak in the alpha spectrum confirms this last point. Rather than being Gaussian, it has a tail that extends out toward lower energies. It has been fit with a crystal ball function, which consists of a Gaussian function with a power-law tail on one side. It is used to model behavior of a particle degraded by a thin film, such as the layer of TPB coating the surface.

The mean of the Gaussian part of the crystal ball function is at 4.91 MeV, below the expected energy of 5.3 MeV. This can be explained by the fact that if the ^{210}Po is on the detector surface, *underneath* the TPB, then at the bare minimum the 5.3 MeV alpha from ^{210}Po can expect to lose a 160 keV by travelling normally through the

$\sim 200\,\mu g/cm^2$ layer of TPB on the wall. The varying TPB thickness throughout the detector could explain the broadness of the peak.

Towards the lower end of the spectrum the crystal ball fit deviates from the data, with the excess shown by the pink histogram. Simulations that place all of the ^{210}Po on the surface under the TPB fail to explain this excess, and it is therefore attributed to sub-surface ^{210}Po that is even further degraded.

For further details concerning ^{210}Po as a surface background see Sec. 8.7: *Surface Backgrounds in DarkSide-50*.

The rate of ^{210}Po decays as a function of time can be used to determine the ^{210}Pb level. If the rate of decay has a half-life of 138 days, it indicates that it is not being replenished by ^{210}Pb, and the detector must have been directly exposed to a ^{210}Po source. If the decay rate follows a much longer half-life of 22 years, it indicates that the ^{210}Po is in secular equilibrium with ^{210}Pb.

The rate of ^{210}Po events in DarkSide-50 over an 800-day span can be found in Fig. 8.10. To avoid contamination from the other alpha peaks, the rate is based on events with S1$\in$[10000,37000] PE. The histogram is fit with both the ^{210}Po decay curve and the ^{210}Pb decay curve. The rate is consistent with the ^{210}Pb curve.

In conclusion, ^{210}Pb contamination is ultimately responsible for the ^{210}Po rate in DarkSide-50. Future detectors should therefore seek to specifically reduce exposure to ^{210}Pb sources in order to cut down on ^{210}Po backgrounds.

8.3.4 Lower ^{232}Th Chain

^{220}Rn and ^{218}Po

The lower ^{232}Th chain begins with ^{220}Rn which undergoes alpha decay with a half-life of 56 s, followed by ^{216}Po with a half-life of just 0.15 s, emitting another alpha.

The short lifetime of ^{220}Rn relative to ^{222}Rn means that there is less time for it to diffuse into the argon, making the overall rate much lower.

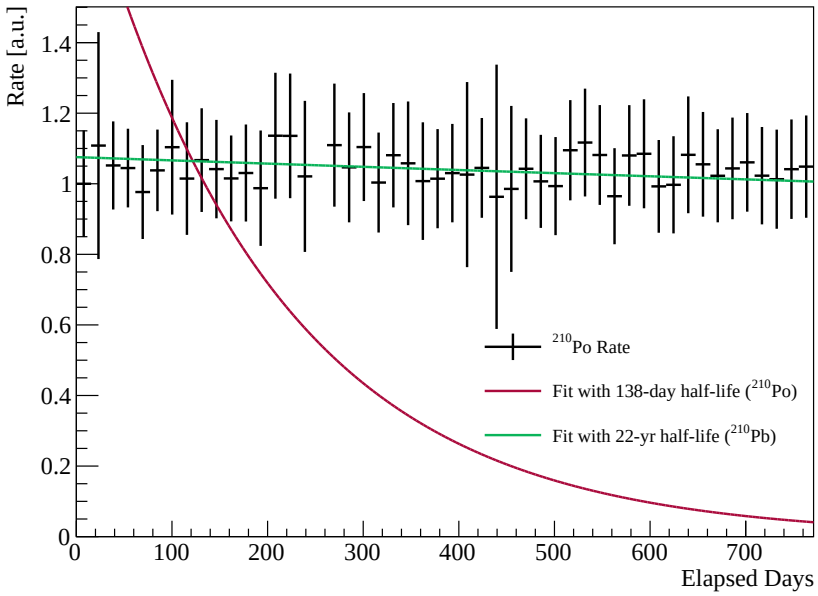

Figure 8.10: ^{210}Po rate over time in DarkSide-50. The value of the first bin has been set to 1.

A delayed coincidence search (see Sec. 8.3.8) was performed to search for the presence of these alphas.

The results of the coincidence search can be seen in Fig. 8.11. The energy scale is set using the light yield previously determined by ^{218}Po. The energies for the ^{220}Rn and ^{216}Po peaks are consistent with the expected values of 6.3 and 6.8 MeV. The time between the alphas follows an exponential with half-life of (0.161 ± 0.03) s, in agreement with ^{216}Po's the expected half-life.

The rate of ^{220}Rn is DarkSide-50 based on the coincidence search is 0.037 nBq/kg. The estimated tagging efficiency for the coincidence search is greater than 90%. This is based on the expected fraction of coincidences that will fall out of the time window used for the coincidence search (see Sec. 8.3.8).

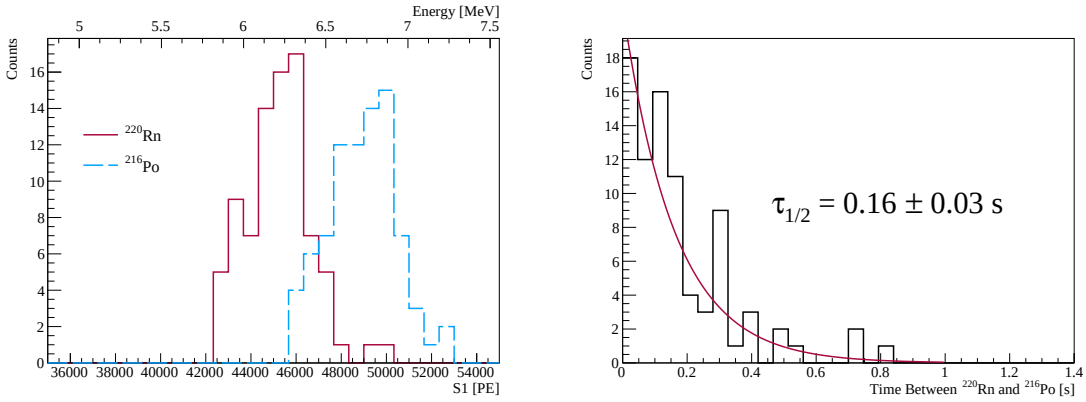

Figure 8.11: Results of a ^{220}Rn–^{216}Po coincidence search in DarkSide-50.

^{212}Bi

^{212}Bi has a half-life of 61 minutes and undergoes alpha decay 35% of the time. The alpha has an energy of 6.1 MeV, which is close to the dominant ^{218}Po peak, and therefore cannot be seen in the alpha spectrum. The parent isotope, ^{212}Pb, has a 10.6 hour half-life, and the daughter, ^{208}Tl, has a 3 minute half-life, and both of these undergo beta decay. This makes a coincidence search for the ^{212}Bi alpha more difficult, as DarkSide-50 has an electron recoil background rate on the order of 1 Hz. One approach that could be explored is to tag the characteristically high energy (2.6 MeV) gamma from the ^{208}Tl decay.

Rather than performing a search for this alpha and estimating the tagging efficiency, an upper limit on the event rate can be set using the fact that ^{212}Bi is in secular equilibrium with ^{220}Rn.

^{212}Po

The other 65% of the time, ^{212}Bi undergoes beta decay into ^{212}Po, which is the shortest lived and highest energy alpha emitter in the natural decay chains.

With a half-life of just 0.3 µs, ^{212}Po's alpha pulse is too near to the ^{212}Bi beta pulse to be separated by the data reconstruction software's pulse-finding algorithm. To identify these signals in the data, a search was done by scanning through the S1

pulse in small increments, looking for a large second derivative indicating the presence of a secondary pulse.

The condition:

$$\frac{\#\text{ of PE between } 0.1\,\mu\text{s and } 1.6\,\mu\text{s}}{\#\text{ of PE in first } 10\,\mu\text{s}} > 0.5$$

separates the prompt ^{212}Po alpha sub-pulses from S2 sub-pulses from unresolved S1+S2 pulses from events very near the top of the TPC. See Fig. 8.12 (left) for an example of an event found with this search.

After the ^{212}Po has been identified within the pulse, the S1 can be reconstructed by subtracting out the ^{212}Bi beta signal using the formula:

$$\mathrm{S1}_{^{212}\mathrm{Po}} = \mathrm{S1} - \frac{\#\text{ of PE in first } 90\,\text{ns}}{\text{mean electron recoil } f_{90}}$$

and then corrected for saturation and z-position. The result of the search is shown in the purple histogram in the alpha spectrum (Fig. 8.8). The reconstructed energy peak is in good agreement with the expected value of 8.8 MeV.

The timing results of this search can be found in Fig. 8.12 (right). The measured value for the ^{212}Po half-life is (482 ± 132) ns.

8.3.5 Lower ^{235}U Chain

^{219}Rn begins the lower ^{235}U chain and has a half-life of only 4 s. This does not give it much time to find its way into the active LAr volume.

The daughter isotope, ^{215}Po, decays with a half-life of 1.8 ms, and another delayed coincidence search was performed to find these decays. Several were found with decay times less than 5 ms, but both the number of matches and the energies of the alphas were consistent with them being very short-lived ^{216}Po decays.

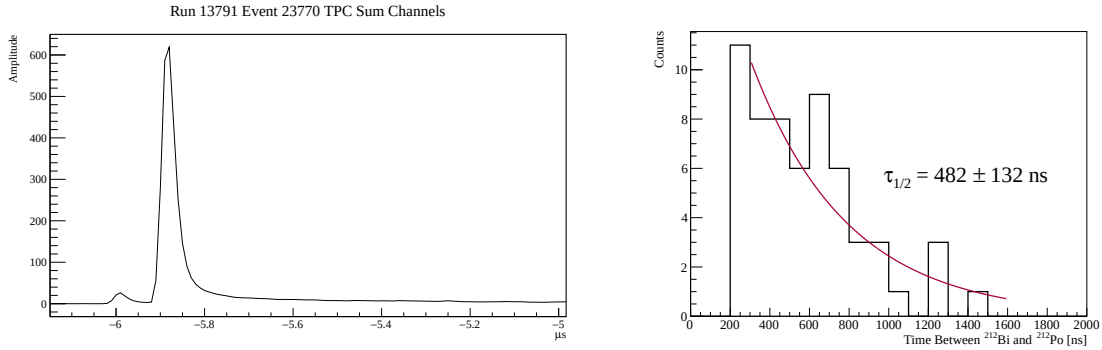

Figure 8.12: **Left:** A ^{212}Bi–^{212}Po coincidence waveform zoomed to the start of S1. The pulses are only 100 ns apart. These pulses are too close together to be distinguished by the pulse-finding algorithm used in DarkSide-50. **Right:** A histogram of the time separation between the two peaks shows that the measured half-life agrees with the expected value of 300 ns.

Chain	Isotope	Energy [MeV]	Measured [MeV]	$\sigma/\sqrt{n}$ [MeV]	Rate[a] [µBq kg^{-1}]
^{238}U	^{222}Rn	5.49	5.47	0.001	2.12 ± 0.04
	^{218}Po	6.00	6.00[b]	0.001	1.55 ± 0.03
	^{214}Po	7.69	7.73	0.005	>0.72, <1.55
	^{210}Po	5.30	4.91	0.001	[c]
^{232}Th	^{220}Rn	6.29	6.20	0.023	0.037 ± 0.004
	^{216}Po	6.78	6.71	0.025	0.037 ± 0.004
	^{212}Bi[d]	6.05	—	—	$< 0.35\times$ ^{220}Rn rate
	^{212}Po	8.78	8.34	0.045	>0.06, <0.65$\times$ ^{220}Rn rate

[a] Errors are statistical.
[b] Reference point.
[c] See Sec. 8.7.
[d] Peak could not be identified via spectrum or coincidence search.

Table 8.1: Alpha rates in DarkSide-50. The values for the ^{238}U chain are obtained via spectral fitting, while the rates for the ^{232}Th chain are obtained via coincidence search. No alphas were found belonging to the ^{235}U chain.

8.3.6 Rates

The measured rates of each alpha in DarkSide-50 can be found in Table 8.1.

8.3.7 Background Estimate

Alphas in the bulk liquid do not pose a background for the DarkSide-50 dark matter search due to their extremely high energy. However, alphas that are evenly mixed throughout the volume may occasionally decay very close to the wall and deposit only a fraction of their energy in the LAr before running into the surface.

A rough evaluation of this risk can be performed as follows: Suppose there is a hollow cylinder of infinite length and radius R. At a random location within the cylinder, a particle is emitted at a random trajectory and travels a distance d in a straight line. Assuming $d \ll R$, the probability of that particle hitting a wall of the cylinder can be shown to be approximately $d/2R$. For the case of DarkSide-50, an alpha only needs to deposit $\sim$1% of its energy to fall above the dark matter region of interest. Given that a 5.5 MeV alpha has a range of about 50 µm in LAr, d can be approximated as 0.5 µm. Plugging in the radius of the detector ($R \sim 18$cm) sets the probability of an alpha particle in the bulk depositing a small enough amount of energy to fall in the dark matter region of interest at 1.4×10^{-6}.

The dominant source of alphas in the bulk LAr comes from ^{222}Rn and ^{218}Po. The ^{222}Rn rate in DarkSide-50 is 2.12 µBq kg^{-1}, making the overall WIMP background rate from ^{222}Rn just 0.0045 events/year. This increases to 0.0077 events/year when the ^{218}Po rate is included. This is well below DarkSide-50's background budget of 0.1 events/year, but it's worth noting that as a detector scales up in volume V, the surface area scales as $V^{2/3}$. If the radon concentration remains the same as in DarkSide-50, then a detector with a size of 20 tonnes can expect to see one background event from bulk alphas every 2.3 years (assuming it isn't rejected by other analysis cuts, such as fiducial cuts or the TPB cut described in Sec. 7.2).

8.3.8 Delayed Coincidence Algorithm

This appendix describes the algorithm used to perform the delayed coincidence searches in Sec. 8.3.3 and 8.3.4.

A loop over all events was performed. When an event passed the data quality cuts (event contains data from all the channels and the waveform baseline was found by the reconstruction algorithm), the alpha S1 cuts ($f_{90} > 0.5$ and $f_{90} < 0.9$), and the alpha S2 cuts ($f_{90} < 0.1$ and $\log(\mathrm{S2/S1}) > -1$), its S1 was compared to the defined range for the first alpha in the coincidence and its event number and time stamp were stored if there was a match.

For example, after an alpha in the ^{222}Rn S1 range was found, its event number and time stamp were stored in an object called `previous_Rn222_event`, overwriting any ^{222}Rn event that may have been saved before.

When an alpha was found that matched the S1 range for the second alpha in the coincidence, such as ^{218}Po, the time difference between that event and the previous ^{222}Rn event were checked. If this time difference fell within a predefined range, the coincidence was stored permanently and the `previous_Rn222_event` object was cleared.

The S1 ranges for each alpha were defined relatively loosely in order to catch alphas that may have had a degraded energy from passing through a material.

The allowed time delay differs for each alpha coincidence to avoid mischaracterizing one coincidence as another. For example, the ^{220}Rn–^{216}Po ($\lambda_{1/2} = 0.15\,\mathrm{s}$) coincidence search used a time delay range of 0.01-2 s to avoid contamination from the longer lived ^{222}Rn–^{218}Po ($\lambda_{1/2} = 3.1\,\mathrm{min}$) and shorter lived ^{219}Rn–^{215}Po ($\lambda_{1/2} = 1.8\,\mathrm{ms}$) coincidences.

The parameters used for each coincidence search can be found in Table 8.2.

Coincidence	Isotope	Min S1 [PE]	Max S1 [PE]	Min Delay [s]	Max Delay [s]
^{222}Rn–^{218}Po ($\lambda_{1/2} = 186\,\mathrm{s}$)	^{222}Rn	41000	41000	2	1800
	^{218}Po	45000	45000		
^{220}Rn–^{216}Po ($\lambda_{1/2} = 0.15\,\mathrm{s}$)	^{220}Rn	51000	51000	0.01	2
	^{216}Po	53500	53500		
^{219}Rn–^{215}Po ($\lambda_{1/2} = 0.0018\,\mathrm{s}$)	^{219}Rn	70000	70000	0	0.01
	^{215}Po	70000	70000		

Table 8.2: Parameters for the alpha coincidence searches.

8.4 Alpha S2s

When an alpha deposits its full energy in DarkSide-50 it produces a large S1 signal consisting of tens of thousands of photoelectrons. The resulting S2 has a similar size, which varies depending on the strength of the drift field. However, alpha events frequently have other small, S2-like pulses in their waveforms. This section studies their nature and their impact on alpha analysis in DarkSide-50.

A selection of alpha events occurring in the bulk LAr was obtained using a delayed coincidence search of ^{222}Rn and ^{218}Po. Then, rather than identifying a single S2 in the waveform, every pulse following S1 was labelled as S2 and the value log(S2/S1) was computed as a measure of its size. The drift time of each pulse relative to S1 was also recorded.

The plot of the S2 size vs. drift time can be found in Fig. 8.13. The remainder of this section will involve explaining the different features that can be seen in this figure.

The first feature is the band of S2 pulses at log(S2/S1)=0 that extents from 0 drift time to the maximum drift time of 376 µs. As a reminder, the S1 signals for ^{222}Rn and ^{218}Po are 40,000-45,000 PE, so these S2s are roughly the same size. These are the so-called "real" S2s that correspond to the argon ionization electrons freed by

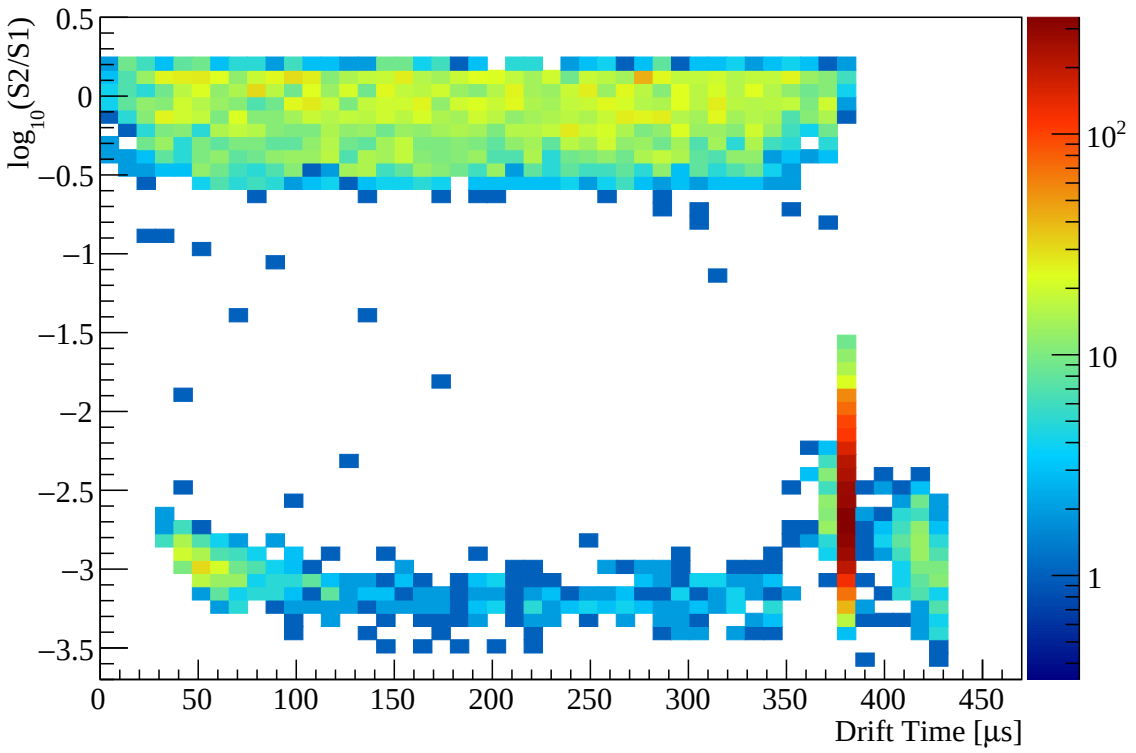

Figure 8.13: A study of all pulses following S1 in ^{222}Rn and ^{218}Po alpha events. Many events contain small S2-like pulses with log(S2/S1)= −3 in addition to their "real" S2 with log(S2/S1)= 0.

the alpha interaction. This can be confirmed by selecting alpha events that had only a single pulse following S1 and realizing that all the S2 signals fall within this band.

The second feature is the hot-spot at the maximum drift time and log(S2/S1) = −2.5. These pulses correspond to a phenomenon called the "S1-echo", and they occur when a UV photon from S1 hits the cathode surface and frees an electron. That electron will drift upward and produce a small S2 pulse consisting of 25-30 PE. Since it drifts all the way from the cathode, it will always occur exactly 376 µs after S1. With alpha S1s being characteristically large bursts of UV, it is not uncommon to free more than one cathode electron, which add together to produce S1-echos in excess 100 PE.

The third feature is the group of S2 pulses with drift times beyond 376 µs. These are from cathode electrons that were freed by the blast of UV from the "real" S2, and can be considered "S2-echos". Like S1-echos, they always occur 376 after the S2 pulse. Given that the entire data acquisition window is 440 µs long, S2-echos will only be seen for events with drift times between 0 µs and $(440 - 376)$ µs.

The last and most interesting feature of Fig. 8.13 is the band of events at $\log(\mathrm{S2/S1}) = -3$ that extends from 25 µs to 376 µs.

Initial attempts to explain these pulses fail. While their size is the same order of magnitude as the cathode photoionization S2s, they do not follow 376 µs after a source of UV. Random, spontaneous electron emission from the cathode could explain the timing and size of the pulses, but could not explain why they are correlated with alpha events or why the data acquisition system is not constantly triggering on spontaneous cathode emissions. Another possibility is that the S1 UV photons free an electron at some point on the Teflon wall, which then produces an S2 with variable drift time. This solution is disfavored for two reasons: one, the PMT that sees the most light from these pulses would always be one of the PMTs on the outer ring of the upper array, but this is far from being the case; and two, the drift electrons would likely not make it to the top of the TPC, but rather get absorbed and lost to the wall as they drift along its surface (see Sec. 8.7.1).

The solution comes from a closer look at the individual waveforms. It turns out that there are two the types of pulses within this band.

The first type is depicted in Fig. 8.14. In this case, the pulse-finding algorithm has misidentified a collection of single photoelectrons in the tail of S1 as a separate pulse. This long tail can be seen after every large pulse in DarkSide-50 as a direct result of the UV-generated long-lived component of TPB seen in Sec. 7.2. While the fraction of light emitted in the tail is small, the alpha S1s themselves are so large that this tail contains hundreds of photoelectrons, and if several of them cluster together

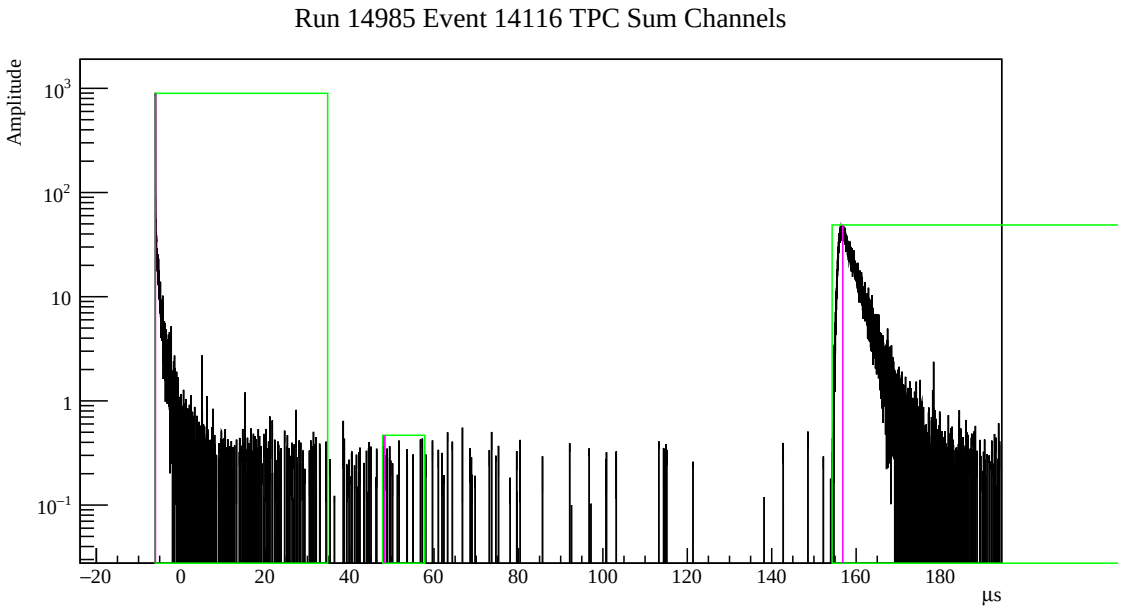

Figure 8.14: An alpha event where the pulse-finding algorithm has identified a segment of the long-lived TPB tail as a separate pulse.

they can be misidentified as a pulse. The likelihood of this occurring drops off with time as the tail becomes sparser, explaining the greater number of pulses in Fig. 8.13 in the 30-70 µs region.

The second type is depicted in Fig. 8.15 and appears to be a genuine S2 pulse with an average size of 30 PE, which is the expected S2 size from a single drift electron freed via photoionization. The pulse is too small for the xy-reconstruction algorithm to identify the transverse position of the pulse, but a rough estimate can be obtained by looking at the PMT pattern.

A 3D view of the DarkSide-50 PMTs can found in Fig. 8.16. Each PMT has been color-coded according to how much light it received during the photoionization pulse seen in Fig. 8.15, with the red PMTs receiving the most light and the blue PMTs receiving the least. The fact that the maximum channel is not one of the PMTs on the outer ring means that it is not a result of photoionization of the wall material. The middling xy and drift time place its point of origin directly in the center of the detector.

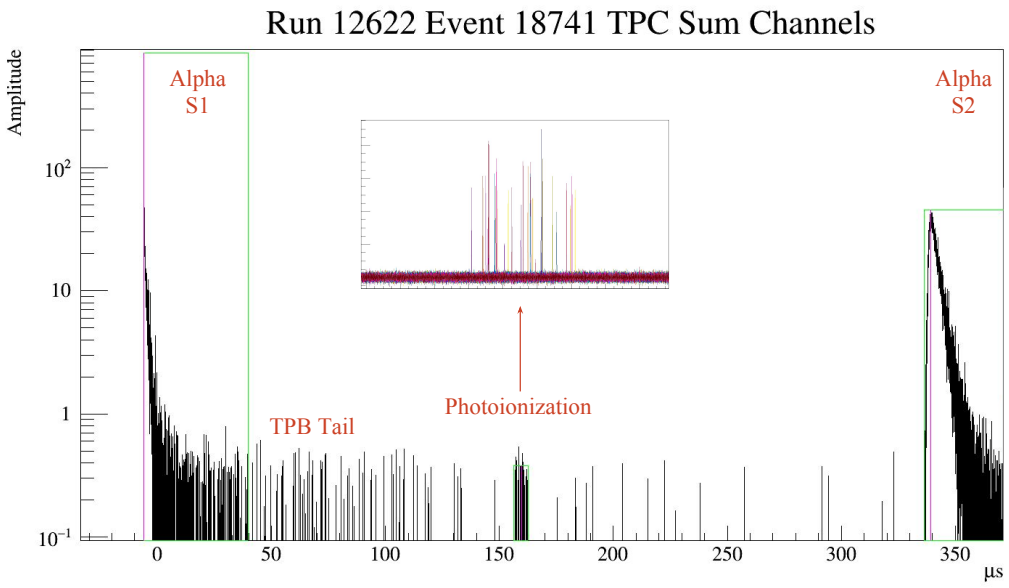

Figure 8.15: An alpha event with a photoionization signal at 160 µs. **Inset**: A zoomed in view of the photoionization signal, with different PMT channels shown in different colors.

Since the small pulse arrives *before* the alpha's S2, it means that it cannot be an electron from S2 that was "delayed" by a temporary capture on an impurity, as this would place the pulse after the alpha S2. Furthermore, the maximum channel of these pulses do not correlate with the maximum channel of the alpha S2s.

The evidence leads to the conclusion that this pulse comes from the photoionization of a single electron within the bulk argon itself. This would require UV photons from S1 to travel upward in the TPC and ionize an atom at a different z position so that the small, single-electron S2 arrives at the gas pocket at an earlier time than the thousands of electrons from the alpha S2.

The precise element undergoing photoionization is unclear. Each 128 nm scintillation photon carries an energy of 9.69 eV. The lowest electron binding energy of liquid argon is estimated in [71] to be 13.84 eV. The reference also estimates energy bands for excited states of argon around 9.63 eV and 9.80 eV, but mentions they might be lower than 9.5 eV. If there is an overlap between these energy bands and the 9.69 eV

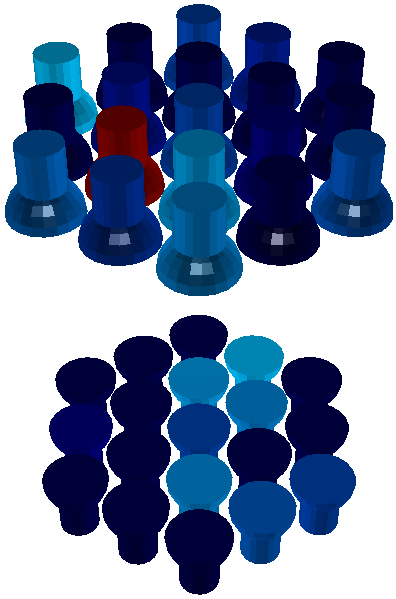

Figure 8.16: The PMT pattern from the small pulse in Fig. 8.15. The red PMT received the most light, indicating that it originated away from the side walls. Evidence points to this drift election coming from an atom in the bulk.

photon energy, it could open the possibility of argon photoionization through interaction with multiple photons, but measured values of the attenuation length of argon to its own scintillation light being on the order of a meter make this unlikely [72].

The existence of electronegative impurities in the LAr could provide the necessary ionization sources. Oxygen has an electron affinity of 1.46 eV, and could capture a drift electron from a previous event, which could be stripped off by the UV photon from the alpha S1 at a later time. To reduce these impurities, DarkSide-50 uses a SAES Monotorr PS4-MT50-R-2 getter to reduce O_2 to sub-ppb levels [15]. During the data-taking campaign used in this study there was a period of five days where the getter was shut off. The overall rate of these photoionization pulses was not found to increase during this period.

The last sources of ionization to consider are organic impurities within the LAr. If a TPB molecule on the interior detector surface breaks off and mixes with the argon, it could be ionized by a single 9.69 eV photon [73].

8.4.1 Analysis Cuts

In the standard DarkSide-50 analysis codes, a pulse is required to be bigger than 100 PE to be classified as S2. However, this analysis of alpha S2s has revealed that a large S1 can ionize enough electrons from the cathode surface to produce a pulse that exceeds this value. An updated version of the S2 size cut should be used to correctly identify S2s from large S1s:

```
bool S2_size_cut = (pulse_integral>100 &&
   log10(pulse_integral/S1)>-1);
```

For events with S1 up to 1000 PE, including all events in the WIMP search region, this cut remains unchanged from the standard cut. For S1s above 1000 PE the log(S2/S1) cut at -1 becomes the stricter term. The justification for setting it at this level can be seen in Fig. 8.13.

8.5 Alpha Light Yield

The contents of Sec. 8.5 were published in JINST [74].

The S1 light yield (hereafter referred to as simply light yield) for an interaction is defined as $LY = S1/Q$, where Q is the energy deposited in the argon during the interaction.

For beta particles, the presence of an electric field reduces the light yield [24]. This is typically explained as a result of the field pulling away electrons from the positive argon ions, resulting in less recombination and thus less primary scintillation. DarkSide-50 reports a beta light yield of 7.9 PE/keV for 0 V/cm drift field and 7.0 PE/keV for 200 V/cm drift field [15].

However, this relationship does not hold true for all types of ionizing particles. The light yield of liquid argon as a function of drift field has been measured for many

different forms of radiation, including neutrons [24], fission fragments [75], alpha particles [75, 76], and helium ions [76]. Alphas and helium ions were found to behave differently from the rest; the light yield increased as the drift field increased, until it reached a peak when the drift field was on the order of 1 kV/cm, after which the light yield began to decrease.

The purpose of this study is to report similar findings of the light yield behavior for alpha induced scintillation in DarkSide-50. A sample of alpha decays is obtained through the detection of naturally occurring radon daughters present in the liquid. Despite its low level of radon contamination (μBq/kg), DarkSide-50 has collected enough statistics to resolve the peaks in the ^{222}Rn decay chain spectrum.

For the dark matter search, DarkSide-50 operates with a drift field of 200 V/cm. However, a substantial amount of data has been collected with drift fields in a range from 0 to 200 V/cm for calibration purposes, and these data sets provide us with a means of comparing the alpha light yield at different field strengths.

A correction was applied to S1 that depends on the vertical (z) position of each alpha event within the TPC to account for a z-dependence of the light collection efficiency within the detector. The z-position of an event is typically measured using drift time (the time between S1 and S2), but in this case, where a comparison is being made to data taken with no field, drift time could not be used. A parameter called top-bottom asymmetry (TBA) was used instead. It is defined as:

$$\text{TBA} = \frac{\text{S1 from top PMTs - S1 from bottom PMTs}}{\text{S1 from all PMTs}}$$

A scatter plot of TBA and drift time in a 200 V/cm drift field can be seen in Figure 8.17. The feature at high drift time is a result of the geometry of the detector; events that are at the maximum drift time (the bottom surface of the TPC) have a TBA that is heavily biased depending on whether the event occurs above a PMT or above the PTFE reflector separating the PMTs. Events occurring directly above the

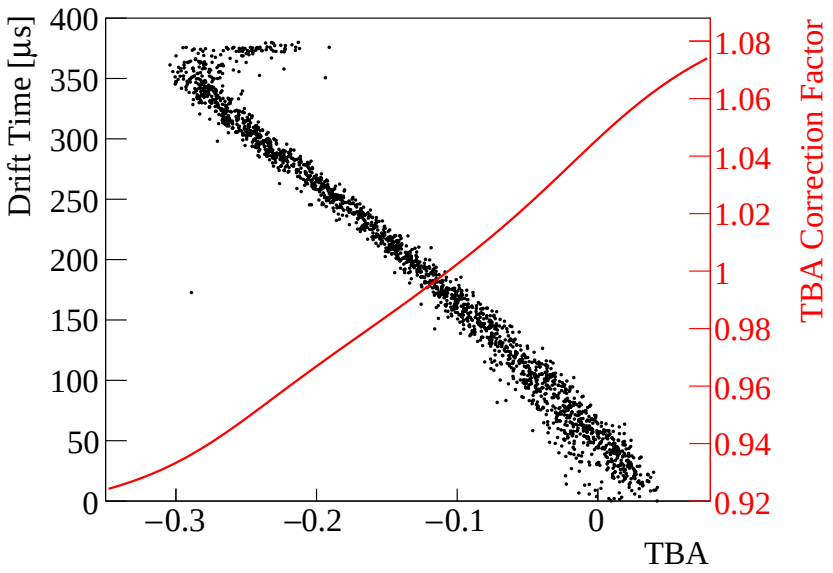

Figure 8.17: **Scatter plot**: Drift time vs. top-bottom asymmetry (TBA) for Po-218 events in a 200 V/cm drift field. The correlation allows TBA to be used as a measure of an event's z-position to make a correction to S1. See the text for an explanation of the feature at high drift time. **Line**: The magnitude of the multiplicative S1 correction factor for an event with a given TBA.

reflector have more light reflecting into the top PMT array, biasing the TBA upward. There is no equivalent feature at low drift time because the liquid is separated from the upper surface of the TPC by a layer of argon gas. This effect introduces a small systematic error into the TBA correction.

The TBA distribution is not symmetric about 0 due to partial internal reflection from the liquid-gas interface at the top of the TPC.

The S1 correction factor for a given TBA is derived from a calibration using the endpoint energy of the ^{39}Ar spectrum, and can be seen in Figure 8.17.

The same TBA correction is applied to all data, independent of an event's S1 or drift field. We eliminate the systematic error from the TBA correction in the final result by presenting the light yield at each drift field relative to the 0 V/cm light yield.

The alpha spectrum after the TBA correction is shown in Figure 8.18. The three peaks identifiable in the final spectrum are labelled based on their relative energies,

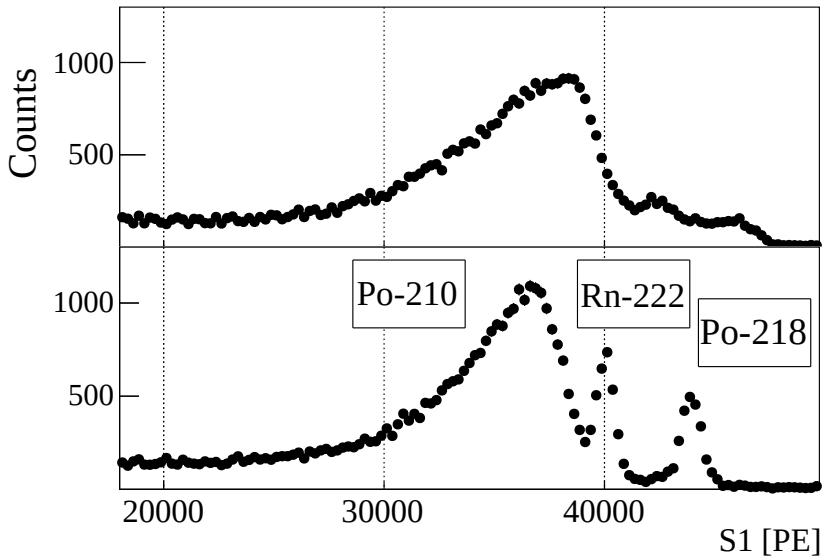

Figure 8.18: The alpha energy spectrum taken with a 200 V/cm drift field. **Top:** The spectrum after incorporating low-gain digitizer data to reconstruct the saturated pulse. **Bottom:** The top spectrum after correcting for the event's z-position within the detector, as determined by the top-bottom asymmetry.

from left to right, as ^{210}Po, ^{222}Rn, and ^{218}Po. More information about the spectrum and the peak identification can be found in Sec. 8.3.2.

The light yield at each drift field is calculated with a fit to the ^{218}Po peak. No conclusions were drawn from the larger ^{210}Po peak because the ^{210}Po alphas are coming from decays on the surfaces, and the electric field along the surfaces is not as well understood as in the bulk. The ^{222}Rn peak was not used due to leakage from the broad ^{210}Po peak.

The alpha spectra for drift fields of 0, 50, 100, 150, and 200 V/cm can be found in Figure 8.19. The histograms are defined with a bin width of 250 PE. The ^{218}Po peak is fit with a Gaussian+linear function over the domain (42000 PE, 46000 PE). To assist in the fit of the intermediate drift fields with lower statistics, an assumption was made that the peak width remains constant over the relatively small increase in mean. Then, a binned log likelihood fitting method was used across all the histograms

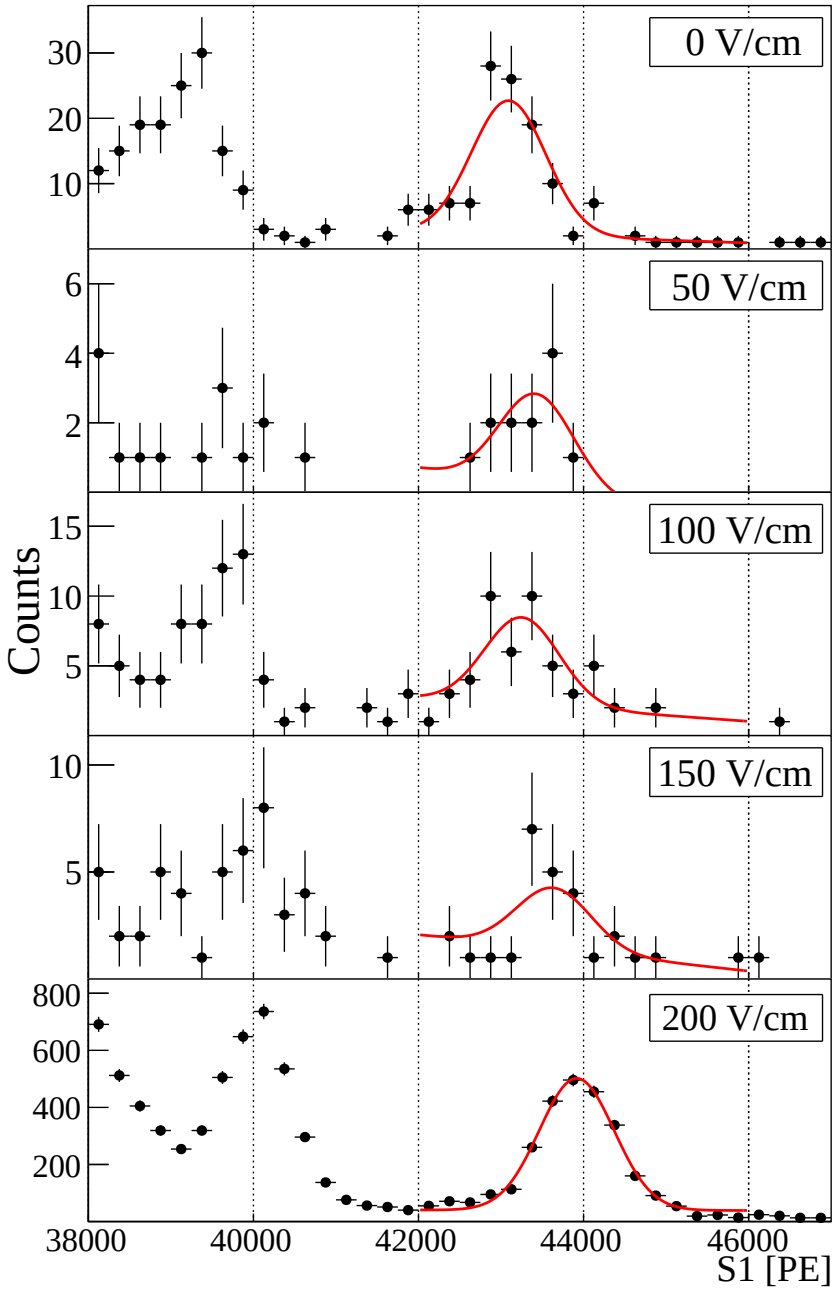

Figure 8.19: The alpha energy spectrum at different drift fields. The ^{218}Po peak, fit here with a Gaussian+linear function, noticeably increases in energy as the strength of the drift field increases. A coherent shift in the Rn-222 peak is visible on the left, although no attempt was made to fit this region.

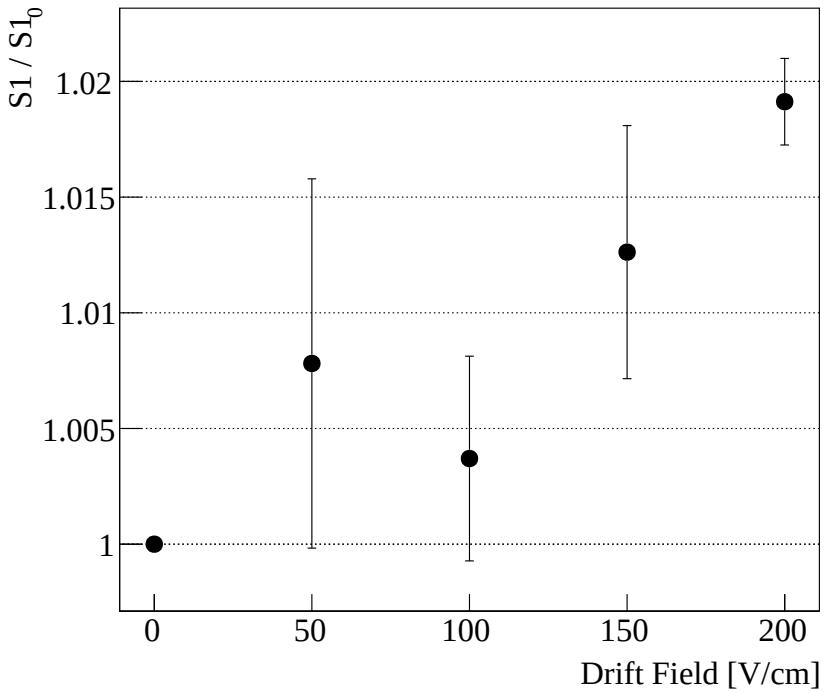

Figure 8.20: ^{218}Po alpha (6.0 MeV) S1 light yield at various drift field strengths relative to 0 V/cm. Statistical errors only.

simultaneously, with the peak width and the linear slope constrained to be the same while the mean was allowed to vary.

The results show that alpha light yield in DarkSide-50 increases as the drift field increases from 0 V/cm to 200 V/cm. The light yield of ^{218}Po alphas at 200 V/cm is 1.019 ± 0.002 times the light yield at 0 V/cm. This ratio for each drift field is plotted in Figure 8.20. The errors are statistical only, with the 0 V/cm point equal to 1 by definition.

The systematic errors from the choice of binning and fitting region were studied and found to be much smaller than the statistical errors ($\pm 3 \times 10^{-4}$).

In the previously mentioned study by Hitachi et al. [76], a similar effect was observed with ^{210}Po alphas (5.3 MeV). Although their study measures the dependence over a larger range (up to 6 kV/cm), their first data point is not until 540 V/cm (with S1/S1$_0$ = 1.03). Their following points at higher electric field strengths show a decreasing light yield. Our study, in addition to confirming the phenomenon for

^{218}Po alphas, provides data for the valuable region at low field strengths where the light yield is still increasing.

The cause of the increasing alpha light yield is not understood. As a possible explanation, Hitachi et al. suggest that the electric field may help drift the electrons out of the dense ionization tracks characteristic of alphas and helium ions, and allow some of the recombination to occur in regions of lower ionization density where non-radiative quenching processes have a reduced effect.

8.6 Alpha Decay Ion Fraction and Mobility

If the overall ^{222}Rn rate in a detector is low enough, the signal from the ^{222}Rn decay can be accurately matched to that of its corresponding ^{218}Po decay ($\tau_{1/2} = 3.1\,\mathrm{min}$). As reported in Table 8.1, the ^{222}Rn rate is only $2.12\,\mu\mathrm{Bq\,kg^{-1}}$, or $100\,\mu\mathrm{Bq}$ in the detector as a whole, which allowed for an effective coincidence search to be performed. The details of the search algorithm can be found in Sec. 8.3.8. This section discusses several properties that the ^{222}Rn–^{218}Po coincidence can be used to measure.

The ^{222}Rn–^{218}Po coincidence has an application for data analysis and reconstruction. Event pairs in which the ^{218}Po decayed quickly can provide an experiment with a means of measuring the precision of a position reconstruction algorithm, as the pair of events should reconstruct at the same place. This was done for DarkSide-50 in [77].

Some other measurements that can be made with the ^{222}Rn–^{218}Po coincidences, which are perhaps more interesting from a physics standpoint, are the heavy ion drift velocity and alpha decay ion fraction in LAr. This is possible because when the ^{222}Rn decays, there is some chance that the ^{218}Po daughter becomes ionized and begins to drift slowly along the electric field in the TPC. These measurements have been performed in xenon [78][79], but to date the measurements are lacking for argon.

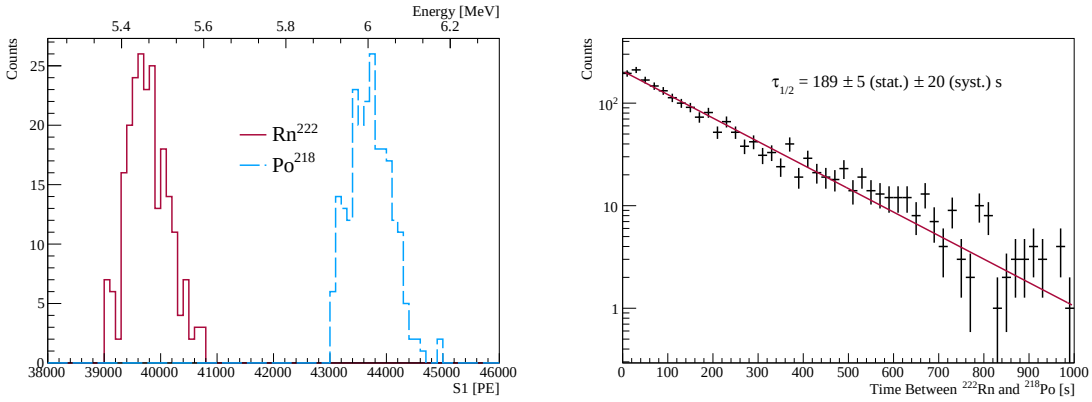

Figure 8.21: Results of a ^{222}Rn–^{218}Po coincidence search in DarkSide-50

The desire to measure the ion drift velocity with a finite volume adds an additional layer of complexity to the coincidence search algorithm. A fraction of the ionized ^{218}Po will drift all the way to the bottom and be stopped by the cathode surface before they have a chance to decay. Once they decay the will appear to have an artificially reduced drift velocity. To eliminate this bias, any coincidence that had the ^{218}Po decay occur in the bottom 5 mm of the TPC was discarded.

The results of the coincidence search in DarkSide-50 can be seen in Fig. 8.21. The S1 values of the identified ^{222}Rn and ^{218}Po alphas can be seen in the left figure, with the energy axis coming from the alpha spectrum as described in Sec. 8.3.2. The elapsed time between each pair of events is plotted in the right figure, and is in good agreement with the expected value of the ^{218}Po half-life.[2]

Position reconstruction of the coincidences reveals more information about these events. The z-position of each event is determined by that event's drift time, and is converted into a length by comparing it to the maximum drift time in the detector. The liquid level surface has been defined as $z = 0$, and the bottom surface rests at $z = -34.7\,\text{cm}$. The xy-position is determined using the PMT patterns by an algorithm developed by Jason Brodsky [80].

[2]For this histogram, only the coincidences with a z-separation of less than 1 cm were used in order to select neutral ^{218}Po, because the cathode surface creates a bias against seeing long-lived drifting ^{218}Po ions.

In DarkSide-50, events near the walls of the detector have reduced xy reconstruction accuracy, so an $r = 15\,\text{cm}$ fiducial cut was applied to the data, removing the outermost 3 cm.

The result of the position reconstruction can be seen in Fig. 8.22 (a). Each coincidence is represented by an arrow, with the base and head indicating the reconstructed locations of the ^{222}Rn and ^{218}Po decays, respectively. Each arrow is colored on a gradient based on its vertical drift velocity, measured as Δz divided by the time between the two events. Faster drift times are colored yellow while those with little to no vertical drift velocity are colored red. This is made more evident in Fig. 8.22 (b) and (c) which show the side and top views of (a). By eye, one can see that the fraction of neutral and ionized ^{218}Po atoms are of similar magnitudes. Concerning the transverse movement of the ^{218}Po it can be seen in (b), and even more so in (c), that the ionized ^{218}Po that drifts toward the cathode experiences very little transverse movement in comparison to the neutral atoms. Another feature that is visible in (b) is an unexplained region from $-15\,\text{cm} < z < -10\,\text{cm}$ that experiences reduced transverse movement. A sum of the angular velocity of the events showed no evidence of any net angular drift direction.

A more quantitative analysis of the above can be found in Fig. 8.23. This is a scatter plot of ^{218}Po decay time versus the drift distance in z. The vertical band of events corresponds to neutral events that were not significantly moved by the drift field. An additional band of events can be seen along a diagonal, which corresponds to positively ionized ^{218}Po drifting downward toward the cathode. The lack of any other bands of events with faster or slower drift speeds suggests that these are singly positively ionized ^{218}Po atoms. This is supported by observations of alpha decays taken in a vacuum, in which nearly all daughter nuclei were neutral or singly charged [81].

To measure the ion drift velocity, a section of the scatter plot was cut out (green dashed lines forming angles of $\pi/2$ and $\pi/4$) and events falling between them were

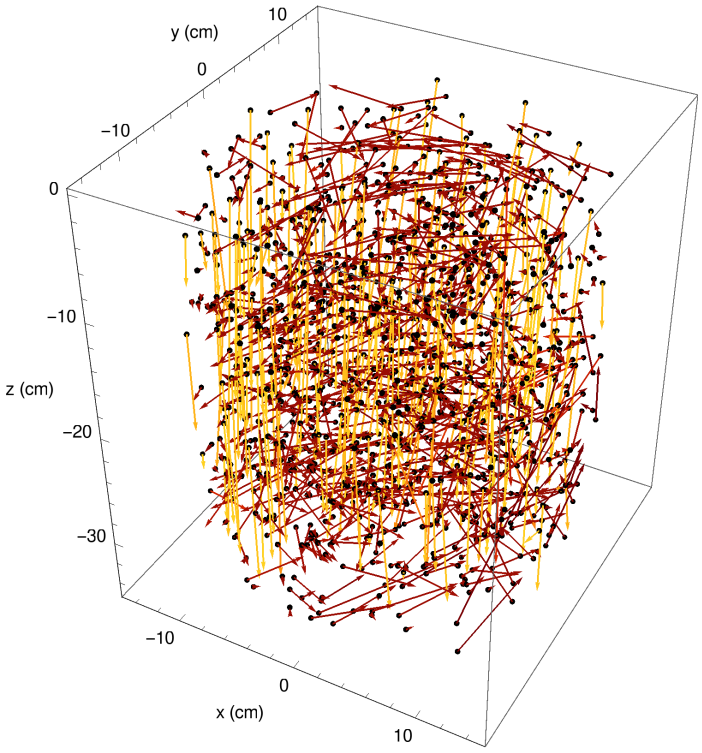

(a) 3D view.

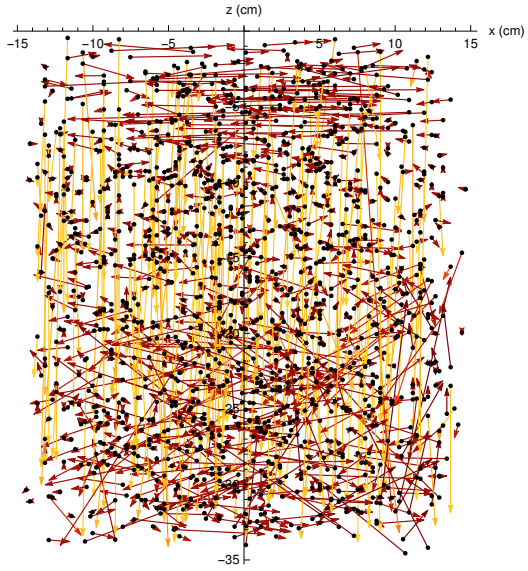

(b) Side view.

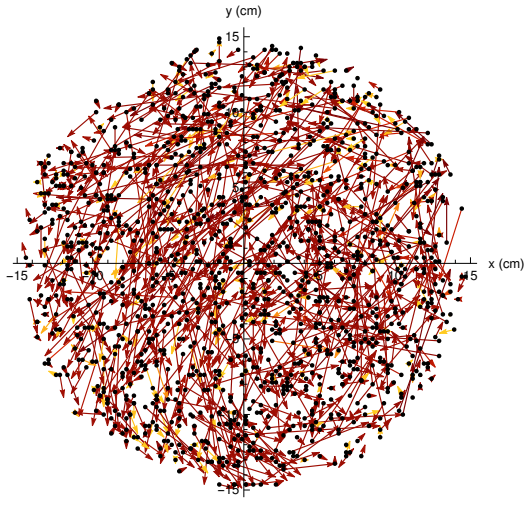

(c) Top view.

Figure 8.22: Position reconstruction of ^{222}Rn–^{218}Po coincidences in DarkSide-50. The path color represents the drift velocity of the ^{218}Po with dark red indicating little to no vertical movement and bright yellow indication a high drift velocity.

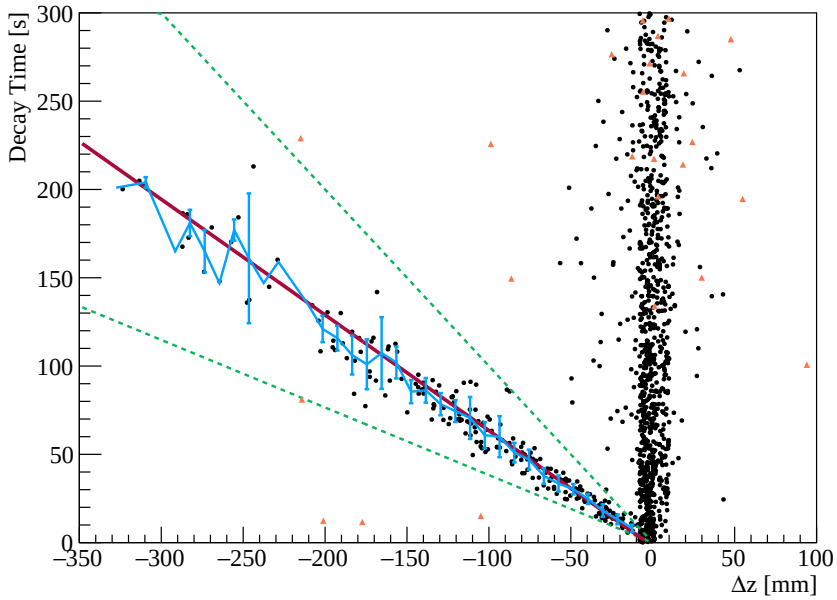

Figure 8.23: A scatter plot of decay time vs. vertical separation for ^{222}Rn–^{218}Po coincidences. The vertical band corresponds to neutrally charged decay products while the diagonal band corresponds to positively charged ^{218}Po that begins drifting toward the cathode before decaying. The blue graph shows the mean and standard deviation of each bin for the points between the green dashed lines, and the solid red line is a linear fit to this graph. The orange triangular points show coincidences that have a large separation in xy (> 12 cm), some of which may be accidental coincidences. The effect of these events on the final results was found to be negligible.

binned in Δz (blue graph) and fit with a linear function (red line). The result is a drift velocity of -1.53 $\pm$ 0.02 (stat.) $\pm$ 0.05 (syst.) mm/s for ^{218}Po ions in liquid argon. Dividing by the 200 V/cm drift field gives an ion mobility of 7.64×10^{-8} m^2 V^{-1} cm^{-1}.

Before the fraction of ionized ^{218}Po could be determined, first the bias caused by cathode surface ^{218}Po needed to be removed, as this bias disfavours ionized ^{218}Po from being seen. To obtain an unbiased sample, a ^{222}Rn decay was only accepted if the daughter ^{218}Po would still be in the bulk LAr at the time of its decay whether it was ionized or not. A precise definition of this cut can be found in Table 8.3.

A histogram of the drift velocities after the anti-biasing cut can be seen in Fig. 8.24. There exists a clear separation between the neutral and ion drift velocities. The fraction of ionized ^{218}Po is 0.36 $\pm$ 0.03(stat.)$\pm$0.04(syst.), with the statistical error

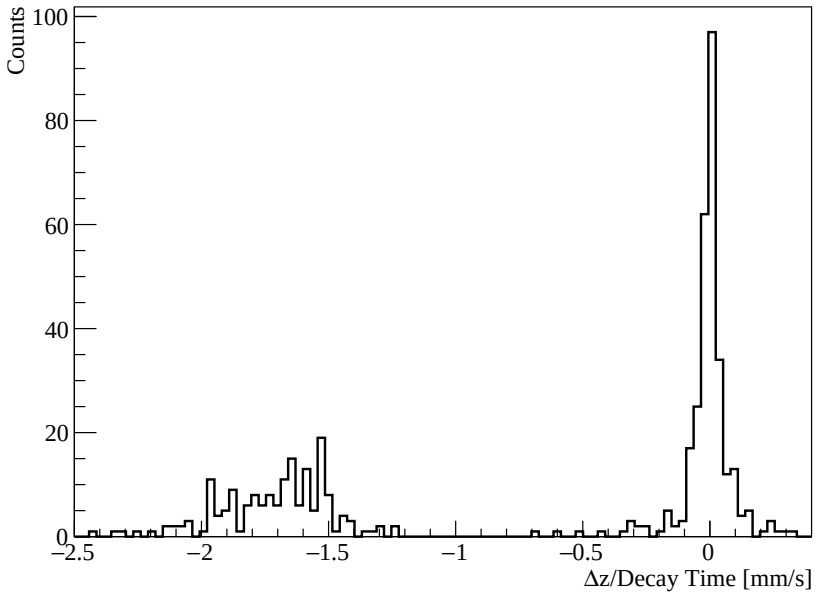

Figure 8.24: The distribution of drift velocity of ^{218}Po after the ^{222}Rn alpha decay. The events at 0 mm/s are neutral ^{218}Po and the events at -1.5 mm/s at positively charged. The fraction of ionized ^{218}Po is 0.36±0.03(stat.)±0.04(syst.).

coming from Poisson counting statistics and the systematic error coming from the data selection cuts.

8.7 Surface Backgrounds in DarkSide-50

The long-lived nature of ^{210}Pb means that both ^{210}Pb and its daughter, ^{210}Po, remain inside DarkSide-50 for a long time after being exposed to ^{222}Rn. They are known as surface backgrounds due to their tendency to get trapped on either the fused silica windows or the Teflon reflector. Pulse-shaped discrimination prevents the ^{210}Pb beta decay from being a background concern, but the ^{210}Po alpha decay can be more troubling for a couple reasons: one, the alpha can lose energy in the wall material and fall within the region of interest; and two, the alpha can be directed into the wall, sending the low energy daughter nucleus recoiling into the liquid.

Requirement	Description
$z_{\mathrm{Po}} > z_{\mathrm{cathode}} + 5\,\mathrm{mm}$	Remove coincidences where the ^{218}Po is near the bottom of the TPC. This prevents ionized ^{218}Po that is stopped by the cathode from influencing the mean ion drift velocity.
$r_{\mathrm{Rn}} < 15\,\mathrm{cm}$ $r_{\mathrm{Po}} < 15\,\mathrm{cm}$	Prevent coincidences near the wall (where the electric field is less understood) from influencing the mean ion drift velocity.
$-\Delta z \cdot \frac{\sin(\pi/8)\cdot \mathrm{s}}{\mathrm{mm}} < \Delta t < -\Delta z \cdot \frac{1\cdot \mathrm{s}}{\mathrm{mm}}$	This is the green dashed line cut in Fig. 8.23.
$-z_{\mathrm{Rn}} + \frac{1}{\tan(\pi/8)} \cdot \frac{\mathrm{mm}}{\mathrm{s}} \cdot \Delta t < 34.7\,\mathrm{cm}$	Require the z-position of the ^{222}Rn decay (z_{Rn}) to be high enough that the ^{218}Po would still be in the bulk even if it drifted with the maximum possible speed toward the cathode before decaying (represented by the lower green dashed line in Fig. 8.23).

Table 8.3: Definitions of cuts used in the ^{222}Rn–^{218}Po analysis. The first two are applied to all coincidences. The third is applied only in the calculation of the ion drift velocity, and the fourth is used only in the calculation of the ion fraction. The decay time is referred to as Δt. The variables x, y, and z refer to the Cartesian coordinates of the isotope indicated in the subscript, with $r = \sqrt{x^2 + y^2}$.

This section is an exhaustive study of ^{210}Po within DarkSide-50, with the ultimate goal of setting a surface background estimation for the DarkSide-50 blind analysis campaign.

8.7.1 The Wall Effect

Before delving too deeply into a discussion of ^{210}Po, first an introduction must be given of the "wall effect". The wall effect is a hypothesis that explains a phenomenon seen in DarkSide-50 that greatly reduces the size of S2 for certain events, such as ^{210}Po, that take place on the Teflon wall surfaces.

The suggested mechanism is that the drift electrons produced in an interaction have some probability of being trapped or absorbed by the wall as they drift upward alongside it. This can cause an event that would have had a large S2 to have a much smaller S2, or no S2 at all.

The Missing S2 Problem

The wall effect finds its roots with a problem that was identified very early in the operation of DarkSide-50: many events are completely missing an S2 pulse.

In the analysis of the 70-day dark matter search [28], there are several cuts that depend on the S2 pulse. These are:

1. S2 size: The pulse following S1 must be at least 100 PE.
2. S2 shape: The pulse following S1 must have an f_{90} less than 0.1.
3. Number of pulses: There must be exactly two pulses (or three, if the third is a small pulse from the photo-ionization of the cathode).
4. Fiducial cut: The event must not occur near the top or bottom of the detector. The drift time between the first and second pulse must be in the range [40 µs, max drift time−40 µs].
5. The S1 maximum fraction: The limit set on the allowed S1 fraction in a single PMT is dependent on the drift time.

The effect of these cuts on the data are shown in Fig. 8.25.

In Fig. 8.25 (top) are the events with the S2 cuts listed above turned off (all other cuts are still applied).

Fig. 8.25 (middle) shows what happens after we remove events that contain only a single pulse. This greatly reduces the number of events in the high f_{90} region of

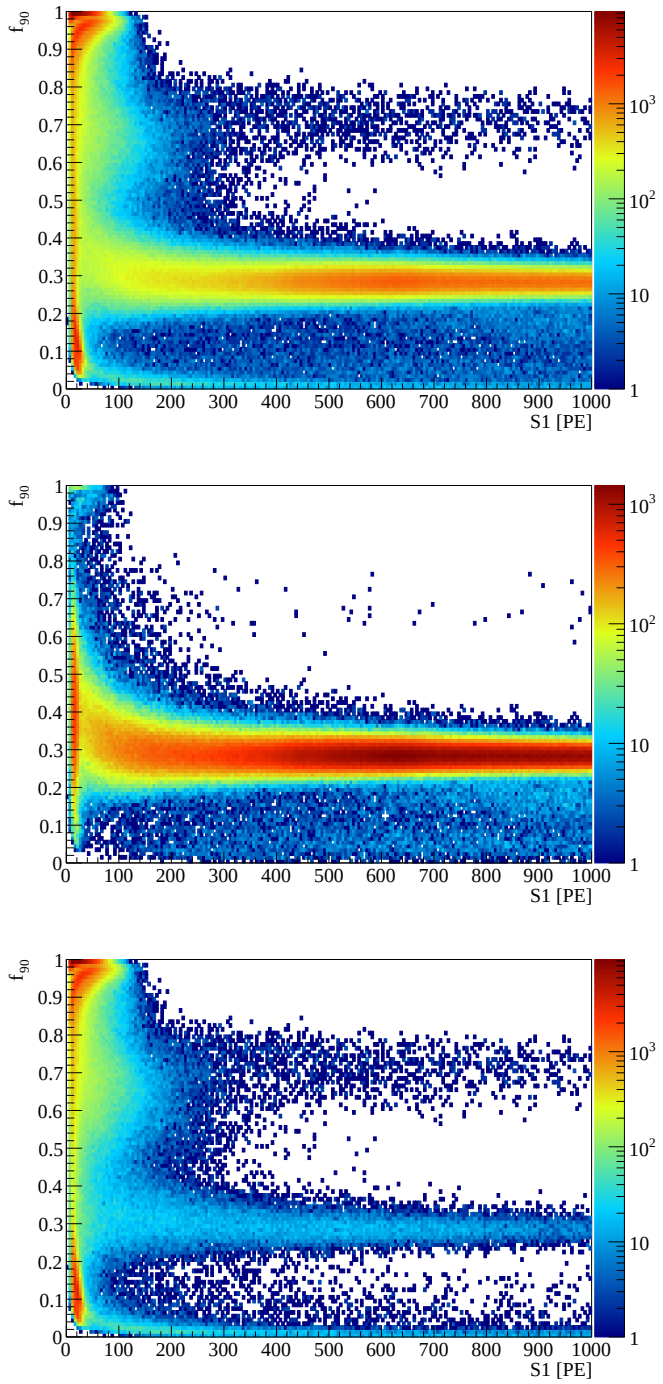

Figure 8.25: Data from the DarkSide-50 70-day dark matter search campaign. **Top**: No cuts involving S2 or drift time have been applied. **Middle**: A cut requiring there to be more than one pulse has been applied to the top histogram. **Bottom**: A cut requiring there to be exactly one pulse has been applied to the top histogram. This shows that most of the events in the nuclear recoil $f_{90}\sim0.7$ region are missing an S2 pulse.

interest (the remaining cuts – drift time and maximum S1 fraction – remove the last few events in this region).

Lastly, Fig. 8.25 (bottom) shows the subtraction of the second figure from the first, selecting only events that have a single pulse. We call these events "S1-only" events.

Many of the S1-only events are in the 0-100 PE range, and can be explained as pure Cherenkov events in the fused silica or Teflon, which deposit no energy in the LAr and therefore produce no S2 signal. However, pure Cherenkov events do not get larger than 100-200 PE, so this cannot explain the presence of the more energetic events.

Supporting Evidence

The probability that a given interaction will produce no S2 will be called P_{noS2}. If the proposed mechanism of drift electrons being lost to the wall is correct, several predictions can be made about P_{noS2}:

1. P_{noS2} should be 0 for events that take place in the bulk argon, since there is no place for the drift electrons to go but up.

2. P_{noS2} should be inversely correlated with the S1 of a surface event. This is because all else being equal (i.e. same type of interaction), an event with smaller S1 will produce fewer drift electrons.

3. P_{noS2} should be positively correlated with drift time, because the further along the wall the electrons have to drift, the higher the probability they have of getting lost.

Unfortunately, due to the very nature of the S2 problem, it is difficult to pinpoint the locations of these interactions, since the x, y, and z reconstruction depend entirely on S2.

Fortunately, ^{210}Po gives us a unique ability to know that an event comes from the surface solely based on its S1. We can look at events in the alpha S1 spectrum that fall below the full 5.3 MeV ^{210}Po alpha energy and know that they must be alphas degraded by the surface material (alphas with full energies below 5.3 MeV do exist in the upper decay chains, but these are not present in the bulk liquid for reasons described in Chapter 5).

See Fig. 8.26 to see what happens to the alpha spectrum when S2 cuts are applied. For alphas, a more strict version of the S2 size cut is needed to remove photoionization pulses (see Sec. 8.4.1). As indicated by the figure, the S2 cuts affect the surface and sub-surface ^{210}Po part of the spectrum, while the full peaks of the ^{222}Rn and ^{218}Po alphas remain. This confirms prediction (1).

Furthermore, an inverse relationship is found between an alpha's S1 and the likelihood that it is missing S2, with a higher proportion of alphas with an S1 of 10000 PE having no S2 than alphas with an S1 of 35000 PE. This confirms prediction (2).

The effect of drift time upon P_{noS2} can be seen by selecting events in the ^{210}Po range that *do* have an S2 pulse.

Fig. 8.27 shows the selection of events in the ^{210}Po S1 range ([10000, 37000] PE) with an S2 pulse. This figure tells us that at 0 drift time the ^{210}Po events have S2s with the expected magnitude (the expected log(S2/S1) for alphas is [−0.5,0.3] (see Fig. 8.13)), but they rapidly decrease in size with increasing drift time. After a depth of 50 µs, ^{210}Po with "regular" S2 magnitudes become rare, until the maximum drift time is reached, where many regular S2s appear again. The existence of many normal-sized S2s at the maximum drift time is expected, as events on the cathode surface can take place far from the side walls.

P_{noS2} has been shown to be correlated with drift time for surface events, confirming prediction (3). It was also shown that the expected size of S2 decreases with drift

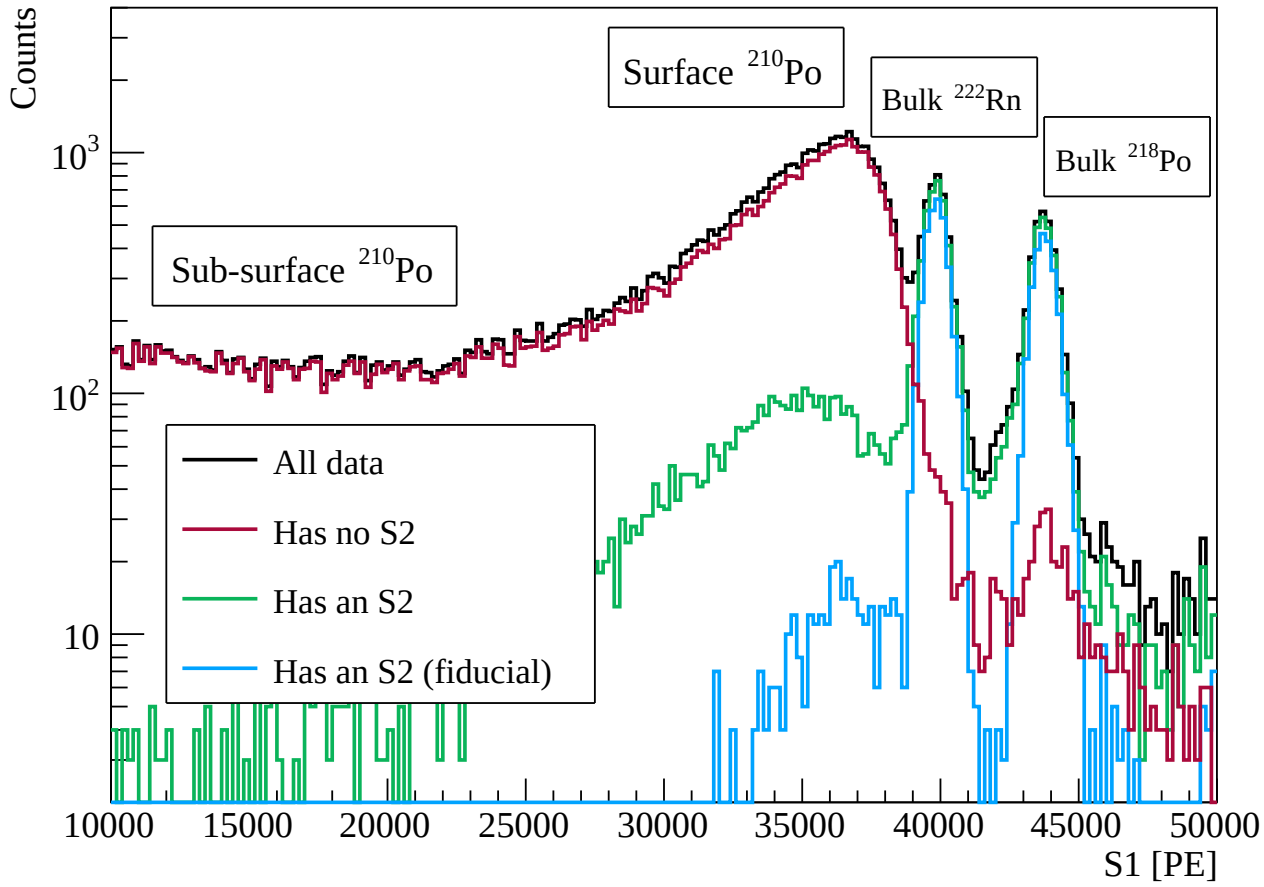

Figure 8.26: **Black**: All alpha events. **Red**: Events with no pulses passing the S2 cuts. **Green**: The events with a pulse passing the S2 size and shape cuts. **Blue**: The events with a pulse passing the S2 size and shape cuts, and the drift time cut.

time, suggesting that as the ionization electrons drift along the wall, they are lost one by one rather than all at once.

The behavior of ^{210}Po surface alphas is in line with what is predicted by the wall effect. The impact of the wall effect on surface backgrounds is discussed in Sec. 8.7.3.

8.7.2 ^{210}Po Rate and Position Reconstruction

To determine the level of background expected from surface backgrounds, the event rate and position of the ^{210}Po must be determined.

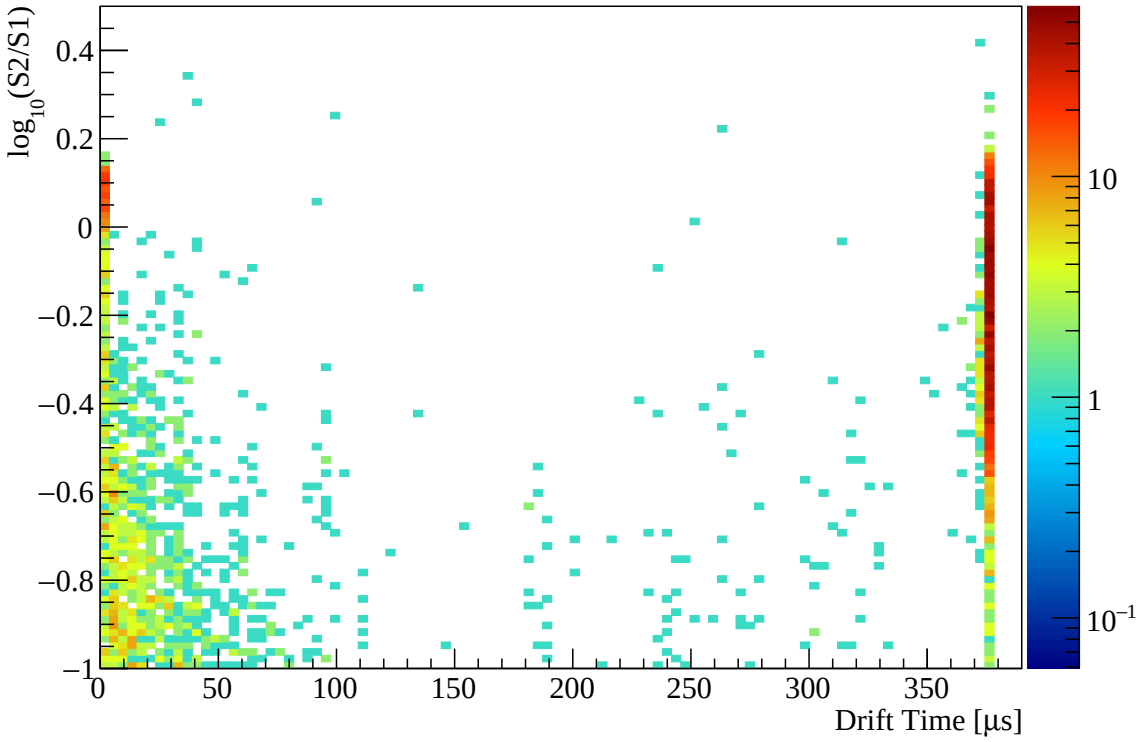

Figure 8.27: ^{210}Po events that have at least one pulse that satisfies the S2 size (>100 PE) and shape (f_{90}<0.1) cuts. The vertical axis is the logarithm of S2 (corrected for saturation) divided by S1 (corrected for saturation and z-position). The downward trend of log(S2/S1) as drift time increases from 0 to 50 µs indicates that the probability of losing drift electrons to the wall increases with drift time. The "regular" sized S2s in the upper right are from cathode ^{210}Po.

Based on the insights from the wall effect, ^{210}Po will be broken up into separate categories, and the rates will be determined for each one:

1. ^{210}Po with S2.
   (a) From the anode or grid (drift time <5 µs).
   (b) From the wall (drift time >5 µs and <371 µs)
   (c) From the cathode (drift time >371 µs).
2. ^{210}Po without S2 (assumed to be entirely from the wall).

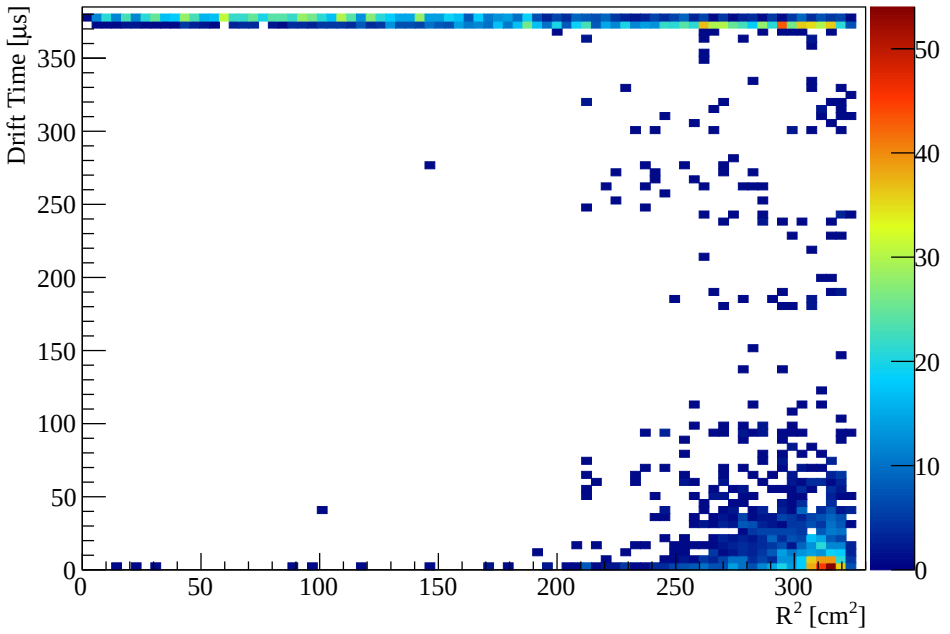

Figure 8.28: Position reconstruction of ^{210}Po alphas events that have S2.

A ^{210}Po event is defined to have an S2 if exactly one of the pulses following S1 satisfies the S2 size and shape cut and an additional alpha-S2 cut: $\log(S2/S1) > -1$ (this is to remove photo-ionization S2s seen in Fig. 8.27). It is defined to have no S2 if none of the pulses following S1 satisfy these cuts.

The position reconstruction of events in category (1) can be seen in Fig. 8.28. As expected, the ^{210}Po are found at high radius, except for the cathode which sees a uniform distribution. The wall effect can be seen again in this figure by the decreasing number of wall events with drift time.

Not many ^{210}Po events appear to be coming from the anode or grid in this figure, but there are a few reasons that they could be under-represented. The signal that the alpha would make as it passes from the anode surface through the argon gas pocket and into the liquid has not been studied, but it very likely produces a different pulse shape. Even alphas from the grid, which would deposit their full energy in the liquid only, may not have a long enough drift time for the S1 and S2 to be separated by the

Description	Location	Rate ($\mathrm{mBq\,m^{-2}}$)
^{210}Po with S2	anode/grid	unknown
^{210}Po with S2	wall	0.059 ± 0.002
^{210}Po with S2	cathode	0.449 ± 0.010
^{210}Po without S2	wall	2.247 ± 0.011

Table 8.4: ^{210}Po rates in DarkSide-50. Errors are statistical.

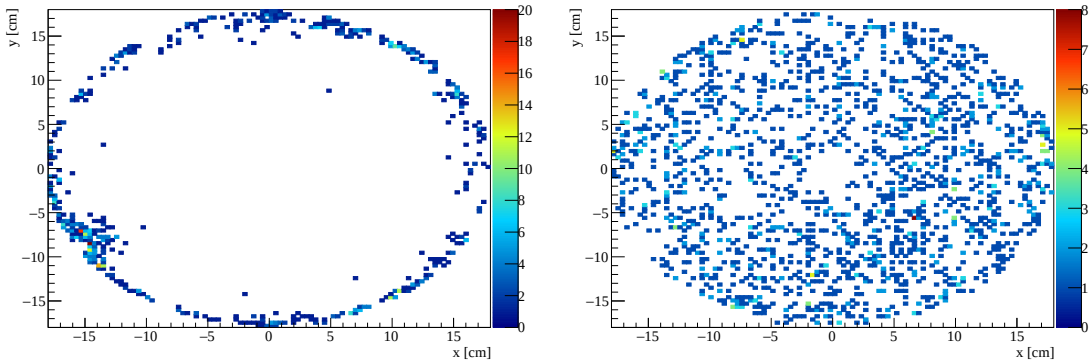

Figure 8.29: xy-position reconstruction of ^{210}Po alphas events that have S2. **Left**: Wall events. The cluster in the bottom left is due to a field anomaly of the drift field in that region which shifts drift electrons inward. **Right**: Cathode events.

pulse-finding algorithm. They would appear as events with a low f_{90} and avoid the alpha selection cuts. For a measurement of the anode/grid ^{210}Po levels the low-level reconstruction codes would have to be reworked.

The xy-reconstruction of the wall and cathode events are found in Fig. 8.29. The cluster in the bottom left of the wall events xy plot is due to a field anomaly of the drift field in that region which shifts drift electrons inward. It is suspected that this field anomaly reduces the wall effect in this region slightly by pulling electrons away from the wall.

The rates for the different categories of ^{210}Po are found in Table 8.4.

8.7.3 Background Estimate

In DarkSide-50's 70-day dark matter search campaign there were many S1-only events in the WIMP region (reminder: Fig. 8.25 (bottom)). If just one of these happens to have an S2, it can end DarkSide-50's prospects as a background-free experiment. In this section, the background risk from these events in a longer, blinded campaign will be examined.

To assess the risk of background from the prompt S1-only events, it helps to break them down into collectively exhaustive categories.

S1-only events can be:

(1) Events that did not produce an S2 in the first place.

(2) Events that did produce an S2, but that S2 was lost for some reason (such as the wall effect).

Class (1) events can become a background if:

(a) An unrelated S2-like pulse falls within the window.

Class (2) events can become a background if:

(a) An unrelated S2-like pulse falls within the window.

(b) Its S2 does not get lost to some effect.

The (a) options require the existence of random and unrelated "S2-only" events that could by chance pile up with an S1-only event in an accidental coincidence. S2-only events do exist and are studied by collaborator Alissa Monte, but are unrelated to surface backgrounds. This study will focus on option (2b) and explore possibility of the S2 *not* getting lost.

Projecting the Wall Effect to Low S1

The figure of interest for the DarkSide-50 blind analysis is the number of surface background events expected in the WIMP search region for a given exposure. This rate will given in terms of events per 500 days of exposure and will be denoted R_{SB}.

Given that no surface backgrounds have been seen in the previous 50 day or 70-day search results published by DarkSide-50, R_{SB} had to be estimated in a roundabout way using the following formula:

$$R_{SB} = \int_{60PE}^{460PE} \frac{dR_{S1O}}{dS1}(S1) \cdot P_{S1O-S2}(S1) \cdot dS1$$

Where $\frac{dR_{S1O}}{dS1}(S1)$ is the rate of S1-only events in an area dS1 of the dark matter search region, and $P_{S1O-S2}(S1)$ is the probability for an event with a given S1 to gain an S2 (or rather, not lose its S2 to the wall effect). The integral bounds, 60 PE and 460 PE, are the lower and upper bounds of the WIMP search region.

The $\frac{dR_{S1O}}{dS1}$ term is obtained simply by looking at the data from the 70-day campaign and counting the number of S1-only events in the WIMP box that pass all other cuts. The WIMP box that was used here has been amended from the one used for the 70-day analysis by adding a cutoff at low energy (60 PE) and high f_{90} (0.9), as these are the minimum changes that are planned for the 500-day campaign. The final box's dimensions will be likely be even smaller, so this represents a conservative figure for the S1-only rate.

In order to take into account the effect of the fiducial cut and the maximum S1 fraction cut, both of which depend on the drift time, the estimated drift time for an S1-only event was obtained using the S1 top-bottom asymmetry (Fig. 8.17).

The result can be seen in Fig. 8.30, with the WIMP search box shown in red.

P_{S1O-S2} was obtained by observing the trend of missing S2s with S1 size. Fig. 8.31 shows the fraction of surface events with a given S1 that passed all analysis cuts,

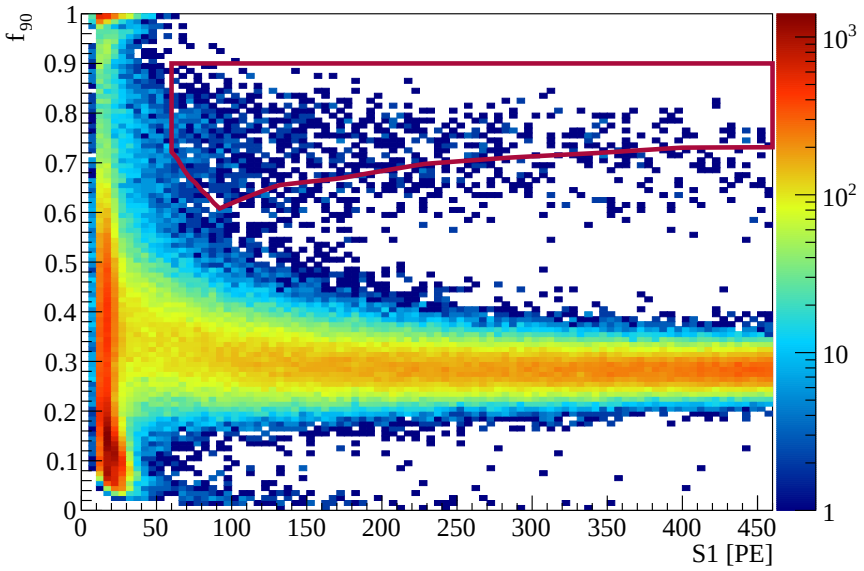

Figure 8.30: The DarkSide-50 70-day campaign with all analysis cuts applied except S2 cuts. Since DarkSide-50 did not have any background events in the 70-day campaign after all cuts were applied, this means that every event in the WIMP search region (red) failed the S2 cuts. The overall rate of these "S1-only" events is of interest for future background predictions.

including S2 cuts, and fall in a modified WIMP box that has been extended out to higher S1 values. The S1 range begins at 600 PE, which is the upper end of the blinded region, and ends at 37000 PE, such that only ^{210}Po surface alphas were selected.

Even at high S1 values of 35000 PE, less than 1 in 100 surface events retained their S2. At 20000 PE and below there were no surface events that passed all cuts, save for an event at 3000 PE and another at 7000 PE. Upon closer evaluation of these two events, they had S2s just large enough to pass the loose S2 size cut that was used for alphas ($\log(S2/S1) > -1$), but still far too small to pass any reasonable nuclear recoil S2/S1 cut that will implemented in the analysis of the 500-day campaign. In fact requiring events to have $\log(S2/S1) > 0.5$ would remove all the events in Fig. 8.31, even those at 35000 PE, while retaining nearly 100% nuclear recoil acceptance in the WIMP region.

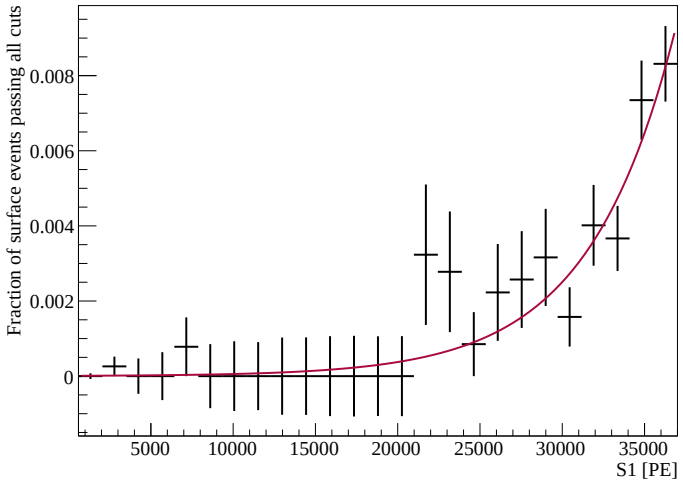

Figure 8.31: The fraction of surface events that pass all analysis cuts, including a 90th percentile nuclear recoil f_{90} cut, as a function of S1. The fraction of background events decreases toward smaller S1 because of the wall effect: a smaller S1 means a smaller S2, which means a greater likelihood of the S2 being lost and failing the S2 cuts. The x-axis begins at 600 PE because this is the upper end of the blinded region.

The lack of any potential background signals from surface events in the region from 20000 PE down to 600 PE gives us confidence that there will also be no surface backgrounds in the blinded region below 600 PE. Quantifying this confidence is difficult. Fitting an exponential curve to this graph (Fig. 8.31 (red line)) and extrapolating $\mathrm{P_{S1O-S2}}$ down into the WIMP region seems dubious, since the mechanism behind the wall effect is not well enough understood to expect any sort of exponential behavior. Nevertheless, we will proceed with the estimation, and any statistical confidence will be heavily modified by systematic uncertainties.

To make the calculation of $\mathrm{R_{SB}}$ both simpler and more conservative, $\mathrm{P_{S1O-S2}}$ was taken as a constant 9.5×10^{-6}, which is the value of the exponential fit at 600 PE. It can then be moved out of the integral and $\mathrm{R_{SB}}$ becomes:

$$\mathrm{R_{SB}} = \mathrm{R_{S1O}} \cdot \mathrm{P_{S1O-S2}}$$

Where R_{S1O} is the total rate of S1-only events in the WIMP box in Fig. 8.30: 907 events/70 days or 6478 ± 215 events/500 days.

This results in $R_{SB} = 0.062 \pm 0.002$ events/500 days, with several important caveats that will be reiterated:

- An S2/S1 cut designed for nuclear recoils, while not used for the 70-day campaign, is expected to be put in place for the 500-day campaign, and will drastically reduce the surface alpha acceptance.

- A fiducial cut in radius, again not used in the 70-day campaign, is expected to be put in place, reducing surface backgrounds further.

- Systematic uncertainties remain significant. The value $P_{S1O-S2} = 9.5 \times 10^{-6}$ was extrapolated from a fit and not empirically verified. With only 907 S1-only events in the WIMP box from the 70-day campaign, P_{S1O-S2} could be as high as 10^{-4} or 10^{-3} and the observed outcome of 0 background events would still be reasonable.

- If the wall effect depends on the electric field near the walls, then temporal changes in that field may influence its effect. There is currently a known field anomaly beneath one of the PMTs, and it tends to pull drift electrons inward, away from the wall (see Fig. 8.29). This could suppress the wall effect and enhance the S2 size under that PMT. In the 70-day campaign the field anomaly was evidently not strong enough to result in any background events, but a new or worsening field anomaly could introduce higher levels of surface background. The size of field anomalies should be carefully monitored throughout the 500-day campaign.

- A TPB tail cut based on the results discussed in Sec. 7.2 can suppress surface backgrounds in DarkSide-50 by orders of magnitude. This will be studied in Sec. 8.8.

8.8 TPB Tail

Some of the contents of Sec. 8.8 were presented at TAUP 2017 [82]

The long-lived component, or "tail", of TPB scintillation, as measured in Sec. 7.2 by RaDOSE, is also seen in DarkSide-50. As a recap, two major discoveries from RaDOSE were:

1. The UV photons emitted by argon scintillation, when absorbed by TPB, can be re-emitted in the tail, but this process is rare.

2. The scintillation from alphas travelling through TPB contains a majority of light in the tail.

In DarkSide-50, the presence of the S2 pulse complicates the study of the TPB tail, as it falls between 0 and 376 µs after S1. It also produces a UV induced TPB tail of its own. Therefore, we define the "tail region" to be the segment of the waveform beginning 10 µs after the start of S1 (at which point all LAr scintillation has ceased) up until the beginning of S2. This avoids contamination from the S2 pulse, and any photoelectrons detected in this region can be attributed to the TPB tail from S1. Unfortunately, this means that events with short drift times can have very small tail regions.

Examples of UV-induced TPB tails in DarkSide-50 can be seen in Fig. 8.32. The top figure features an event has an S1 of 440 PE, with 3 PE in the tail region. The bottom figure features a much larger event, with an S1 of ∼40000 PE. The tail is more pronounced as well, with 290 PE in the tail region. The factor of 100 increase in S1 led to a factor of 100 increase in the TPB tail. The TPB tail can also be seen following the S2 pulse, which in this event is similar in size to S1.

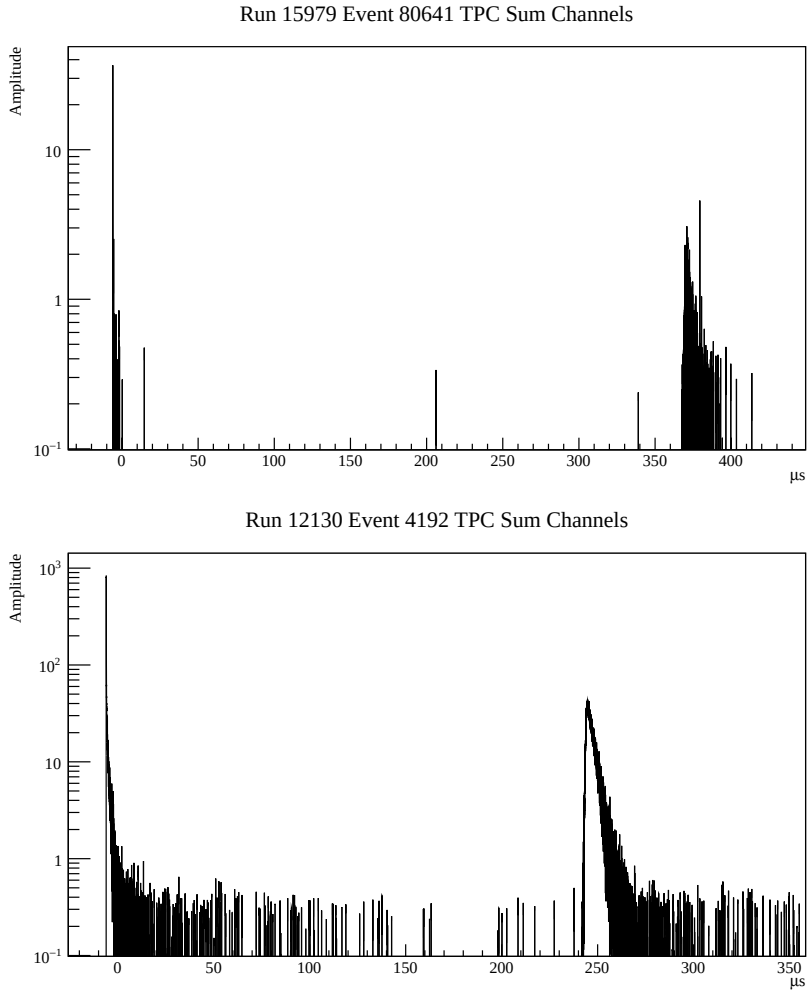

Figure 8.32: Events in DarkSide-50 with varying sizes of S1 and TPB tail. The top event has an S1 of 440 PE and has 3 PE in the region between S1 and S2: at 15 µs, 210 µs, and 340 µs. The bottom event has an S1 of 40000 PE and has nearly 300 PE in the tail region.

The WIMP search region in DarkSide-50 has an upper bound of less than 500 PE, so WIMP events in this region are expected to have between 0 and 3 PE in the tail region, depending on S1 size and the placement of the S2 pulse within the waveform.

An example of alpha scintillation in the TPB can be seen in Fig. 8.33. The event featured in this figure has an S1 of 390 PE (recalling that in DarkSide-50 S1 is defined as the integral of the first 7 µs of the pulse only). The event features 250 PE in the tail region, which in this case extends out to the end of the acquisition window because

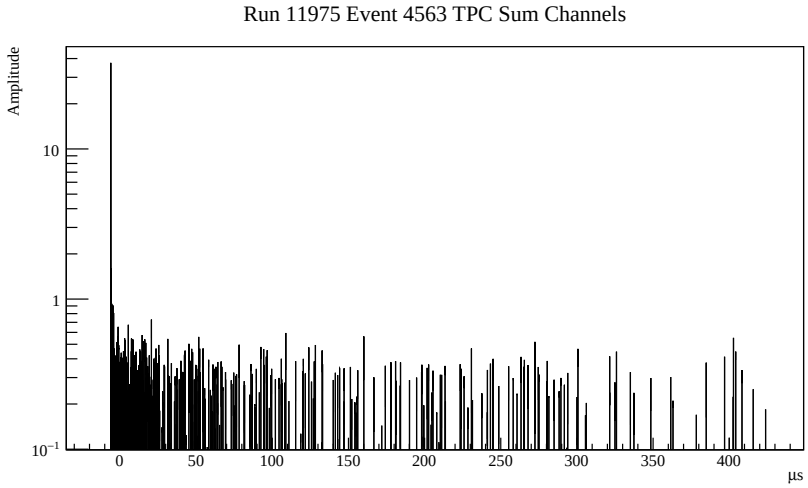

Figure 8.33: A surface alpha decay in DarkSide-50. The number of photoelectrons in the tail (250 PE), is large in comparison to its S1 size (390 PE).

there is no S2 pulse. This tail contains two orders of magnitude more photoelectrons than the comparably sized "regular" event from Fig. 8.32.

The lack of S2 for this event is not a surprise either, as surface events are expected to be correlated with S1-only events via the wall effect (Sec. 8.7.1).

8.8.1 Tail Cut

A data selection cut was designed to tag the TPB tail from surface events in order to alleviate the uncertainty surrounding the wall effect's suppression of surface backgrounds.

The design goal of the "TPB tail cut" was to maximize the suppression of surface events while retaining a 99% acceptance of all nuclear recoils in the LAr. This was achieved using the DarkSide-50 nuclear recoil calibration data taken with an ^{241}AmBe neutron source placed directly outside the cryostat.

Neutron events were selected by requiring them to pass all TPC analysis cuts and to fall within the WIMP box, while at the same time requiring a coincident signal in the liquid scintillator veto corresponding to the 4.4 MeV gamma ray energy from the

^{241}AmBe source. This requirement suppressed external backgrounds and coincident gamma gays from the ^{241}AmBe source.

The tail cut was defined by setting the 99th percentile upper limit on the number of photoelectrons in the tail region as a function of both S1 and drift time.

The procedure went as follows:

1. A series of `N` points were chosen along the drift time range, called `DTpoints`. The first point was at 10 µs, while the `N`th point was the maximum drift time of 376 µs.

2. A series of `N` scatter plots, called `ScatterPlots`, were defined with each `ScatterPlots[i]` corresponding to a drift time `DTpoints[i]`. The x-axis of the scatter plot was S1 and the y-axis was TPE, where TPE stands for "tail PE" and is the number of PE between 10 µs and `DTpoints[i]`.

3. A loop over every neutron event was performed, and for each neutron event a loop over `DTpoints` was performed, until the value of `DTpoints[i]` exceeded the drift time of the event. In each iteration of the loop, TPE was calculated and the event was added to `ScatterPlots[i]`. See an example of a scatter plot in Fig. 8.34.

4. Each `ScatterPlots[i]` was binned in S1 and a loop over the S1 bins was performed. For each bin, the mean value of TPE was recorded. See the red graph in Fig. 8.34.

5. The graph of mean TPE values for each scatter plot was fit with a linear function. See the green line in Fig. 8.34.

6. The constant of the fitted line was raised until 99% of the events in the scatter plot fell below the line. See the blue line in Fig. 8.34.

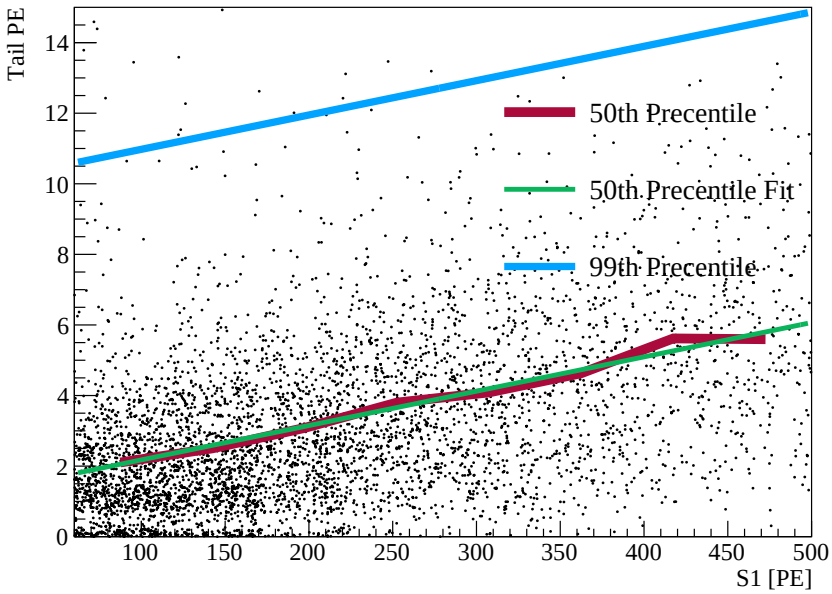

Figure 8.34: Scatter plot of photoelectrons in the tail region versus S1 for neutron events with a drift time greater than 275 µs. The red graph follows the 50th percentile, and the green line is a linear fit to the graph. This line is elevated with constant slope until 99% of neutron events fall below it (blue line). This is repeated for each drift time value, and the 99th percentile curves for each drift time are collected together into a single 2D histogram: Fig. 8.35.

7. The N lines representing the 99% nuclear recoil acceptance for a given drift time and S1 were compiled into a single 2D histogram (Fig. 8.35).

In effect, this process increases the available statistics by using every event for every drift time slice up until its S2.

To determine if a given event passes the tail cut, the value in the 2D histogram corresponding to the event's drift time and S1 is looked up. If the number of PE in the event's tail region (10 µs up to the beginning of S2) exceeds this value, then it has a larger TPB tail than 99% of neutrons, and should be cut.

This procedure can be repeated for any desired level of nuclear recoil acceptance.

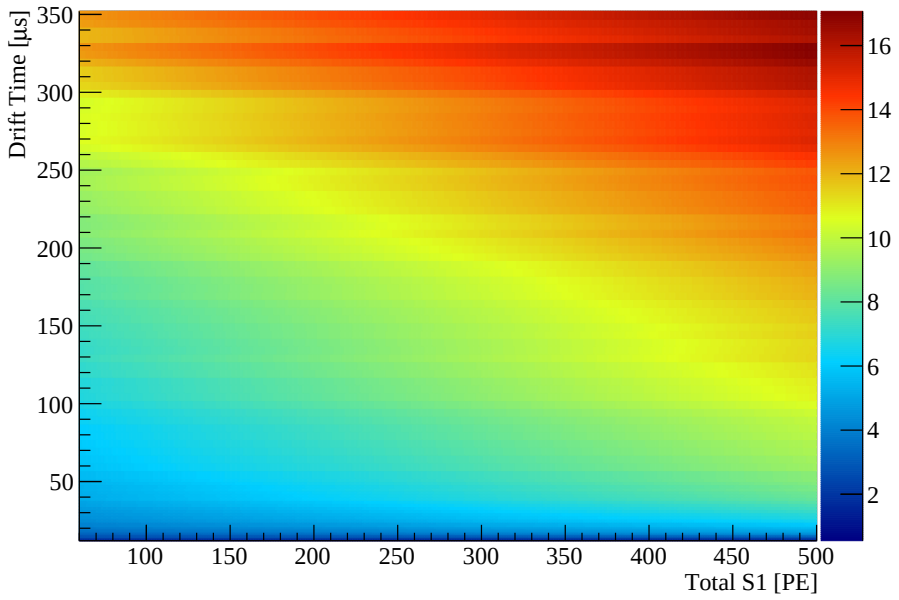

Figure 8.35: A 2D histogram forming a lookup table for the 99th percentile values of TPE for a nuclear recoil event with a given S1 and drift time. Example: An event has a drift time of 200 µs and an S1 of 300 PE. According to this figure, 99% of nuclear recoils with these parameters have 11 or fewer photoelectrons in the tail region.

8.8.2 Cut Effectiveness

The effectiveness of the cut toward suppressing surface backgrounds was determined with RaDOSE data. A selection of surface alpha decays were obtained through the deposition of radon daughters on a TPB-coated quartz slide placed in a LAr volume, and tagging the alpha in the ^{214}Bi–^{214}Po coincidence (see Sec. 7.2).

The lack of S2 in the RaDOSE measurement meant that the acceptance of each event could be calculated for each of the drift time values. In other words, for each alpha event, the number of TPE in each of the `N` regions [10 µs,`TDbins[i]`] was determined and compared to the 99th percentile value obtained from Fig. 8.35. While the light yield in RaDOSE was about 25% lower than in DarkSide-50, it was assumed that this had an equivalent effect on both the S1 and the TPE so no correction was needed.

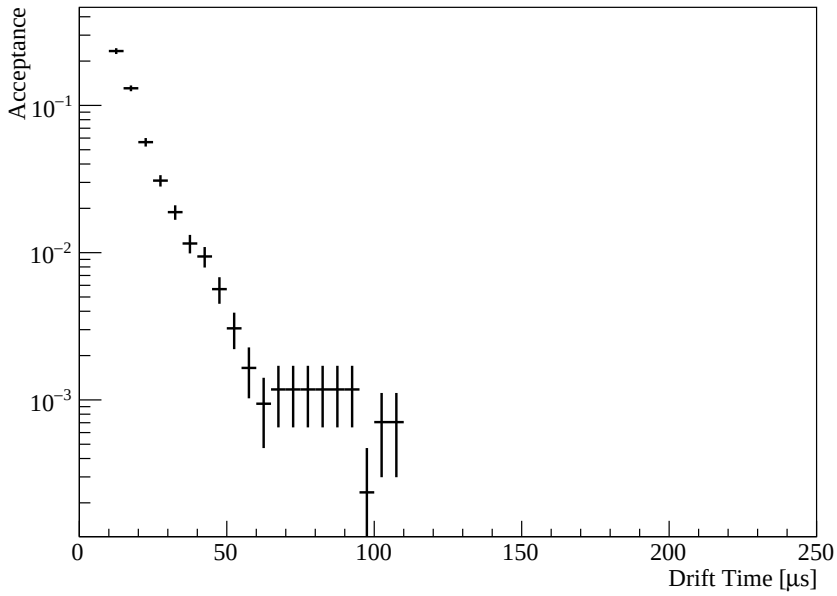

Figure 8.36: Surface background acceptance as a function of drift time. The longer the drift time, the longer the tail region between S1 and S2, and the easier it is to separate an event with a large tail (alpha in TPB) from an event with a small tail (recoil in LAr).

The results can be seen in Fig. 8.36. Not unexpectedly, the surface background acceptance was found to decrease with drift time, because a longer tail region provides a greater ability to distinguish the size of the TPB tail.

The fiducial volume in DarkSide-50 extends from 40 to 336 µs. Under the assumption that surface events are distributed uniformly in drift time, the integrated acceptance over this range is 0.0005 ± 0.0001. However, due to the wall effect, DarkSide-50 is biased toward seeing surface events near the top of the detector. The acceptance at 40 µs can therefore be taken as an upper limit: 0.0094 ± 0.0015.

The estimated surface background rate from Sec. 8.7.3 was 0.062 events/500 days. In the worst-case scenario that all the surface events are concentrated at a drift time of 40 µs, the surface background after the tail cut becomes:

$$\mathrm{R_{SB}}(\text{After worst-case tail cut}) = 0.00058 \pm 0.00009\,\text{events/500 days}$$

Even without a radial fiducial cut or S2/S1 cut, which would suppress this value further, the expected surface background rate is far below DarkSide-50's design goal of 0.1 background events. Systematic effects, while still not fully understood, are unlikely to affect this rate by the orders of magnitude needed for it to pose a threat to DarkSide-50's background-free operation.

Chapter 9

Conclusions

Alphas and surface backgrounds in liquid argon detectors are a concern for dark matter searches because of their ability to create WIMP-like signals. Using the RaDOSE detector, we discovered a long-lived component of TPB scintillation that enables an effective suppression of these signals. When applied to the DarkSide-50 dark matter search campaign, it reduces the expected number of these background events well below the design specifications.

Appendix A

Scintillation of Organic Compounds

What follows is an English translation of a French paper by R. Voltz and G. Laustriat [62], entitled "Radioluminescence des milieux organiques I", which aids in the understanding of the long-lived scintillation component of TPB. Assistance in translation was provided by the online tools Google Translate [83] and BonPatron [84].

Introduction

Interest in laws governing the decay of scintillation in organic media, for applications in radiation detection, has given rise to many experimental studies [1]. In various cases, the existence of two components in the light emission has been demonstrated; the first, known as "fast", is characterized by high intensity and a comparable decrease in the fluorescence from the scintillator, while the second ("slow" component), less intense, decreases much more slowly, in a non-exponential. For a given scintillator, the relative importance of each component varies with the nature of the incident

radiation [2]; it is the same, therefore, for the shape of the overall light pulse. The work done so far to explain the origin of the two components of the scintillation and to establish the law of decay for scintillation did not lead to definitive conclusions [3-8]. In this study, we resume consideration of these issues (we have already dealt with partially in a previous publication [9]).

Scintillation, having the same spectral composition as fluorescence, must be attributed to the de-excitation of excited molecules in the lowest singlet state. The formation of these molecular levels results from a succession of elementary phenomena which we will examine in the first part of this work, which will lead us to clarify the physical origin of the two components of the scintillation. We will give an analysis of the evolution of molecules in the lowest excited singlet state and the lowest triplet state, then we will establish expressions for the number of photons emitted per particle per unit time ("instantaneous" intensity of scintillation) or during a given time interval ("integrated" intensity). We consider separately the cases of pure aromatic media (single crystals) and binary systems (solution of a fluorescent compound in a liquid aromatic or plastic).

A.1 Formation and evolution of molecular excited states

To describe the formation of activated molecules responsible for scintillation in aromatic crystals, we will consider three successive stages. In the first, which is very short ($\approx 10^{-13}$ s), the incident particle and the secondary electrons are slowed down in the scintillator and produce "primary" activation states, for which it is important to clarify the nature and spatial distribution. In the second stage, energy dissipation processes are accompanied by non-radiative transitions to the lowest excited singlet (S_1) and triplet (T_1) molecular states; the duration of these phenomena is of the order

of 10^{-10} to 10^{-11} s. The evolution of the S_1 and T_1 states thus formed occurs during a final stage, the length of which is approximately equal to (or greater than) 10^{-9} s, and can be studied by current experimental means.

A.1.1 Primary Molecular States

Created by primary and high-energy secondary particles, excited molecular states and ionized molecules with activation energy E undergo electronic transitions with dipole moment μ, or oscillator strength f, mainly due to collisions, with the cross section approximately proportional to the quantity μ^2 or the ratio f/E [10,11].

For aromatic molecules, the direct excitation of the molecules in the T_1 and S_1 states are respectively forbidden for reasons of spin and symmetry, and are therefore unlikely. According to spectroscopy measurements in the far ultraviolet [12] and inelastic scattering of fast, mono-energetic electrons [13,14], the most frequent transitions are, on the other hand, to excited singlet levels of energy slightly lower than E_i, the first ionization state, or to states of "superexcitation" of energy higher than E_i [11,15,16]; we denote excited molecules in the singlet levels by S_n.

The majority of products from the ionizing collisions of the secondary electrons have too low kinetic energy ($T \lesssim 500\,\mathrm{eV}$) to move away from the parent molecule at a distance greater than r_0, for which the Coulomb interaction energy is equal to kT [17]. In condensed non-polar media, it is generally accepted that the preferential recombination of these electrons occurs very quickly ($\approx 10^{-11}$s); the molecule thus formed will be on a higher energy level, with equal likelihood to be in a singlet state (S_n) or in one of the three triplet states (T_n); the formation of the latter is statistically favored. Note also that the slow electrons can excite the molecules in a triplet state directly by an electronic exchange process, whose cross section is maximum at an energy slightly higher than the triplet level and decreases rapidly for higher energies [10].

As the slow secondary electrons have a large cross section of elastic collision with the molecules of the medium, they induce active products that accumulate in small volumes which we shall call "clusters" ("blobs" [17]), which have centers that are close to the path of the primary particle and whose radius is of the order of the distance r_0 defined above.

After the passage of ionizing particle, one can distinguish two regions in the medium, respectively characterized by high and low local concentrations of activated molecules, and whose relative importance depends on the ionizing power of the incident radiation. In the case of heavy ions (protons, alphas, etc.) of high specific energy loss, they form an area of high density activation, cylindrical and centered on the trajectory of the incident particle ("trace"), materialized by clusters and the S_n molecules excited by the primary particle; the radius of this track is the order of r_0. Outside this region are dispersed molecules activated by the energetic secondary electrons (radiation delta) with less energy than the primary ionizing particle. For incident radiation characterized by a low linear energy transfer (gamma rays, fast electrons, etc.), the mean free path between collisions is higher than for heavy particles: the excited molecules along the primary path remain dispersed and do not form a continuous activation column. Areas of high excitation density are then reduced to clusters and traces formed by the secondary electrons with ionizing power.

A.1.2 Evolution of Primary Molecular States

S_n and T_n molecules are subjected to non-radiative processes, which lead to lower electronic levels and, in general, the same multiplicity. These transitions can be followed by ionization (for superexcited states) or nuclear reorganization with dissociation, isomerization, or internal conversion to the states S_1 and T_1.

In areas of low concentration of active products, the role of the external environment in the evolution of the primary excited states is to merely absorb excess energy

of molecular vibration. In areas of high activation density, we believe the influence of perturbations in the vicinity of other activated products must also be considered. Thus, in the intense electric field created by a transitional free charge, a molecule in a high energy primary excited state undergoes rapid electronic rearrangement and, with high probability, is brought to an ionized state [18]. Ionization of a primary excited molecule can also be caused by the interaction with another primary excited molecule; this is a result of a transition effect with a significant dipole moment μ, and the likelihood of the process is proportional to the amount μ^2 [19].

The interaction process between the primary activation products therefore results in the ionization of S_n molecules. In the subsequent recombination of the ions, the T_n state formation is statistically favored, and the local concentration of these within the high-density zones of activation is increased at the expense of singlet-level molecules. These triplet states are in addition to those mentioned above and due to the slow secondary electrons in the clusters; traces are then characterized by a high concentration of excited molecules in the T_1 state (particularly from the internal conversion $T_n \rightarrow T_1$). Subsequently, we assume that at the end of the non-radiative transitions to lower levels, these molecules are distributed in the track following a Gaussian law:

$$C_T(r) = \frac{1}{\pi r_0^2} \frac{\mathrm{d}N_T}{\mathrm{d}x} \exp\left[-(r/r_0)^2\right] \tag{A.1}$$

where $C_T(r)$ represents the local concentration at a distance r from the trajectory, and dN_T/dx the number of molecules in the state T_1 per unit of distance covered by the particle that generated the track; r_0, the length characterizing the lateral distribution of the excited molecules, is on the order of the radius of the clusters caused by the slow secondary electrons.

A.1.3 Evolution of the Low Energy Excited States

In the final stage of scintillation, excited molecules in the S_1 and T_1 levels (the lowest) are subjected to various intra- and intermolecular processes whose list is shown in Table 1. For binary systems, the kinetic scheme takes into account the energy transfer from the state of the substrate S_1 to the first level of the fluorescent solute singlet F_l (F_0: ground state); the mechanism of this process of energy transition has been studied recently [20]. The reactions (1) to (5) and (12) to (16) are usually considered to account for the fluorescence induced by ultraviolet light, and are well known [21]; the process (5), (8) and (16), in particular, correspond to the degradation of the electronic energy under the influence of an inhibitor product Q, wherein in the aromatic solutions is often dissolved oxygen. Reactions (6) to (11) take into account the disabling process of T_1 states. Of particular note are the bi-molecular annihilation reactions (9) to (11), highlighted and studied recently [22]; triplet-triplet interaction can lead to singlet, triplet and quintuplet (Q_1) states. The overall rate constant of the bimolecular annihilation of T_1 states χ_{tt} is given by:

$$\chi_{tt} = 2k_{tt} + k'_{tt} + 2k''_{tt} \tag{A.2}$$

The molecules excited by corpuscular radiation is distributed in limited areas where the concentration can be much higher than in the rest of the medium. In addition to the mentioned process, we must also consider the diffusion phenomena to establish the equations giving the variation over time of the concentrations C_s, C_T, and C_f of excited molecules in states S_1, T_1, and F_1, respectively. The kinetic

		Process	Rate Constant
(1)	$S_1 \rightarrow S_0 + h\nu_s$	fluorescence	(k_s)
(2)	$S_1 \rightarrow T_1$	singlet − triplet conversion	(k'_s)
(3)	$S_1 \rightarrow S_0$	internal conversion	(k''_s)
(4)	$S_1 + S_0 \rightarrow S_0 + S_0$	mutual conversion	(k_{ss})
(5)	$S_1 + Q \rightarrow S_0 + Q$	external conversion	(k_{sq})
(6)	$T_1 \rightarrow S_0 + h\nu_T$	phosphorescence	(k_t)
(7)	$T_1 \rightarrow S_0$	internal conversion	(k'_t)
(8)	$T_1 + Q \rightarrow S_0 + Q$	external conversion	(k_{tq})
(9)	$T_1 + T_1 \rightarrow S_1 + S_0$	triplet − triplet annihilation	(k_{tt})
(10)	$T_1 + T_1 \rightarrow T_1 + S_0$	triplet − triplet annihilation	(k'_{tt})
(11)	$T_1 + T_1 \rightarrow Q_1 + S_0$	triplet − triplet annihilation	(k''_{tt})
(12)	$S_1 + F_0 \rightarrow F_1 + S_0$	energy transfer	(k_{sf})
(13)	$F_1 \rightarrow F_0 + h\nu_f$	fluorescence	(k_f)
(14)	$F_1 \rightarrow F_0$	internal conversion	(k'_f)
(15)	$F_1 + F_0 \rightarrow F_0 + F_0$	mutual conversion	(k_{ff})
(16)	$F_1 + Q \rightarrow F_0 + Q$	external conversion	(k_{fq})

Table A.1: Evolution of the lowest energy excited molecular states

equations are:

$$\frac{\partial}{\partial t}C_s = D_s \Delta C_s - \frac{1}{\tau_s}C_s + k_{tt}C_T^2 \tag{A.3}$$

$$\frac{\partial}{\partial t}C_T = D_T \Delta C_T - \frac{1}{\tau_T}C_T - \chi_{tt}C_T^2 + k'_s C_s \tag{A.4}$$

$$\frac{\partial}{\partial t}C_f = D_f \Delta C_f - \frac{1}{\tau_f}C_f + k_{sf}[F]C_s \tag{A.5}$$

where D_s D_T, and D_f as diffusion coefficients of these molecules.

We also have:

$$\frac{1}{\tau_s} = k_s + k'_s + k''_s + k_{ss}[S_0] + k_{sq}[Q] + k_{sf}[F] \tag{A.6}$$

$$\frac{1}{\tau_T} = k_t + k'_t + k_{tq}[Q] \tag{A.7}$$

$$\frac{1}{\tau_f} = k_f + k'_f + k_{ff}[F] + k_{fq}[Q] \tag{A.8}$$

where τ_s, τ_f, and τ_T denote, respectively, the decay time constants of the fluorescence of the solvent and solute, and the phosphorescence of the substrate. $[S_0]$, $[Q]$, and $[F]$ represent the concentration of non-excited molecules in the substrate, the inhibitor compound, and the fluorescent solute.

A.1.4 Origin of the Two Scintillation Components

After the preceding production of molecular states S_1 by ionizing radiation, light emission of the scintillator takes place through two main modes.

The excitement of the scintillator molecules to singlet states (S_n) and subsequent internal conversion to the S_1 states is too fast to be followed by the current experimental techniques; the appearance of excited molecules in the state S_1 can be considered as instantaneous. The corresponding light pulse, which we shall call the prompt signal, has a very short rise time and the decay depends on the kinetics of molecules in the scintillator in the S_1 state.

Excited molecules in the first singlet level also result from the interaction between two T_1 states (reaction (9) in the chart); they are formed very quickly, with high local concentrations in the particle traces. The formation of S_1 states is then delayed and we call the corresponding transmission the delayed signal; in this case, the shape of the light pulse depends on the evolution of the scintillator and the excited molecules in the singlet and triplet states.

The actual pulse shape of the flash of light emitted by the scintillator, as observed experimentally, results from the superposition of the prompt and delayed signals. Similarly, the integrated intensity of the scintillation is the sum of integrated intensities of each signal.

A.2 Scintillation intensity of pure aromatic compounds

Even at high radiation intensities, the overlap of traces from different charged particles is negligible; the kinetics of the activated states in the scintillator is then identical to that of the molecules excited by an individual particle. Let us consider successively the intensity of the prompt and delayed signals of the scintillation.

A.2.1 Prompt Signal

The local concentration C_s of molecules in the state S_1, which are the source of the prompt emission, satisfies the kinetic equation:

$$\frac{\mathrm{d}}{\mathrm{d}t}C_s = D_s \Delta C_s - \frac{1}{\tau_s}C_s \tag{A.9}$$

where τ_s is given by the relation (6) wherein the term $k_{sf}[F]$ is neglected. By integration over all space, and time interval (0, t), we can show that, if immediately after the passage of the primary and secondary particles, $N_s(0)$ molecules are excited to the S_1 state, their number at time t is given by:

$$N_s(t) = N_s(0)\exp(-t/\tau_s).$$

We then obtain the expression of the signal intensity of the prompt:

$$I(t) = k_s N_s(0) \exp(-t/\tau_s) \tag{A.10}$$

as well as that of the integrated intensity over the time interval (0, t_0):

$$L(0, t_0) = \eta_s N_s(0)[1 - \exp(-t_0/\tau_s)] \tag{A.11}$$

where $\eta_s = k_s \tau_s$ denotes the fluorescence quantum yield of the scintillator. The total number of photons emitted in the prompt signal is given by:

$$L = L(0, \infty) = \eta_s N_s(0). \tag{A.12}$$

Note that Gervais de Lafond [6,23] considered an equation similar to (9), but with an additional term for bimolecular annihilation, whose influence is reflected by an initial very fast decrease of the light intensity, which has not been demonstrated experimentally. Moreover, this author believes that the bimolecular inhibition of two S_1 states may explain the effects of degradation of the molecular excitation energy observed for particles of high ionizing power ("ionization quenching"). The study of the influence of the nature of ionizing particles on the performance of the scintillation [2], however, led us to admit that these phenomena result from inhibition of the interaction between primary states of high excitement, and that they are too fast to affect the decay law of scintillation.

A.2.2 Delayed Signal

The S_1 singlet states responsible for the delayed transmission are formed by triplet-triplet interactions in areas of high ionization density, essentially constituted by the trace of the incident particle if it is characterized by a high linear energy loss; the

intensity of the delayed signal is then obtained by considering the kinetics of excited molecules in the S_1 and T_1 levels in this primary path. With little ionizing radiation (fast electrons, for example), high density activated regions created by secondary electrons are scattered along the course of the primary particle; in this case, to determine the intensity of the delayed signal, it is necessary to study the kinetics of excited molecules in one of these secondary traces, the overall effect being obtained by summing over all of them.

Local concentrations C'_s and C_T of the states S_1 (due to the triplet-triplet interaction) and T_1 satisfy the kinetic equations (3) and (4). At the initial instant, defined by the passage of the particle, has $C'_s = 0$. The initial distribution of T_1 states in cylindrical tracks will be characterized by law (1), giving the concentration C_T based on the number dN_T/dx of excited molecules per unit length. Assuming, again, that the linear density dN_T/dx remains constant throughout the length of the trace, concentrations C_T and C'_s depend only on the distance r to the axis and time.

General expressions of instantaneous and integrated intensities — By integrating the function $C_s(r,t)$ over the entire volume of the primary track - or all of the secondary traces - one obtains the total number $N'_s(t)$ of excited molecules in the S_1 level from interacting triplet-triplet states caused by the incident particle; the intensity of the delayed signal is then:

$$I'(t) = k_s N'_s(t) = k_s \int_0^R \mathrm{d}x \int_0^\infty C'_s(r,t) 2\pi r \, \mathrm{d}r \tag{A.13}$$

where R denotes the total length of the traces. Taking into account this relationship, and kinetic equation (3) giving the variations of $C'_s(r,t)$, we deduce that the intensity $I'(t)$ satisfies:

$$\frac{\mathrm{d}I'}{\mathrm{d}t} + \frac{1}{\tau_s} I' = f(t) \equiv k_s k_{tt} \int_0^R \mathrm{d}x \int_0^\infty C_T^2(r,t) 2\pi r \, \mathrm{d}r \tag{A.14}$$

the integral $\int_0^\infty \Delta C'(r,t) 2\pi r dr$ being zero ([1]). Setting $I'(0) = 0$ for the delayed signal, the following expression is obtained:

- Instantaneous intensity:

$$I'(t) = \int_0^t \exp[-(t-\alpha)/\tau_s] f(\alpha)\, \mathrm{d}\alpha \tag{A.15}$$

- Integrated intensity on the interval $(0,t_0)$:

$$L'(0,t_0) = \tau_s \left[\int_0^{t_0} f(\alpha)\, \mathrm{d}(\alpha) - I'(t_0) \right] \tag{A.16}$$

where α is the integration variable.

Calculation of $f(t)$ — This function, defined by equation (14), is obtained by determining the local concentration $C_T(r,t)$ of the excited molecules in the T_1 state by means of kinetic equation (4), taking into account the initial condition (1). In the case of aromatic compounds used as scintillators, the efficacy of the conversion $S_1 \to T_1$ is generally low, so we neglect the term $k'_s C_s$ of the second part of kinetic equation (4), which is then in the form:

$$\frac{\partial}{\partial t} C_T(r,t) = D_T \Delta C_T(r,t) - \frac{1}{\tau_T} C_T(r,t) - \chi_{tt} C_T^2(r,t). \tag{A.17}$$

To solve this nonlinear differential equation, we use approximation methods whose nature depends on the relative importance of second order terms.

[1] If v and s respectively denote the volume of the trace and the delimiting surface, where n is a unit normal vector to the latter:

$$\int_v \Delta C'_s \, \mathrm{d}v = \int_s \boldsymbol{\nabla} C'_s \mathbf{n} \, \mathrm{d}s$$

The concentration gradient having only a radial component that tends to zero for large values of r makes the above amounts zero.

When considering only the diffusion process, the variation of the concentration Γ of the molecules in the T state is given by the relation:

$$\Gamma(r,t) = \frac{\mathrm{d}N_T/\,\mathrm{d}x}{\pi r_0^2(1+t/t_a)}\exp\left[-\frac{r^2}{r_0^2(1+t/t_a)}\right]. \tag{A.18}$$

At the center of the track, this concentration decreases according to the law: $C_T(t) = C_T(0)(1+t/t_a)^{-1}$, where $C_T(0) = \mathrm{d}N_T/\pi r_0^2\,\mathrm{d}x$ is the initial concentration, and $t_a = r_0^2/4D_T$ is the "decay time".

If we consider at present only the process of bimolecular annihilation, we get a similar law with a decay time given by $t_b = [\chi_{tt}C_T(0)]^{-1}$. The decreased local concentration of T_1 states will be controlled by one of the two phenomena characterized the shortest decay time. For particles with high ionizing power, the concentration $C_T(0)$ can be great enough that the term $\chi_{tt}C_T^2$ is initially the most important. After a while, however, the local concentration in the trace decreases sufficiently, and the diffusion term becomes and remains dominant.

Under these conditions, the differential equation (17) can be solved by an approximation method devised by Jaffé [24,25] which assumes that the spatial distribution of excited molecules, initially given by equation (1), remains Gaussian in shape at all times, despite the bimolecular annihilation that continues to unfold. Specifically, we look for a solution of the form:

$$C_T(r,t) = \gamma(t)\Gamma(r,t) \tag{A.19}$$

where Γ is the distribution function (18) of states T_1, if only the diffusion process is considered, and $\gamma(t)$ an unknown function to be determined. For this purpose, we substitute expression (19) in the equation (17) and integrate over the entire volume, giving:

$$\frac{\mathrm{d}}{\mathrm{d}t}N_T(t) + \frac{1}{\tau_T}N_T(t) = -\chi_{tt}\int_0^R \mathrm{d}x \int_0^\infty C_T^2(r,t)2\pi r\,\mathrm{d}r \tag{A.20}$$

where $N_T(t)$ denotes the total number of molecules in the T_1 state, present at the instant t, the time since the incident particle:

$$N_T(t) = \int_0^R \mathrm{d}x \int_0^\infty C_T(r,t) 2\pi r \, \mathrm{d}r.$$

Knowing that:

$$\int_0^R \mathrm{d}x \int_0^\infty \Gamma(r,t) 2\pi r \, \mathrm{d}r = N_T(0)$$

and

$$\int_0^R \mathrm{d}x \int_0^\infty \Gamma^2(r,t) 2\pi r \, \mathrm{d}r = \frac{C_T(0) N_T(0)}{2(1 + t/t_a)}$$

we obtain the equation:

$$\frac{\mathrm{d}}{\mathrm{d}t}\gamma(t) + \frac{1}{\tau_T}\gamma(t) = -\frac{\gamma^2(t)}{2t_b(1 + t/t_a)}$$

which, with the initial condition $\gamma(0) = 1$, gives the expression:

$$\gamma(t) = \frac{\exp(-t/\tau_T)}{1 + \frac{t_a}{2t_b}\exp(\frac{t_a}{\tau_T})\left[\mathrm{Ei}(-\frac{t+t_a}{\tau_T}) - \mathrm{Ei}(-\frac{t_a}{\tau_T})\right]} \tag{A.21}$$

where $\mathrm{Ei}(-x) = -\int_x^\infty \frac{e^{-\alpha}}{\alpha}\,\mathrm{d}\alpha$.

Finally, given the relations (19) and (21), the function $f(t)$ is written:

$$f(t) = \frac{k_s}{2t_b}\frac{k_{tt}}{\chi_{tt}} \frac{N_T(0)\exp(-2t/\tau_T)}{\left\{1 + \frac{t_a}{2t_b}\exp\left(\frac{t_a}{\tau_T}\right)\left[\mathrm{Ei}(-\frac{t+t_a}{\tau_T}) - \mathrm{Ei}(-\frac{t_a}{\tau_T})\right]\right\}^2 (1 + t/t_a)} \tag{A.22}$$

Note that in the case of pure aromatic compounds, the lifetime τ_T of the T_1 states is generally very much greater than the duration of scintillation ($\tau_T = 10^{-2}\,\mathrm{s}$ for monocrystalline anthracene, for example [26]); the conditions $t \ll \tau_T$ and $t_a \ll \tau_T$ are then satisfied and the expression (22) tends to the following simplest form:

$$f(t) \simeq \frac{k_s}{2t_b}\frac{k_{tt}}{\chi_{tt}}\frac{N_T(0)}{\left[1+\frac{t_a}{2t_b}\log(1+t/t_a)\right]^2(1+t/t_a)} \tag{A.23}$$

which we will use to determine the instantaneous and integrated delayed signal intensities of pure organic scintillators.

Instantaneous Intensity — It's expression, according to the relationship (15) is given by:

$$\begin{aligned} I'(t) =& \frac{k_s}{2t_b}\frac{k_{tt}}{\chi_{tt}}N_T(0)\times \\ & \int_0^t \frac{\exp[-(t-\alpha)/\tau_s]\,\mathrm{d}\alpha}{\left[1+\frac{t_a}{2t_b}\log(1+\alpha/t_a)\right]^2(1+\alpha/t_a)} \end{aligned} \tag{A.24}$$

We verify that the intensity of the delayed signal $I'(t)$ is initially given by the slope $f(0) = (k_s k_{tt}/2t_b\chi_{tt})N_T(0)$, and passes through a maximum on the curve at $\tau_s f(t)$. On the other hand, as $f(t)$ is a function that varies slower than the exponential $\exp(-t/\tau_s)$, it can be shown that $I'(t)$ asymptotically approaches $\tau_s f(t)$ for time t such that $t \gg \tau_s$ ([2]). Under these conditions, the decay of the delayed signal is given

[2]Substituting $\alpha = tx$, expression (15) becomes:

$$I'(t) = t\int_0^1 \exp\big[-\frac{t}{\tau_s}(1-x)\big]f(tx)\,\mathrm{d}x.$$

As t/τ_s increases, the exponential factor quickly becomes very small, except for values of x in the vicinity of $x = 1$ wherein the function $f(tx)$ varies very little. Under these conditions, if $t/\tau_s \gg 1$:

$$I'(t) \simeq tf(t)\int_0^1 \exp\big[-\frac{t}{\tau_s}(1-x)\big]\,\mathrm{d}x \simeq \tau_s f(t).$$

by:

$$I'(t) \simeq \tau_s \frac{k_s}{2t_b} \frac{k_{tt}}{\chi_{tt}} \frac{N_T(0)}{\left[1 + \frac{t_a}{2t_b} \log(1 + t/t_a)\right]^2 (1 + t/t_a)} \tag{A.25}$$

Integrated Intensity — Expressing $I'(t_0)$ using the asymptotic expression (25) you obtain, using equation (16):

$$L'(0, t_0) = \eta_s \frac{k_{tt}}{\chi_{tt}} N_T(0)[1 - F(t_0)] \tag{A.26}$$

with:

$$F(t_0) = \frac{1}{1 + \frac{t_a}{2t_b} \log\left(1 + \frac{t_0}{t_a}\right)} \times \left(1 + \frac{\tau_s}{2t_b} \frac{1}{\left[1 + \frac{\tau_s}{2t_b} \log\left(1 + \frac{t_0}{t_a}\right)\right](1 + \frac{t_0}{t_a})}\right)$$

Note that if $\tau_s \leq t_b$ and $t_0 \gg t_a$, the function $F(t_0)$ tends to the simplest form:

$$F(t_0) \simeq \left[1 + \frac{t_a}{2t_b} \log(1 + t_0/t_a)\right]^{-1} \tag{A.27}$$

The overall number of photons emitted in the delayed signal is given by:

$$L' = L'(0, \infty) = \eta_s \frac{k_{tt}}{\chi_{tt}} N_T(0). \tag{A.28}$$

A.3 Scintillation Intensity of Binary Aromatic Systems

The light emission of these scintillators is due to the radiative decay of solute molecules excited by an energy transfer from the solvent S_1 levels, which result either from excitement to a high energy state followed by internal conversion, or a triplet-triplet interaction in the particle traces. As for pure organic media, we then consider the

prompt and delayed signals, whose intensity is obtained by a generalization of previous calculations, and taking into account the kinetics of the excited molecules of the solute, as described by equation (5) and the initial condition $C_f = 0$.

A.3.1 Signal Prompt

If $N_s(0)$ denotes the number of molecules of the substrate in the S_1 state immediately after the passage of the particle, it is easily shown that the number $N_f(t)$ of excited solute molecules present at time t is given by:

$$N_f(t) = k_{sf}[F]N_s(0)\frac{\tau_s\tau_f}{\tau_f - \tau_s}[\exp(-t/\tau_f) - \exp(-t/\tau_s)].$$

The intensity of the prompt signal is then expressed as:

$$I_f(t) = \eta_f\epsilon_{sf}N_s(0)\frac{1}{\tau_f - \tau_s}[\exp(-t/\tau_f) - \exp(-t/\tau_s)] \tag{A.29}$$

where $\eta_f = k_f\tau_f$ denotes the fluorescence yield of the solute and $\epsilon_{sf} = k_{sf}[F]\tau_s$ the efficiency of the electronic energy transfer process between the substrate and solute. In practice, for concentrations of solute ϵ_{sf} sufficiently close to unity, the condition $\tau_s \ll \tau_f$ is satisfied; the decay of intensity is then described by:

$$I_f(t) \simeq \frac{\eta_f\epsilon_{sf}}{\tau_f}N_s(0)\exp(-t/\tau_f). \tag{A.30}$$

It can be verified as well that the overall number L_f of photons emitted in the prompt signal is:

$$L_f = \eta_f\epsilon_{sf}N_s(0). \tag{A.31}$$

A.3.2 Delayed Signal

As for the pure aromatic compounds, the number $N'_s(t)$ of excited molecules in the substrate S_1 state from triplet-triplet interaction is given by the expression:

$$N'_s(t) = (k_s)^{-1} \int_0^t \exp[-t(t-\alpha)/\tau_s] f(\alpha)\, \mathrm{d}\alpha$$

which, for $t \gg \tau_s$, tends to the asymptotic form:

$$N'_s(t) \simeq (\tau_s/k_s) f(t).$$

The number $N'_f(t)$ of excited solute molecules satisfies the differential equation:

$$\frac{\mathrm{d}}{\mathrm{d}t} N'_f(t) = -\frac{1}{\tau_f} N'_f(t) + k_{sf}[F] N'_s(t)$$

and the initial condition $N'_f(0) = 0$. We deduce then the expression of the intensity I'_f of the delayed signal:

$$\begin{aligned} I'_f(t) &= k_f N'_f(t) \\ &= k_f k_{sf}[F] \int_0^t \exp[-(t-\alpha)/\tau_f] N'_s(\alpha)\, \mathrm{d}\alpha \end{aligned}$$

or even, for $t \gg \tau_s$:

$$I'_f(t) = \frac{k_f \epsilon_{sf}}{k_s} \int_0^t \exp[-(t-\alpha)/\tau_f] f(\alpha)\, \mathrm{d}\alpha. \tag{A.32}$$

For reasons similar to those mentioned in footnote ([2]), since $f(t)$ varies slower than $\exp(-t/\tau_f)$, if $t \gg \tau_f$ it yields the relationship:

$$I'_f(t) = \frac{\eta_f \epsilon_{sf}}{k_s} f(t) \tag{A.33}$$

which describes the decay of the delayed signal at times t such that $t \gg \tau_s$ and $t \gg \tau_f$. We have already seen that the $\tau_s \ll \tau_f$ condition is usually satisfied; for the commonly used fluorescent compounds, lifetime τ_f is of the order of 10^{-9} s [27], equation (33) will therefore apply to time intervals where $t \gtrsim 10^{-8} s$.

For scintillators containing no inhibitory substances such as oxygen, which results in the degradation of T_1 energy states, the term [Q] in equation (7) is negligible and the lifetime τ_T is similar to that observed with the crystal [28]. Under these conditions, the function $f(t)$ is given by (23) and you obtain, for the intensity of the delayed signal, the expression:

$$I'_f(t) = \frac{k_f \epsilon_{sf}}{2t_b} \frac{k_{tt}}{\chi_{tt}} N_T(0) \times \int_0^t \frac{\exp[-(t-\alpha)/\tau_f]\, \mathrm{d}\alpha}{\left[1 + \frac{t_a}{2t_b} \log(1 + \alpha/t_a)\right]^2 (1 + \alpha/t_a)} \tag{A.34}$$

which gives the following asymptotic form:

$$I'_f(t) \simeq \eta_f \epsilon_{sf} \frac{k_{tt}}{\chi_{tt}} \frac{N_T(0)}{\left[1 + \frac{t_a}{2t_b} \log(1 + t/t_a)\right]^2 (1 + t/t_a)} \tag{A.35}$$

Similarly, it shows that the total number L'_f of photons emitted by the particle in the delayed signal is expressed by:

$$L'_f(t) = \eta_f \epsilon_{sf} \frac{k_{tt}}{\chi_{tt}} N_T(0). \tag{A.36}$$

In the very important particular case of non-degassed liquid scintillators, the dissolved oxygen is a highly effective inhibitor; the term $k_{tq}[Q]$ then becomes dominant in equation (7) [28], and the lifetime τ_T is not much greater than the duration of the scintillation. For the expression $I'_f(t)$, consider then the function $f(t)$ in its non-simplified

form (22); the decay of the delayed signal, in particular, takes place according to the law:

$$I'_f(t) \simeq \eta_f \epsilon_{sf} \frac{k_{tt}}{\chi_{tt}} \frac{1}{2t_b} \frac{N_T(0) \exp(-2t/\tau_T)}{\left\{1 + \frac{t_a}{2t_b} \exp\left(\frac{t_a}{\tau_T}\right) \left[\mathrm{Ei}(-\frac{t+t_a}{\tau_T}) - \mathrm{Ei}(-\frac{t_a}{\tau_T})\right]\right\}^2 (1 + t/t_a)}. \quad \text{(A.37)}$$

This work allowed us to establish the theoretical expressions for scintillation intensity, from analysis of the primary process caused by particles and the kinetics of the metastable states S_1 and T_1 that form. In the next paper, these expressions will be confronted with experimental results obtained with crystals and organic liquid solutions. We can then check the validity of this kinetic study and evaluate various parameters (r_0, D_T, K_{tq}, ...) characterizing the initial distribution and evolution of the excited states created in aromatic media by ionizing particles.

Appendix A References

[1] Birks (J.B.), The Theory and Practice of Scintillation Counting, Pergamon Press, 1964, chap. 6.

[2] Voltz (R.), Pfeffer (G.), Lopes Da Silva (J.) et Laustriat (G.), Symposium International de Luminescence (N. Riehl et H. Kallmann, dit.), Verlag K. Thiemig, Mnchen, 1966, p. 59.Voltz (R.), Lopes Da Silva (J.), Laustriat (G.) et Coche (A.), J. Chem. Physics, 1966, 45, 3306.

[3] Kallmann (H.) et Brucker (G.J.), Phys. Rev., 1957, 108, 1122.

[4] Kilin (S.F.) et Rozman (I.M.), Opt. and Specty., 1959, 6, 37.

[5] Birks (J.B.), I.R.E. Trans. NS, 1960, 7, 2-3.

[6] Gervais De Lafond (Y.), Thse (3e cycle), Toulouse, 1962.

[7] Gibbons (P.E.), Northrop (D.C.) et Simpson (O.), Proc. Phys. Soc., 1962, 79, 373.

[8] Walter (G.), Thse Sc. Phys., Strasbourg, 1964.

[9] King (T.A.) et Voltz (R.), Proc. Roy. Soc., 1966, A 289, 424.

[10] Mott (N.F.) et Massey (H.S.W.), The Theory of Atomic Collisions, Oxford, 1965; (a) chap. 16 ; (b) chap. 18.

[11] Platzman (R.L.), The Vortex, 1962, 23, 8.

[12] Klevens (H.B.) et Platt (J.R.), J. Chem. Physics, 1949, 17, 470.

[13] Lassettre (E.N.), Rad. Research, suppl. n 1, 1959, 530.

[14] Skerbele (A.) et Lassettre (E.N.), J. Chem. Physics, 1965, 42, 395.

[15] Platzman (R.L.), J. Physique, 1960, 21, 853.

[16] Jesse (W.P.), J. Chem. Physics, 1964, 41, 2060.

[17] Mozumder (A.) et Magee (J.L.), Rad. Research, 1966, 28, 203.

[18] Bethe (H.) et Salpeter (E.E.), Handbuch der Physik, Springer Verlag, Berlin, 1957, 35, 321.

[19] Choi (S.I.), J. Chem. Physics, 1965, 43, 1818.

[20] Voltz (R.), Laustriat (G.) et Coche (A.), J. Chim. Physique, 1966, 63, 1253-1259.

[21] Frster (Th.), Fluoreszenz Organischer Verbindungen, Vandenhoek und Ruprecht, Gttingen, 1951.

[22] Leach (S.) et Migir-Dicyan (E.), Actions chimiques et biologiques des radiations (M. Hassinsky, dit.), 1966, 9, 117.

[23] Blanc (D.), Cambou (F.) et Gervais De Lafond (Y.), J. Physique, 1964, 25, 319.

[24] Jaff (G.), Ann. Phys., 1913, 42, 303.

[25] Magee (J.L.), J. Chem. Physics, 1955, 52, 528.

[26] Kepler (R.G.), Caris (J.C.), Avakian (P.) et Abramson (E.), Phys. Rev. Letters, 1963, 10, 400.

[27] Lami (H.), Pfeffer (G.) et Laustriat (G.), J. Physique, 1966, 27, 398.

[28] Livingston (R.) et Ware (W.), J. Chem. Physics, 1963, 39, 2593.

Appendix B

MgF_2 for Liquid Xenon Surface Backgrounds

In addition to liquid argon (LAr) detectors, liquid xenon (LXe) detectors are also concerned about surface backgrounds. One example is the EXO collaboration's search for neutrinoless double beta decay using ^{136}Xe [85]. They are searching for the following process:

$$^{136}\mathrm{Xe} \rightarrow ^{136}\mathrm{Ba} + 2458\,\mathrm{keV}^1$$

Any other process which emits a gamma with an energy near 2458 kEV is therefore a background concern. One such gamma comes from the beta decay of ^{214}Bi, which emits a 2448 keV gamma with a branching ratio of 1.57% [87].

Normally this signal can be vetoed by the alpha decay of ^{214}Po, the short-lived ($\tau_{1/2} = 164\,\mu\mathrm{s}$) daughter of the ^{214}Bi decay. However, if the ^{214}Po is on the surface of the detector, there is a 50% chance that the alpha will be directed into the wall and escape detection.

[1] [86]

In a TPC setting such as the EXO-200 detector, the drift field is capable of drifting ionized daughters of bulk ^{222}Rn decays into the cathode surface (see Sec. 8.6 and [79]), which makes ^{214}Po on the cathode surface a very real possibility.

The technique described in Chapter 7 for suppressing surface backgrounds in LAr used the organic compound TPB that is already present on the interior surfaces of LAr detectors. The TPB acts as a veto by emitting a pulse of light with a long tail when an alpha particle travels through it.

This technique cannot be directly extended to LXe detectors because LXe is known to dissolve organic compounds [65, 66]. Instead, we propose the use of the inorganic compound MgF_2 as a surface background suppressant in LXe detectors.

MgF_2's use as an optical coating is well established [88]. It can be vacuum evaporated onto a material to form a uniform and insoluble layer of any desired thickness. It is also transparent to LXe scintillation light [89].

One additional property of MgF_2, reported for the first time here, is that it acts a strong scintillator when stimulated with alpha particles. This property is particularly relevant for surface backgrounds, as a coating of MgF_2 could be applied to the detector surface such that the alpha from ^{214}Po decaying on the surface would be seen whether it gets emitted into the LXe or into the MgF_2 wall coating.

B.1 The Detector

The alpha scintillation in MgF_2 was measured using the apparatus described in Sec. 7. To summarize, the detector features two chambers. The upper chamber contains a photomultiplier tube (PMT) that is pointed downward at a quartz window. On the other side of the quartz window is the lower chamber containing a reflecting cup in which a source can be placed. The quartz window forms a hermetic seal with Teflon gaskets to allow the lower chamber to be pumped down to a vacuum.

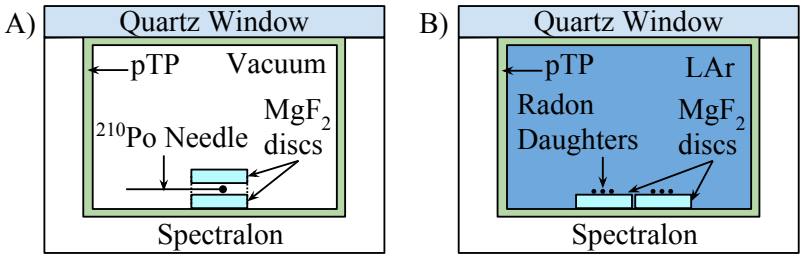

Figure B.1: The configurations of the two measurements.

B.2 The Measurements

Two measurements were performed. Measurement A used a ^{210}Po needle source to measure alpha scintillation in MgF_2 under vacuum conditions at both room temperature and liquid nitrogen temperature. Measurement B used radon daughters directly deposited on MgF_2 discs placed inside an active LAr volume to determine the vetoing power of the MgF_2 scintillation in practice. The configurations of the lower chamber for each measurement can be found in Fig. B.1.

Note: the Spectralon cup and quartz window were coated with the wavelength-shifting compound p-terphenyl (pTP) in order to shift the 128 nm scintillation light to longer wavelengths ($\sim$ 340 nm [90]) for efficient detection. It is assumed to have no impact on the MgF_2 scintillation, which has been measured to have a peak wavelength of 385 nm [91].

B.2.1 Measurement A

The source was constructed by creating a "sandwich" with a ^{210}Po needle source [57] and two MgF_2 discs with 5 mm diameter and 1 mm thickness, held together with clear tape along the edges of the discs. A diagram and picture of the sandwich can be found in Fig. B.2.

The sandwich was placed inside the Spectralon reflecting cup in the lower chamber of the detector (Fig. B.1 (A)). After the detector was closed, a -1100 V bias was applied to the PMT and the scintillation pulses were recorded with the data

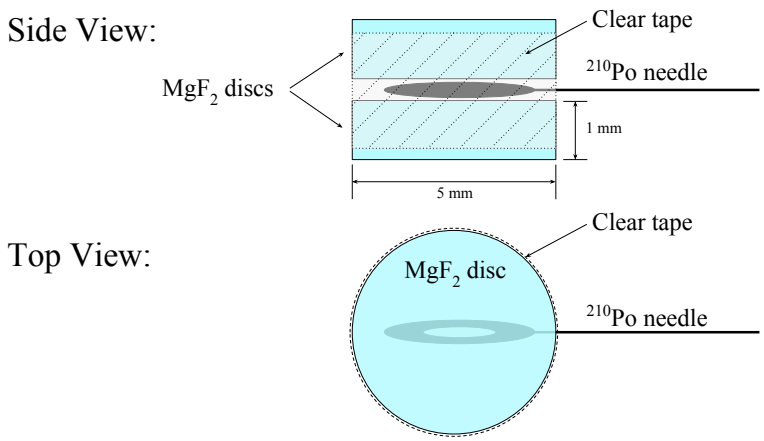

(a) A diagram of the source used for the vacuum measurements.

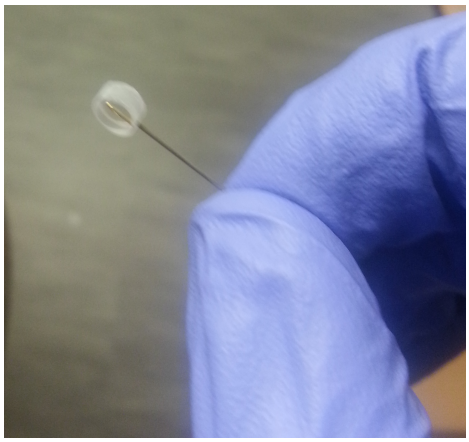

(b) A picture of the source.

Figure B.2: To produce alpha scintillation in MgF_2, a ^{210}Po needle source was sandwiched between two MgF_2 discs held together with clear tape.

acquisition system described in Chapter 7. This was done first at room temperature (295 K), then the lower chamber was submerged in a LN_2 bath and left for one hour to equilibrate to 77 K before taking data again.

Results

MgF_2 exhibited scintillation under alpha excitation at both 295 K and 77 K. The lifetime of the scintillation pulse increased significantly when going from warm to cold temperature. Sample waveforms can be found in Fig. B.3. To understand the

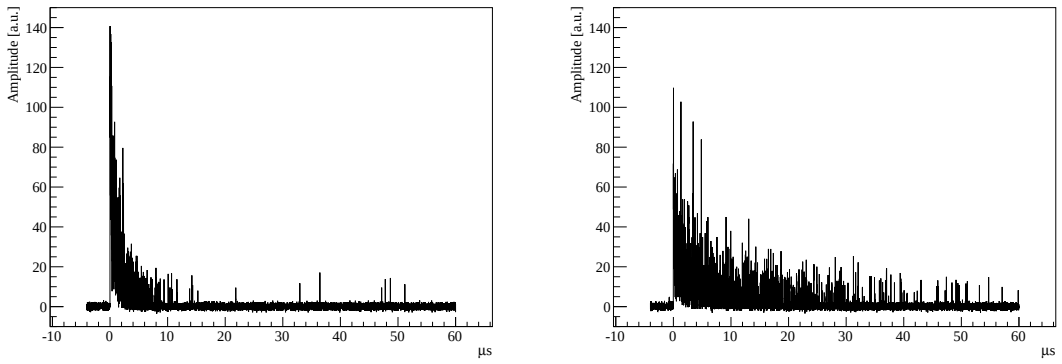

(a) 295 K (b) 77 K

Figure B.3: Some waveforms from Measurement A.

changing pulse shape, we define the parameter f_{90} as the integral of the first 90 ns of the pulse divided by the integral of the entire pulse. The length of the pulse was set by the end of the data-taking window, which for Measurement A was 60 µs after the trigger.

A plot of f_{90} vs. pulse integral can be found in Fig. B.4, where data from both measurements is shown on the same set of axes. The pulse integral is defined in terms of single photoelectrons (PE) detected by the PMT. The single PE pulse integral was calibrated by a fit to the distribution of integrals from pulses found in the tails of each waveform.

The non-Gaussian shape of the peaks, seen by eye in Fig. B.4, were discovered to be a result of the ^{210}Po needle source not being mono-energetic, possibly due to the alphas being degraded by a thin protective coating.

The average waveform (AW) was calculated from each measurement to quantify the different time components involved in the scintillation process.

The shapes of the AWs resemble that of a short-lived exponential (prompt signal) followed by a power-law decay with an exponential cutoff (delayed signal), which contained most of the light. The 295 K AW also contains a small exponential component with an even longer lifetime (tail signal). It is suspected that the tail is present at

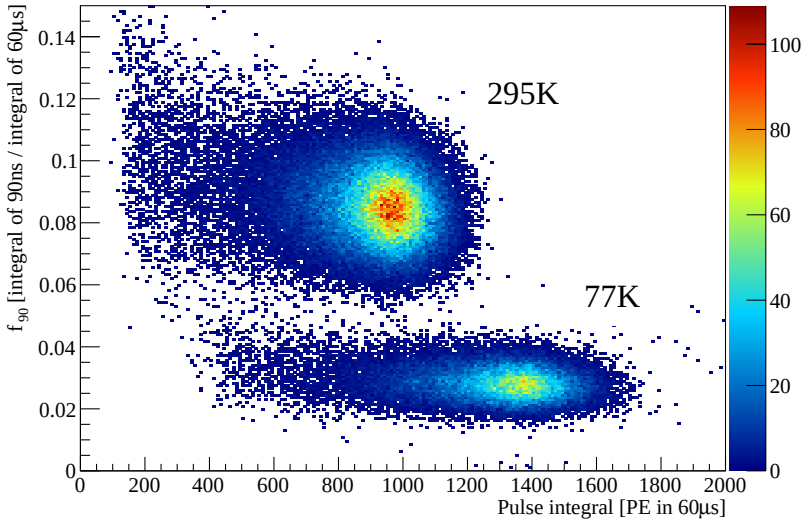

Figure B.4: Pulse shape parameter f_{90} vs. pulse integral. As the temperature decreases, the MgF_2 produces more scintillation and has a longer pulse shape.

77 K as well, but the delayed signal at 77 K remains dominant up until the end of the 60 µs window, so it could not be seen.

The fit function was then convolved with a Gaussian ($G(t;\mu,\sigma)$) to account for the timing resolution of the detector. The full fit function is therefore:

$$f(t) = G(t;\mu,\sigma) * \left(\frac{N_0}{\tau_0} e^{-t/\tau_0} + \frac{N_1}{I_1} \frac{e^{-t/\tau_1}}{(1+t/t_a)^n} + \frac{N_2}{\tau_2} e^{-t/\tau_2} \right) \tag{B.1}$$

The parameters N_0, N_1, and N_2 are the relative fractions of light in the prompt, delayed, and tail components, respectively. The average waveform is scaled to an integral of 1, so after fitting the $f(t)$, each parameter N_x ($x = 0, 1, 2$) is re-scaled as $N'_x = N_x/(N_0 + N_1 + N_2)$ to reflect this normalization.

The parameters τ_0, τ_1, and τ_2 are the lifetimes of the prompt, delayed, and tail components, respectively.

The parameters t_a and n set the timescale and rate of the power law decay. On a log-log plot, the expression $1/(1 + t/t_a)^n$ appears flat up until t_a, after which it transitions to a line with slope $-n$.

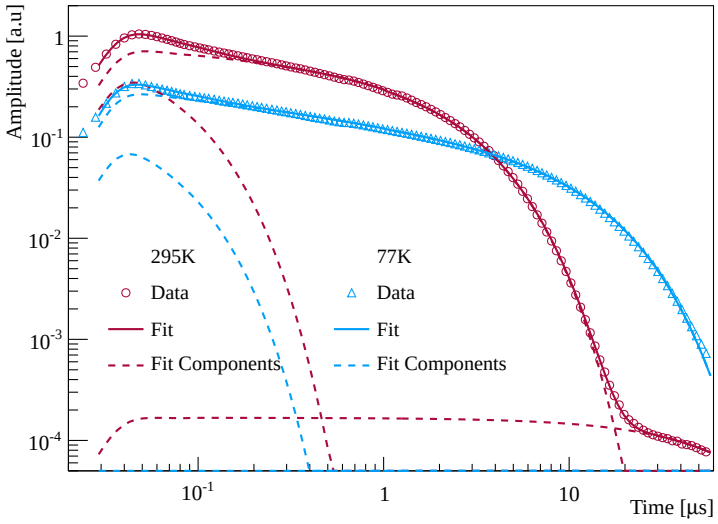

Figure B.5: Measurement A average waveforms. The lifetime of the dominant component increases from 2.3 µs at 295 K to 13 µs at 77 K. The longest component of the 295 K waveform, seen at the bottom right, is suspected of being present at 77 K as well, but the 60 µs acquisition window was not long enough to capture it.

Finally, the parameter I_1 is a normalization parameter that allows N_1 to reflect the integral of the delayed component. It is defined as

$$I_1 = \int_0^\infty \frac{e^{-t/\tau_1}}{(1+t/t_a)^n}\,\mathrm{d}t = e^{t_a/\tau_1} t_a^n \tau_1^{1-n} \Gamma(1-n, t_a/\tau_1)$$

where $\Gamma(s,x) = \int_x^\infty t^{s-1}e^{-t}\,\mathrm{d}t$ is the upper incomplete gamma function.

The average waveforms with their overlaid fits can be found in Fig. B.5. The parameters for each fit can be found in Table B.1.

At either temperature, the dominant component of the scintillation was discovered to have a lifetime of microseconds, orders of magnitude longer than that of LXe's 4.3 and 22 ns scintillation lifetimes [61]. This would allow LXe detectors to use pulse-shape discrimination to reject surface events.

T	N_0'	τ_0(ns)	N_1'	τ_1(µs)	t_a (µs)	n	N_2	τ_2(µs)
295 K	0.029(20)	54(10)	0.96(1)	2.3(1)	0.055(50)	0.18(3)	0.013(3)	73(10)
77 K	0.0055(50)	49(10)	0.99(3)	13(1)	0.055(50)	0.27(1)	—	—

Table B.1: The fit parameters for $f(t)$. Statistical errors were found to be negligible. Systematic errors, shown in parenthesis, refer to the uncertainty of the last digits and reflect the error from binning choice and initial fit parameters. The Gaussian convolution parameters $\mu = 30(1)$ ns and $\sigma = 8.5(10)$ ns were the same across both measurements.

B.2.2 Measurement B

Measurement B was designed to demonstrate the surface background suppression capability of MgF_2 in practice. Two 1 mm by 5 mm MgF_2 discs were placed in a chamber filled with ^{222}Rn gas to collect a sample of ^{214}Bi radon daughters on their surface. After being exposed to radon for over 3 hours, the discs, now sources themselves, were placed in the detector, which was then cooled down and filled with scintillation-grade LAr (Fig. B.1 (B)).

Results

LAr produces different pulse shapes for different forms of incident radiation (see Chapter 3). Betas and gammas have an f_{90} of ~ 0.3, while alphas have an f_{90} of 0.6-0.7. This resulted in several populations of events being visible in a plot of f_{90} vs. pulse integral, which can be seen in Fig. B.6. Many of the larger pulse integrals have been corrected for digitizer saturation by using a linear map to pulse integrals from a digitizer channel that received unamplified signals from the PMT in a manner similar to Sec. 8.3.1.

Four populations of events are highlighted in Fig. B.6. The origin of each population can be identified using the delayed ^{214}Bi–^{214}Po coincidence. This is done by looking for a timing correlation between events in one population and events in an-

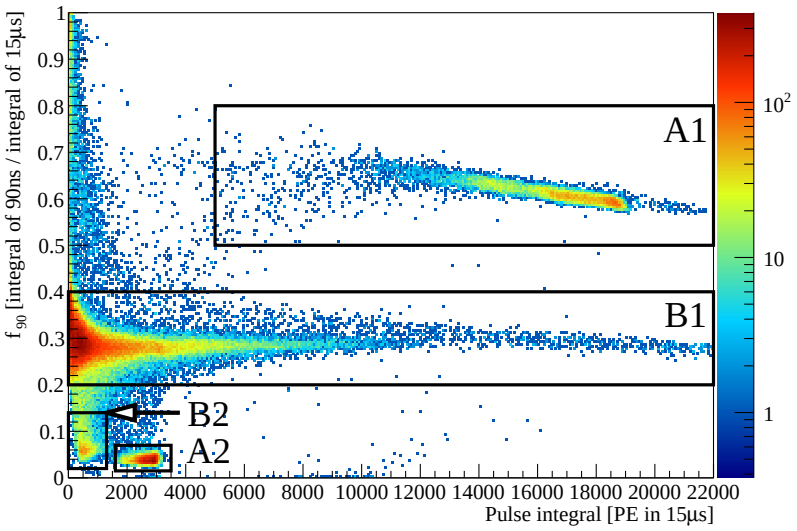

Figure B.6: Measurement B data. Four distinct event populations can be seen. These populations are identified using the delayed ^{214}Bi–^{214}Po coincidence (explained in the text). A1 is the ^{214}Po alpha in LAr. A2 is the ^{214}Po alpha in MgF_2. B1 is the ^{214}Bi beta or gamma, or external background gamma, in LAr. B2 is the ^{214}Bi beta or gamma in MgF_2.

other. A histogram of the time delay Δt between the ^{214}Bi decay and the ^{214}Po decay should follow an exponential with $\lambda_{1/2} = 164\,\mu s$.

A total of 16 histograms were generated for every combination Δt_{XY}, which is the elapsed time between an event in the region labelled X and the next event in the region labeled Y, for $X, Y \in \{A1, A2, B1, B2\}$. Only four combinations were found to follow an exponential distribution with the expected ^{214}Po half-life. These four distributions are Δt_{B1A1}, Δt_{B1A2}, Δt_{B2A1}, and Δt_{B2A2} and are shown in Fig. B.7. The other combinations showed no correlation.

We can conclude from this correlation that populations B1 and B2 contain ^{214}Bi beta decay events, and populations A1 and A2 contain ^{214}Po alpha decay events. This is consistent with our understanding of f_{90} from previous measurements with LAr (see Chapter 8) that identify A1 events as alphas in LAr and B1 events as betas or gammas in LAr. The results from Measurement A confirm the identity of A2

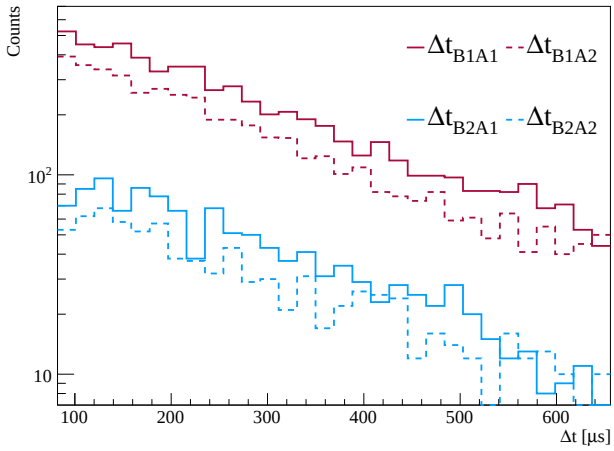

Figure B.7: Delay time between events in the labelled populations in Fig. B.6. The distributions follow an exponential decay with a half-lives between 155 µs and 175 µs, consistent with the 164 µs half-life of ^{214}Po. This indicates that populations B1 and B2 correspond to ^{214}Bi beta decay and populations A1 and A2 correspond to ^{214}Po alpha decay.

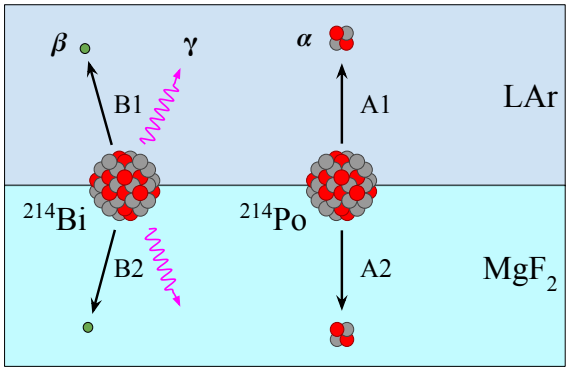

Figure B.8: Origin of the event populations in Fig. B.6.

events as alphas in MgF_2, which leaves B2 as the betas and gammas in MgF_2. This is summarized in Fig. B.8.

Events from external gamma backgrounds are also expected to be present in B1, but the measured rate of this background (taken after the radon daughters had decayed away) was between 1 and 10 Hz, making the accidental coincidence rate with the short-lived ^{214}Po negligible.

With radon daughters on the surface of the MgF_2 disc, it is expected that 50% of the betas from ^{214}Bi would be directed into the MgF_2 during the decay. The

difference in rate between coincidences starting with B1 and those starting with B2 (see Fig. B.7) can be attributed to the coincident gammas. ^{214}Bi emits one or more coincident gammas in about 80% of its decays. If the beta is directed into the MgF_2 while a high energy coincident gamma is directed into the LAr, the gamma signal is expected to dominate and place the event in B1. The events between populations B1 and B2 are speculated to be from when these pileups occur with lower energy gammas.

Light Yield

The mean value of the 15 µs pulse integrals for ^{214}Po alphas in MgF_2 (A2) is (2699 ± 188) PE. Assuming the pulse shape is similar at LAr temperature (87 K), we know from the fit to the 77 K AW in Measurement A that 79.7% of the light from the pulse occurs in the first 15 µs.

A measurement of the light yield in the detector was obtained with the 60 keV gamma from an ^{241}AmBe source. The result was a light yield of (5.78±0.01) PE/keV.

Combining these values gives an electron equivalent energy for the interaction of $(586 \pm 41)\,\mathrm{keV}_{ee}$. The ^{214}Po alpha has an energy of 7.7 MeV, giving an overall quenching factor in MgF_2 of 13.1 ± 0.9.

B.3 Conclusions

A ^{214}Po alpha depositing its full energy in MgF_2 is expected to produce a $(586 \pm 41)\,\mathrm{keV}_{ee}$ signal, well above the detection threshold of LXe experiments. It also produces a pulse with a distinctive shape for easy identification. If coated on the surface of a LXe experiment it could be used to reject events caused by the decay of radioisotopes on the surface.

Bibliography

[1] M. Lisanti. Lectures on Dark Matter Physics. In J. Polchinski and et al., editors, *New Frontiers in Fields and Strings (TASI 2015)*, pages 399–446, 2017, 1603.03797.

[2] F. Zwicky. Die Rotverschiebung von extragalaktischen Nebeln. *Helvetica Physica Acta*, 6:110–127, 1933.

[3] V. C. Rubin et al. Motion of the Galaxy and the local group determined from the velocity anisotropy of distant SC I galaxies. I - The data. *Astronomical Journal*, 81:687–718, September 1976.

[4] V. C. Rubin and W. K. Ford, Jr. Rotation of the Andromeda Nebula from a Spectroscopic Survey of Emission Regions. *Astrophysical Journal*, 159:379, February 1970.

[5] Astronomy Picture of the Day. `https://web.archive.org/web/20170311200254/https://apod.nasa.gov/apod/ap111221.html`. [Online; accessed 7-October-2017].

[6] A. N. Taylor, S. Dye, T. J. Broadhurst, N. Bentez, and E. van Kampen. Gravitational lens magnification and the mass of abell 1689. *The Astrophysical Journal*, 501(2):539, 1998.

[7] C.S. Frenk and S.D.M. White. Dark matter and cosmic structure. *Annalen der Physik*, 524(9-10):507–534, 2012.

[8] Douglas Clowe, Marua Brada, Anthony H. Gonzalez, Maxim Markevitch, Scott W. Randall, Christine Jones, and Dennis Zaritsky. A direct empirical proof of the existence of dark matter. *The Astrophysical Journal Letters*, 648(2):L109, 2006.

[9] Wayne Hu. An Introduction to the CMB. `http://background.uchicago.edu/~whu/beginners/introduction.html`. [Online; accessed 18-Sep-2017].

[10] M. Milgrom. A modification of the Newtonian dynamics as a possible alternative to the hidden mass hypothesis. *Astrophysical Journal*, 270:365–370, July 1983.

[11] S. Knapen, T. Lin, and K. M. Zurek. Light Dark Matter: Models and Constraints. *ArXiv e-prints*, September 2017, 1709.07882.

[12] Daniel J. H. Chung, Edward W. Kolb, and Antonio Riotto. Superheavy dark matter. *Phys. Rev. D*, 59:023501, Nov 1998.

[13] Adrian Cho. Two big dark matter experiments gain U.S. support. `http://www.sciencemag.org/news/2014/07/two-big-dark-matter-experiments-gain-us-support`, July 2014. [Online; accessed 6-July-2017].

[14] M. Klasen et al. Indirect and direct search for dark matter. *Progress in Particle and Nuclear Physics*, 85:1–32, November 2015, 1507.03800.

[15] P. Agnes et al. First results from the DarkSide-50 dark matter experiment at Laboratori Nazionali del Gran Sasso. *Physics Letters B*, 743:456–466, 2015.

[16] DEAP-3600 Collaboration. First results from the DEAP-3600 dark matter search with argon at SNOLAB. *ArXiv e-prints*, July 2017, 1707.08042.

[17] Teppei Katori. MicroBooNE, A Liquid Argon Time Projection Chamber (LArTPC) Neutrino Experiment. *AIP Conference Proceedings*, 1405(1):250–255, 2011, http://aip.scitation.org/doi/pdf/10.1063/1.3661595.

[18] R Hennings-Yeomans. Direct Detection of Dark Matter with MiniCLEAN. *Journal of Physics: Conference Series*, 315, 2011.

[19] M. Agostini et al. Search of Neutrinoless Double Beta Decay with the GERDA Experiment. *Nuclear and Particle Physics Proceedings*, 273275:1876 – 1882, 2016. 37th International Conference on High Energy Physics (ICHEP).

[20] A Marchionni et al. ArDM: a ton-scale LAr detector for direct Dark Matter searches. *Journal of Physics: Conference Series*, 308(1):012006, 2011.

[21] J. Strait et al. Long-Baseline Neutrino Facility (LBNF) and Deep Underground Neutrino Experiment (DUNE) Conceptual Design Report Volume 3: Long-Baseline Neutrino Facility for DUNE June 24, 2015. *ArXiv e-prints*, January 2016, 1601.05823.

[22] M. Martin. Exciton Self-Trapping in Rare-Gas Crystals. *Journal of Chemical Physics*, 54:3289–3299, April 1971.

[23] A. Hitachi, T. Doke, and A. Mozumder. Luminescence quenching in liquid argon under charged-particle impact: Relative scintillation yield at different linear energy transfers. *Phys. Rev. B*, 46:11463–11470, Nov 1992.

[24] H. Cao et al. Measurement of scintillation and ionization yield and scintillation pulse shape from nuclear recoils in liquid argon. *Phys. Rev. D*, 91:092007, May 2015.

[25] Alden Fan. *Results from the DarkSide-50 Dark Matter Experiment*. Ph.D. thesis, UCLA, 2016.

[26] Shawn Westerdale. *A Study of Nuclear Recoil Backgrounds in Dark Matter Detectors*. Ph.D. thesis, Princeton University, 2016.

[27] J. Xu et al. A study of the trace 39Ar content in argon from deep underground sources. *Astroparticle Physics*, 66:53 – 60, 2015.

[28] P. Agnes et al. Results from the first use of low radioactivity argon in a dark matter search. *Phys. Rev. D*, 93:081101, Apr 2016a.

[29] Henning O. Back et al. First Large Scale Production of Low Radioactivity Argon From Underground Sources. *ArXiv e-prints*, 2012, 1204.6024.

[30] H. O. Back et al. First Commissioning of a Cryogenic Distillation Column for Low Radioactivity Underground Argon. *ArXiv e-prints*, 2012, 1204.6061.

[31] Sandro De Cecco and Claudio Giganti. DARKSIDE @ LPNHE : DS-20K project. `https://indico.in2p3.fr/event/12120/contribution/1/material/slides/1.pdf`, 2015.

[32] T. Igarashi, M. Tanaka, T. Washimi, and K. Yorita. Performance of VUV-sensitive MPPC for liquid argon scintillation light. *Nuclear Instruments and Methods in Physics Research Section A: Accelerators, Spectrometers, Detectors and Associated Equipment*, 833:239 – 244, 2016.

[33] J.B. Birks. Chapter 3 - The Scintillation Process in Organic Materials–I. In J.B. Birks, editor, *The Theory and Practice of Scintillation Countin*, International Series of Monographs in Electronics and Instrumentation, pages 39 – 67. Pergamon, 1964.

[34] William R. Leo. *Techniques for Nuclear and Particle Physics Experiments: A How-to Approach*. Springer, 1994.

[35] Brunet, Max, Cantin, Michel, Julliot, Claude, and Vasseur, Jacques. Propriétés de photocathodes métalliques et de couches fluorescentes dans l'ultraviolet lointain. *Le Journal de Physique Physique Appliquée*, 24(S3):53–59, 1963.

[36] Trinh Thi Hoang Mai and R. Drouin. Relative Quantum Efficiencies of Some Ultraviolet Scintillators. *Appl. Opt.*, 10(1):207–208, Jan 1971.

[37] W. M. Burton and B. A. Powell. Fluorescence of Tetraphenyl-Butadiene in the Vacuum Ultraviolet. *Appl. Opt.*, 12(1):87–89, Jan 1973.

[38] C.H. Lally, G.J. Davies, W.G. Jones, and N.J.T. Smith. UV quantum efficiencies of organic fluors. *Nuclear Instruments and Methods in Physics Research Section B: Beam Interactions with Materials and Atoms*, 117(4):421 – 427, 1996.

[39] D.N. McKinsey et al. Fluorescence efficiencies of thin scintillating films in the extreme ultraviolet spectral region. *Nuclear Instruments and Methods in Physics Research Section B: Beam Interactions with Materials and Atoms*, 132(3):351 – 358, 1997.

[40] V.M. Gehman et al. Fluorescence efficiency and visible re-emission spectrum of tetraphenyl butadiene films at extreme ultraviolet wavelengths. *Nuclear Instruments and Methods in Physics Research Section A: Accelerators, Spectrometers, Detectors and Associated Equipment*, 654(1):116 – 121, 2011.

[41] B J P Jones, J K VanGemert, J M Conrad, and A Pla-Dalmau. Photodegradation mechanisms of tetraphenyl butadiene coatings for liquid argon detectors. *Journal of Instrumentation*, 8(01):P01013, 2013.

[42] R Francini et al. VUV-Vis optical characterization of Tetraphenyl-butadiene films on glass and specular reflector substrates from room to liquid Argon temperature. *Journal of Instrumentation*, 8(09):P09006, 2013.

[43] C. P. Benson, G. D. Orebi Gann, and V. M. Gehman. Measurements of the Intrinsic Quantum Efficiency and Visible Reemission Spectrum of Tetraphenyl Butadiene Thin Films for Incident Vacuum Ultraviolet Light. *ArXiv e-prints*, September 2017, 1709.05002.

[44] Hamamatsu. 2015 Photonic Devices. `https://web.archive.org/web/20150404111054/http://www.hamamatsu.com:80/resources/pdf/etd/p-dev_2015_TOTH0023E.pdf`. [Online; accessed 28-September-2017].

[45] Tosoh. Optical Silica Glass. `https://web.archive.org/web/20170928144925/https://cdn.shopify.com/s/files/1/1090/0622/files/Tosoh-ES-ED-H-Series-Fused-Silica.pdf?5509191820080193540`. [Online; accessed 28-September-2017].

[46] aStar - Physical Measurement Laboratory. `https://physics.nist.gov/PhysRefData/Star/Text/ASTAR.html`. [Online; accessed 28-September-2017].

[47] M G Boulay. DEAP-3600 Dark Matter Search at SNOLAB. *Journal of Physics: Conference Series*, 375(1):012027, 2012.

[48] Jingke Xu, Chris Stanford, Shawn Westerdale, Frank Calaprice, Alexander Wright, and Zhiming Shi. First measurement of surface nuclear recoil background for argon dark matter searches. *Phys. Rev. D*, 96:061101, Sep 2017.

[49] Kelly Swanson Sten Hansen. R11065neghvbase-7.pdf. `http://lartpc-docdb.fnal.gov/cgi-bin/RetrieveFile?docid=441&filename=R11065NegHVBase-7.pdf&version=1`. [Online; accessed 10-Sep-2017].

[50] Pfeiffer Vacuum. Hicube. https://www.pfeiffer-vacuum.com/filepool/File/Literature/Turbopumps-PT0191PEN.pdf. [Online; accessed 28-September-2017].

[51] SAES Pure Gas Inc. PS3-MT3 MonoTorr Heated Getter Gas Purifier. https://web.archive.org/web/20170928144514/http://www.saespuregas.com/Library/specifications-brochures/MonoTorr_Brochure.pdf. [Online; accessed 28-September-2017].

[52] Pfeiffer Vacuum. Hlt5xx. https://www.idealvac.com/files/ManualsII/Pfeiffer_SmartTest_Instruction_Manual_2.pdf. [Online; accessed 10-Sep-2017].

[53] CAEN-S.p.A. V1720. http://www.caen.it/csite/CaenProd.jsp?idmod=570&parent=11, October 2016.

[54] Ben Loer. Daqman. https://github.com/bloer/daqman, 2016.

[55] R Acciarri and others. Effects of Nitrogen contamination in liquid Argon. *Journal of Instrumentation*, 5(06):P06003, 2010.

[56] Jingke Xu. *Study of Argon from underground sources for dark matter detection.* Ph.D. thesis, Princeton University, 2013.

[57] Spectrum Techniques. Needle Sources. https://web.archive.org/web/20170925203233/http://www.spectrumtechniques.com/products/sources/needle-sources/, 2017. [Online; accessed 25-September-2017].

[58] E. Rault et al. *Optimization of Yttrium-90 Bremsstrahlung Imaging with Monte Carlo Simulations*, pages 500–504. Springer Berlin Heidelberg, Berlin, Heidelberg, 2009.

[59] E. Segreto. Evidence of delayed light emission of tetraphenyl-butadiene excited by liquid-argon scintillation light. *Phys. Rev. C*, 91:035503, Mar 2015.

[60] L.M. Veloce others. Temperature dependence of alpha-induced scintillation in the 1,1,4,4-tetraphenyl-1,3-butadiene wavelength shifter. *Journal of Instrumentation*, 11(06):P06003, 2016.

[61] Akira Hitachi et al. Effect of ionization density on the time dependence of luminescence from liquid argon and xenon. *Phys. Rev. B*, 27:5279–5285, May 1983.

[62] R. Voltz and G. Laustriat. Radioluminescence des milieux organiques I. Étude cinétique. *J. Phys. France*, 29:159–166, 1968.

[63] Tiago Palmeira, Alexander Fedorov, and Mário N Berberan-Santos. Temperature dependence of the phosphorescence and of the thermally activated delayed fluorescence of $^{12}C_{70}$ and $^{13}C_{70}$ in amorphous polymer matrices. Is a second triplet involved? *Methods and Applications in Fluorescence*, 2(3):035002, 2014.

[64] EStar - Physical Measurement Laboratory. `https://physics.nist.gov/PhysRefData/Star/Text/ESTAR.html`. [Online; accessed 28-September-2017].

[65] P. Sanguino, F. Balau, A.M. Botelho do Rego, A. Pereira, and V. Chepel. Stability of tetraphenyl butadiene thin films in liquid xenon. *Thin Solid Films*, 600:65 – 70, 2016.

[66] Alexander I. Bolozdynya et al. Using a wavelength shifter to enhance the sensitivity of liquid xenon dark matter detectors. *IEEE Trans. Nucl. Sci.*, 55:1453–1457, 2008.

[67] P Agnes et al. The veto system of the DarkSide-50 experiment. *Journal of Instrumentation*, 11(03):P03016, Mar 2016.

[68] P Agnes et al. The electronics and data acquisition system for the DarkSide-50 veto detectors. *Journal of Instrumentation*, 11(12):P12007, Dec 2016c.

[69] Linde Gas. Health Hazard Data. `https://web.archive.org/web/20130625060223/http://www.us.lindegas.com/International/Web/LG/US/MSDS.nsf/NotesMSDS/Air+002/$file/Air+002.pdf`, Jan 1995. [Online; accessed 4-August-2017].

[70] A.S. Barabash et al. The BiPo-3 detector for the measurement of ultra low natural radioactivities of thin materials. *Journal of Instrumentation*, 12(06):P06002, 2017.

[71] I Badhrees et al. Measurement of the two-photon absorption cross-section of liquid argon with a time projection chamber. *New Journal of Physics*, 12(11):113024, 2010.

[72] J. Calvo et al. Measurement of the attenuation length of argon scintillation light in the ArDM LAr TPC. *arXiv*, 2016, 1611.02481.

[73] Daniel Käfer. *Characterization and Optimization of Growth and Electronic Structure of Organic Thin Films for Applications in Organic Electronics*. Ph.D. thesis, Ruhr-University Bochum, 11 2008.

[74] P. Agnes et al. Effect of low electric fields on alpha scintillation light yield in liquid argon. *Journal of Instrumentation*, 12(01):P01021, 2017.

[75] Akira Hitachi et al. Scintillation and ionization yield for α particles and fission fragments in liquid argon. *Phys. Rev. A*, 35:3956–3958, May 1987.

[76] Akira Hitachi, Jay A. LaVerne, and Tadayoshi Doke. Effect of an electric field on luminescence quenching in liquid argon. *Phys. Rev. B*, 46:540–543, Jul 1992.

[77] Andrew Watson. *Transverse Position Reconstruction in a Liquid Argon Time Projection Chamber using Principal Component Analysis and Multi-Dimensional Fitting*. PhD thesis, Temple University, 2017.

[78] K. Wamba et al. Mobility of thorium ions in liquid xenon. *Nuclear Instruments and Methods in Physics Research Section A: Accelerators, Spectrometers, Detectors and Associated Equipment*, 555(1):205 – 210, 2005.

[79] J. B. Albert et al. Measurements of the ion fraction and mobility of $\alpha-$ and β-decay products in liquid xenon using the EXO-200 detector. *Phys. Rev. C*, 92:045504, Oct 2015.

[80] Jason Brodsky. *xy Position Reconstruction in DarkSide-50*. Ph.D. thesis, Princeton University, 2015.

[81] Shin Ito and Nobuhiro Maeda. Charge distributions of alpha-recoil atoms from electrodeposited 210po source. *Nuclear Instruments and Methods in Physics Research Section B: Beam Interactions with Materials and Atoms*, 28(3):331 – 335, 1987.

[82] TAUP 2017. `https://web.archive.org/web/20170303224415/http://taup2017.snolab.ca`, 2017. [Online; accessed 25-September-2017].

[83] Google Translate. `https://web.archive.org/web/20170919000354/https://translate.google.com/`, 2017. [Online; accessed 19-September-2017].

[84] BonPatron. `https://web.archive.org/web/20170919044834/http://bonpatron.com/`, 2017. [Online; accessed 19-September-2017].

[85] The Exo-200 Collaboration. Search for Majorana neutrinos with the first two years of EXO-200 data. *Nature*, 510:229–234, June 2014, 1402.6956.

[86] Matthew Redshaw, Elizabeth Wingfield, Joseph McDaniel, and Edmund G. Myers. Mass and Double-Beta-Decay Q Value of ^{136}Xe. *Phys. Rev. Lett.*, 98:053003, Feb 2007.

[87] WWW Table of Radioactive Isotopes. 214Bi. `https://web.archive.org/web/20170925194716/http://nucleardata.nuclear.lu.se/toi/nuclide.asp?iZA=830214`, 2017. [Online; accessed 25-September-2017].

[88] Materion. Magnesium Fluoride MgF2 for Optical Coating. `https://web.archive.org/web/20170630124242/https://materion.com/resource-center/product-data-and-related-literature/inorganic-chemicals/fluorides/magnesium-fluoride-mgf2-for-optical-coating`, 2017. [Online; accessed 25-September-2017].

[89] CRYSTRAN. Magnesium Fluoride. https://web.archive.org/web/20170921095103/https://www.crystran.co.uk/optical-materials/magnesium-fluoride-mgf2, 2017. [Online; accessed 25-September-2017].

[90] OMLC. p-Terphenyl. https://web.archive.org/web/20170925224115/http://omlc.org/spectra/PhotochemCAD/html/003.html, 2017. [Online; accessed 25-September-2017].

[91] V. B. Mikhailik and H. Kraus. Performance of scintillation materials at cryogenic temperatures. *Physica Status Solidi B Basic Research*, 247:1583–1599, July 2010, 1001.5461.